LEVEL III

AFAL-TR-77-157

AO 58198

AIR FORCE AVIONICS LABORATORY

ADVANCED ARCHIVAL MEMORY

Corporate Research and Development
General Electric Company
Schenectady, New York 12301

DDC
RECEIVED
MAR 21 1979
C

August 1977

Third Interim Report   October 16, 1976-January 15, 1977

Approved for public release; distribution unlimited.

AIR FORCE AVIONICS LABORATORY
AIR FORCE WRIGHT AERONAUTICAL LABORATORIES
AIR FORCE SYSTEMS COMMAND
WRIGHT-PATTERSON AIR FORCE BASE, OHIO 45433

79 03 21 010

NOTICE

When Government drawings, specifications, or other data are used for any purpose other than in connection with a definitely related Government procurement operation, the United States Government thereby incurs no responsibility nor any obligation whatsoever; and the fact that the government may have formulated, furnished, or in any way supplied the said drawings, specifications, or other data, is not to be regarded by implication or otherwise as in any manner licensing the holder or any other person or corporation, or conveying any rights or permission to manufacture, use, or sell any patented invention that may in any way be related thereto.

This report has been reviewed by the Information Office (OI) and is releasable to the National Technical Information Service (NTIS). At NTIS, it will be available to the general public, including foreign nations.

This technical report has been reviewed and is approved for publication.

MILLARD G. MIER
Project Engineer

FOR THE COMMANDER

ROBERT J. ALMASSY, Maj, USAF
Deputy Chief, Electronic Research Branch
Electronic Technology Division

"If your address has changed, if you wish to be removed from our mailing list, or if the addressee is no longer employed by your organization please notify AFAL/DHR   ,W-PAFB, OH 45433 to help us maintain a current mailing list".

Copies of this report should not be returned unless return is required by security considerations, contractual obligations, or notice on a specific document.

REPORT DOCUMENTATION PAGE	READ INSTRUCTIONS BEFORE COMPLETING FORM

1. REPORT NUMBER	2. GOVT ACCESSION NO.	3. RECIPIENT'S CATALOG NUMBER
AFAL-TR-77-157		

4. TITLE (and Subtitle)

ADVANCED ARCHIVAL MEMORY-

5. TYPE OF REPORT & PERIOD COVERED

Interim Report No. 3-
Oct.16,1976–Jan.15,1977

6. PERFORMING ORG. REPORT NUMBER

SRD-77-086

7. AUTHOR(s)

C.Q. Lemmond, Dr. P.V. Gray
Dr. C.G. Kirkpatrick, J.F. Norton
H.G. Parks, Dr. G.E. Possin

8. CONTRACT OR GRANT NUMBER(s)

F33615-76-C-1322,
ARPA Order-3194

9. PERFORMING ORGANIZATION NAME AND ADDRESS

Corporate Research and Development
General Electric Company
Schenectady, New York 12301

10. PROGRAM ELEMENT, PROJECT, TASK AREA & WORK UNIT NUMBERS

Project 3194/01/01*

11. CONTROLLING OFFICE NAME AND ADDRESS

Air Force Avionics Laboratory (AFAL/DHR)
Wright Patterson Air Force Base, Ohio
45433

12. REPORT DATE

August 1977

13. NUMBER OF PAGES

138

14. MONITORING AGENCY NAME & ADDRESS(if different from Controlling Office)

15. SECURITY CLASS. (of this report)

Unclassified

15a. DECLASSIFICATION/DOWNGRADING SCHEDULE

16. DISTRIBUTION STATEMENT (of this Report)

Approved for public release, distribution unlimited

17. DISTRIBUTION STATEMENT (of the abstract entered in Block 20, if different from Report)

18. SUPPLEMENTARY NOTES

*Prepared for Advanced Research Project Agency
under APRA Order No. 3194

19. KEY WORDS (Continue on reverse side if necessary and identify by block number)

Computer	Ion Implantation
Memory Systems	Alloy Junction
Electron Optics	
Ion Optics	

20. ABSTRACT (Continue on reverse side if necessary and identify by block number)

During this reporting period, effort in the archival memory program included experimental and theoretical studies on planar diode substrates to determine a more exact doping profile measured by anodic oxidation and stripping techniques; improved implanting methods to place the peak of implant distribution near the N layer surface; writing experiments with a variety of im-
(continued on other side)

DD FORM 1473 EDITION OF 1 NOV 65 IS OBSOLETE
1 JAN 73

planted inert ions and a determination of the writing efficiencies; an initial model of the alloy junction formation was made; eutectic alloying with single laser pulses was achieved; the electron beam write station was made operational; and the write optics study was begun with a general analysis of the various configurations.

PREFACE

The objective of this basic research program is to investigate the feasibility of new storage techniques for large archival memories using ion and electron beams with semiconductor targets. The goal is the development of an archival memory capable of storing 10^{14} to 10^{15} bits with rapid access to the stored information.

The currently funded effort (Phase I) deals with feasibility studies of key technical areas. The program covers experimental and analytical investigations: (1) to demonstrate the feasibility of ion implanted and alloy junction storage media, (2) to determine the feasibility of beam optics design required for writing/reading on the media, and (3) to select the better of the two storage methods and perform a preliminary paper design of the concept for further development.

This report covers the third quarter effort. The two previous quarters were described in reports AFAL-TR-76-213 and AFAL-TR-77-35. During this reporting period, effort in the Archival Memory Program included experimental work and theoretical studies on planar diode structures (memory target substrate), implantation of inert ions to form damage writing on a planar diode structure, studies of writing efficiencies of inert ions, eutectic writing with an Nd:YAG laser, and development of the electron beam writing station which was made operational.

A variety of implanted inert ions (Ne^+, Ar^+, Xe^+, Kr^+, and He^+) were characterized for writing efficiency. Fluences required for inert ion writing can

79 03 21 010

be achieved with currently developed ion sources and will permit 10 Mbit/sec recording rates.

Optics studies during the quarter were confined to a general analysis of the various write optics configurations.

TABLE OF CONTENTS

TABLE OF CONTENTS (Cont'd)

LIST OF ILLUSTRATIONS

LIST OF ILLUSTRATIONS (Cont'd)

LIST OF ILLUSTRATIONS (Cont'd)

LIST OF TABLES

Section I

INTRODUCTION AND SUMMARY

The Advanced Archival Memory Program is directed toward the development of a large memory with 10^{14} to 10^{15} bit capacity, rapid access to stored information (< 100 μsec access to a block), and high data rates (10 to 100 Mbits/sec). This Phase I of the overall program addresses technology studies of two memory approaches: (1) ion implantation to form surface diodes or damage bit sites, and (2) electron beam formed alloy junction surface diodes. These studies include not only memory target physics but also feasibility of the beam optics required to form bit sites by either of the approaches. At the conclusion of the studies, the better of the two storage methods will be selected based on memory target feasibility, practicability of the beam optics, and applicability of such a memory to a large, rapid-access archival memory system.

During this quarter of the Advanced Archival Memory Program, a number of technical advances were made and directions for future research established in the following areas:

- Target modeling
- Planar diode (memory target substrate) development
- Ion writing
- Alloy junction writing
- Alloy junction experimental write station
- Writing optics studies

1

TARGET MODELING STUDIES

During previous quarters, modeling studies have been directed toward establishing a better understanding of the motion of electron beam generated carriers in planar diode targets and toward explaining the measured gain as a function of beam energy. During this third quarter, the model has been applied to samples with a doping profile which has been more exactly measured by the anodic oxidation and stripping technique. The agreement between the model and experiment is significantly better when measured doping profiles are used. A Gaussian damage profile was also introduced, and the dependence of gain versus energy behavior on recombination was investigated. The Gaussian damage profile is realistic for damage writing and also does not cause a convergence problem with the model.

PLANAR DIODE (MEMORY TARGET SUBSTRATE) DEVELOPMENT

During this period, a continued effort was made to improve the diode structure. It was shown during the previous quarter that a high built-in electric field at the surface is required for high gain. A method was developed to achieve this field. It consists of producing a steep doping gradient near the surface by implanting through an oxide film of sufficient thickness to put the peak of the implant distribution near the interface. During this period, boron implants were made and demonstrated higher gains than the arsenic implants originally used. Planar diodes of good quality can now be produced. Further optimization is anticipated, however, particularly for low noise operation.

2

ION WRITING

Writing experiments were conducted using a variety of implanted inert ions (Ne^+, Ar^+, Xe^+, Kr^+, and He^+). The work during the quarter corroborated the second quarter suggestion that ion damage, as well as ion doping, may be a viable means for recording information. These studies also included measurements of writing efficiencies. The data on writing efficiency will be used during the fourth quarter in designing high density writing experiments.

ALLOY JUNCTION EXPERIMENTS

As an aid to understanding the factors involved in the alloy diode approach and to help design and interpret the electron beam writing experiments, computer programs were initiated. The programs are designed to give quantitative information and, as experimental writing gets underway, their usefulness in interpreting results will become more pronounced.

Additional laser writing experiments were conducted during this quarter. An Al-Si target was first used and rows of single pulse per site were made. Neutral density filters were introduced to attenuate the laser beam in steps. Laser writing was achieved with no visible surface damage. This achieved one of the main goals of the quarter--eutectic alloying with single pulses of laser radiation.

Another sample target system consisted of Au-Si. The laser beam was used to heat spot patterns, with the energy of the beam varied by use of neutral density filters. Eutectic alloying was observed using a scanning electron microscope.

3

ALLOY JUNCTION EXPERIMENTAL WRITE STATION

A field emission electron beam write station was specified and contracting officer approval for its purchase was obtained very early in the contract. A 120 day delivery promise was not met. The station was delivered November 30, 1976, and installed by the Coates and Welter serviceman by mid-December. The sample holder was modified to accept archival target chips and electrical leads brought out. Electronic blanking and deflection circuitry were incorporated by General Electric. In addition, a heated stage to be used in thermal bias experiments was designed and constructed. Testing of the stage is beginning.

The electron column has undergone initial tests for beam focus and beam current. Electron beam recording tests will begin early in the next quarter.

WRITE OPTICS STUDY

During this quarter, the optics study was confined to acquiring and developing the tools necessary for a general analysis of the various write optics configurations. These tools will be used in the analytical evaluation of specific write optics configurations during the fourth quarter.

Section II

MODELING OF CARRIER MOTION IN PLANAR DIODE STRUCTURES

During the previous two quarters, progress has been made toward establishing a better understanding of the motion of electron beam generated carriers in planar diode targets. During the first quarter, a model was described for the electron beam gain versus beam energy behavior of planar diode targets. The model uses the complete solution of the injected carrier continuity equation including the effects of electric fields due to doping profiles, mobility variation with doping, and the appropriate boundary conditions. The generation of carriers as a function of penetration depth by the electron beam is included using the best experimental data from a number of sources.

During the second quarter, it was shown that this model could explain the measured gain versus beam energy of properly prepared and annealed As^+ implanted planar diodes without the assumption of any bulk recombination. The observed gain reduction at low beam energy could be accounted for entirely by surface recombination. However, even with maximum surface recombination, the As^+ implanted samples achieved more than 50% of the maximum possible gain, if all generated carriers were collected by the planar diode depletion region. It is believed that this model could be applied with similar success to other implanted ions in silicon when the doping profiles have been determined.

During the third quarter, the model was applied to the same As^+ implanted samples but with a more exact doping profile measured by the

5

anodic oxidation and stripping technique which was initiated during the second quarter and is continuing. The agreement between the model and experiment is improved with this newly measured doping profile. This improved agreement will be useful during the following quarter for evaluation of the writing experiments.

During the second quarter, bulk recombination was introduced into the model near the surface. The primary purpose was to explore the differences between bulk recombination near the surface and surface recombination on the gain versus energy behavior. However, these calculations also demonstrated the application of the model to the study of damage writing. During the third quarter, a Gaussian damage profile was introduced and the dependence of the gain versus energy behavior on recombination was investigated. The Gaussian damage profile is more realistic for damage writing and also does not cause a convergence problem with the model.

APPLICATIONS OF CARRIER TRANSPORT MODEL TO GAIN VS ENERGY DATA

During the previous quarter, the gain vs beam energy behavior of As^+ implanted planar diodes was modeled using a published profile due to Schwettmann [1]. This, along with other experiments, demonstrated that the observed gain reduction at low beam energy was due to surface recombination. During the second quarter, one of the arsenic and one of the phosphorus planar diode samples were profiled by anodic oxidation and a 4-point probe. Application of the model to these profiles and comparison to the experimental data are discussed in this section.

6

Figure 1 shows the measured doping profile (solid line) from the Second Quarterly Report for a 100 keV P$^+$ implanted sample at 10^{14} cm^{-2} into $\langle 111 \rangle$ 10-20 ohm-cm silicon. The wafer was annealed at 770°C for 1 hour in argon. The dotted lines are the approximations to the profile used for the model calculation. Figure 2 shows the predicted gain vs beam energy curve based on this profile for two typical values of surface recombination velocity (S_V). The experimental points are from sample P18C which is a section from the same wafer that was profiled. As can be seen, the agreement is very good. The lack of a steep doping gradient near the surface allows a larger amount of recombination at the surface, which results in low diode gain at low beam energies. Figure 3 is a plot of the same data as collection efficiency vs beam energy. The collection efficiency η is defined as

$$\eta = G/G(S_V = 0) \tag{1}$$

where G is the measured or calculated gain and $G(S_V = 0)$ is the maximum possible gain with no surface recombination;

$$G(S_V = 0) = 0.92 \left(\frac{\text{Beam Energy}}{3.64 \text{ eV}} \right) \tag{2}$$

(see Section II of the Second Quarterly Report). This is an alternate way of presenting the gain data which gives a better picture of the degree of agreement especially at low beam energies. As was discussed during the last quarter, recombination velocities in the range of 10^5 to 10^7 cm/sec are typical for electron beam irradiated silicon surfaces. Similar numbers have been observed on BEAMOS (beam addressed metal oxide semiconductor) targets. The model correctly predicts the gain behavior of the phosphorus implanted

7
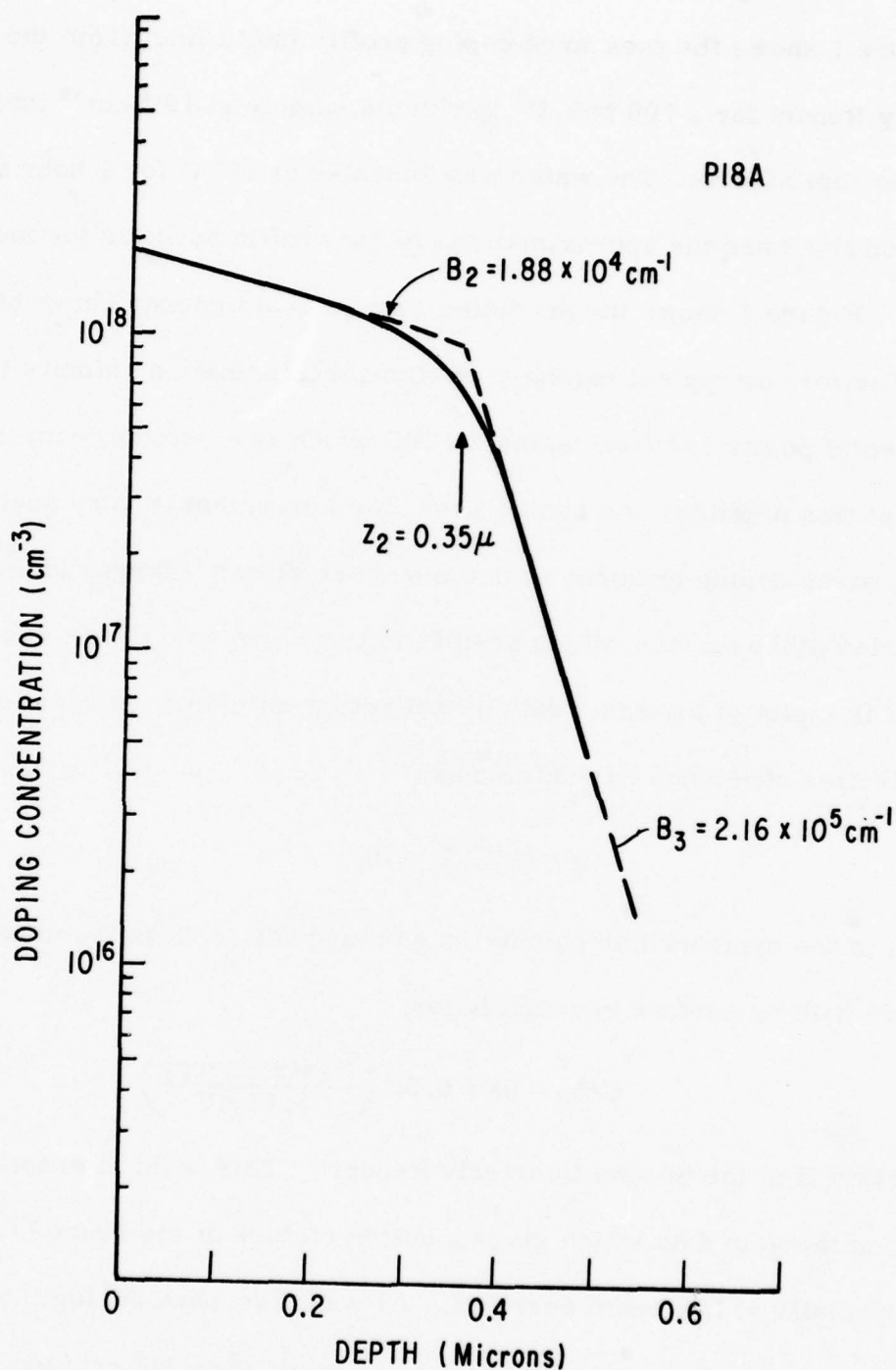
Figure 1. Measured Doping Profile for Sample P18A Prepared by 100 keV P+ Implantation at 10^{14} cm^{-2} into Silicon. (Dotted lines are approximation to data used for model calculations of gain vs beam energy. Parameters of approximation are shown in the figure.)
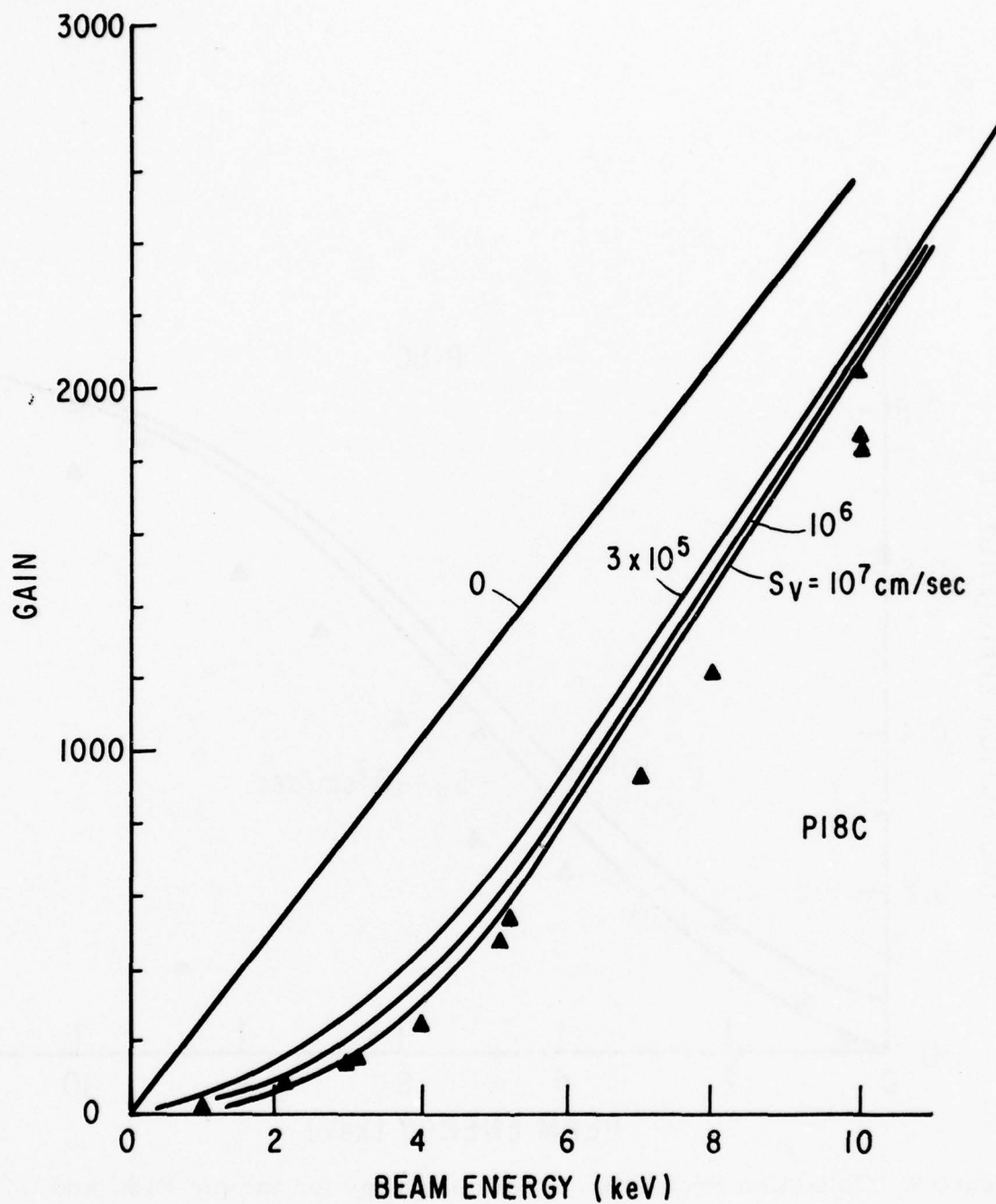
Figure 2. Gain vs Beam Energy Data for Sample P18C. (100 keV P^+ implant at 10^{14} cm^{-2} into $\langle 111 \rangle$ silicon and annealed at 770°C for 1 hour. Solid lines are model calculation based on the doping profile measured by anodic oxidation and a 4-point probe as described in text.)

9
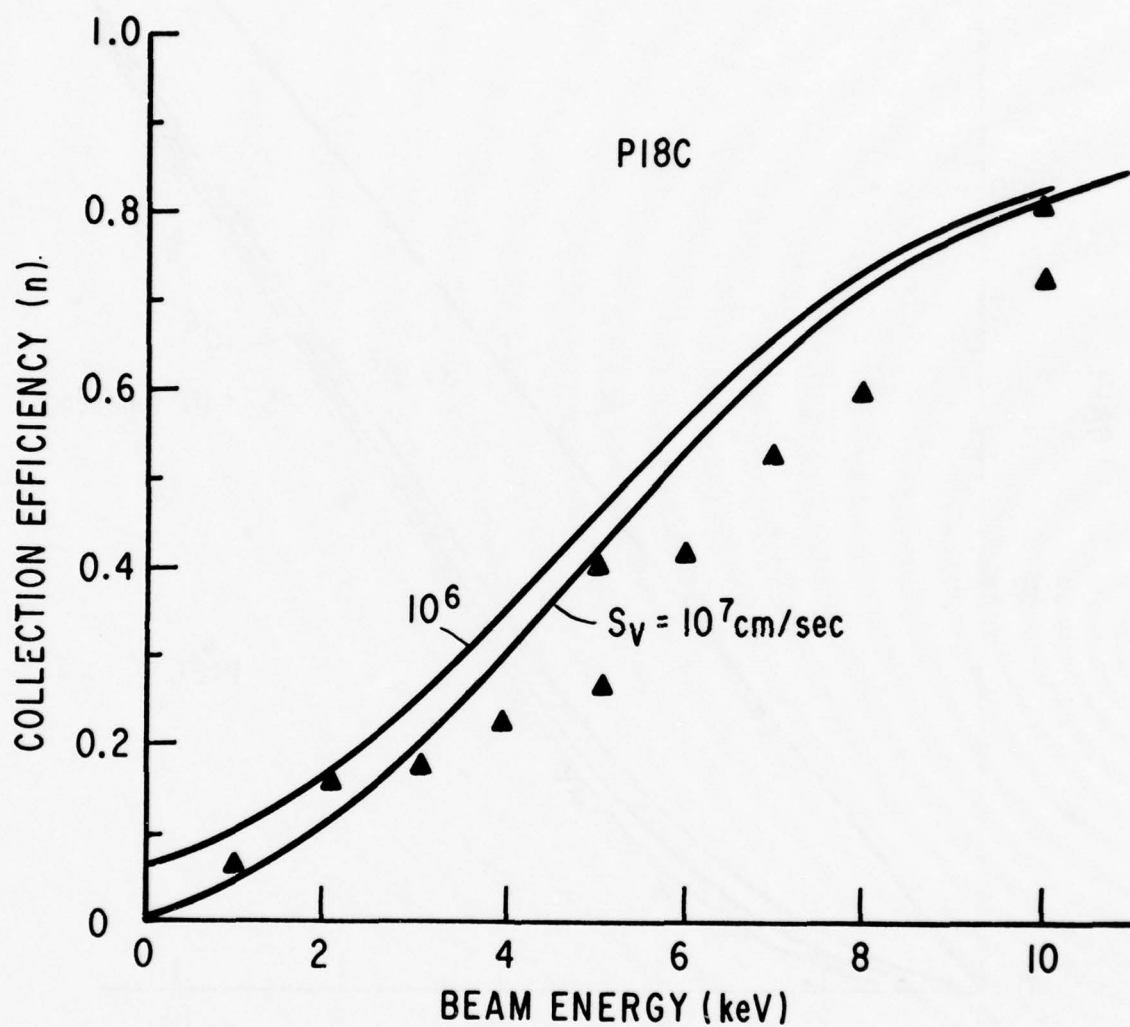
Figure 3. Collection Probability vs Beam Energy for Sample P18C and Model
Calculation as Described in Figure 2

planar diodes with the same value of recombination velocity observed for the arsenic samples and the BEAMOS targets.

Figure 4 shows the measured (•) doping profile for an As$^+$ implanted planar diode prepared by 100 keV As$^+$ implantation at 10^{14} cm^{-2} into 10-20 ohm-cm $\langle 111 \rangle$ float zone silicon after anneal at 770°C for 1 hour in argon. This is taken from the anodic profiling results conducted during the second quarter. The solid curve is the approximation used for the model calculation. The parameters are indicated in the figure caption. Figure 5 shows the predicted and observed gain vs beam energy behavior. The error bars indicate the typical variation in gain over 0.01 cm^2 of surface area. Again the agreement is very good, especially at the low beam energies. The agreement is better than for the calculation on the Schwettmann profile used during the last quarter. The excellent agreement, especially at low beam energies, can be seen more clearly in Figure 6 where the collection efficiency is shown. Again surface recombination velocities in the range of 10^6 cm/sec provide the best fit. The behavior at low beam energies is very sensitive to the profile near the surface and, if a more exact approximation to the measured profile had been used, the agreement would have been slightly better.

MODELING OF DAMAGE WRITING

The interaction of the writing ion beam with the semiconductor causes a number of different changes in the material. If the writing ion is an electrical dopant for the material and resides on a substitutional (i.e., electrically active) site, then the doping level of the material will be altered in the local written region. If the number of introduced dopants is larger than the background doping level and of the opposite type, then electric fields will be

11
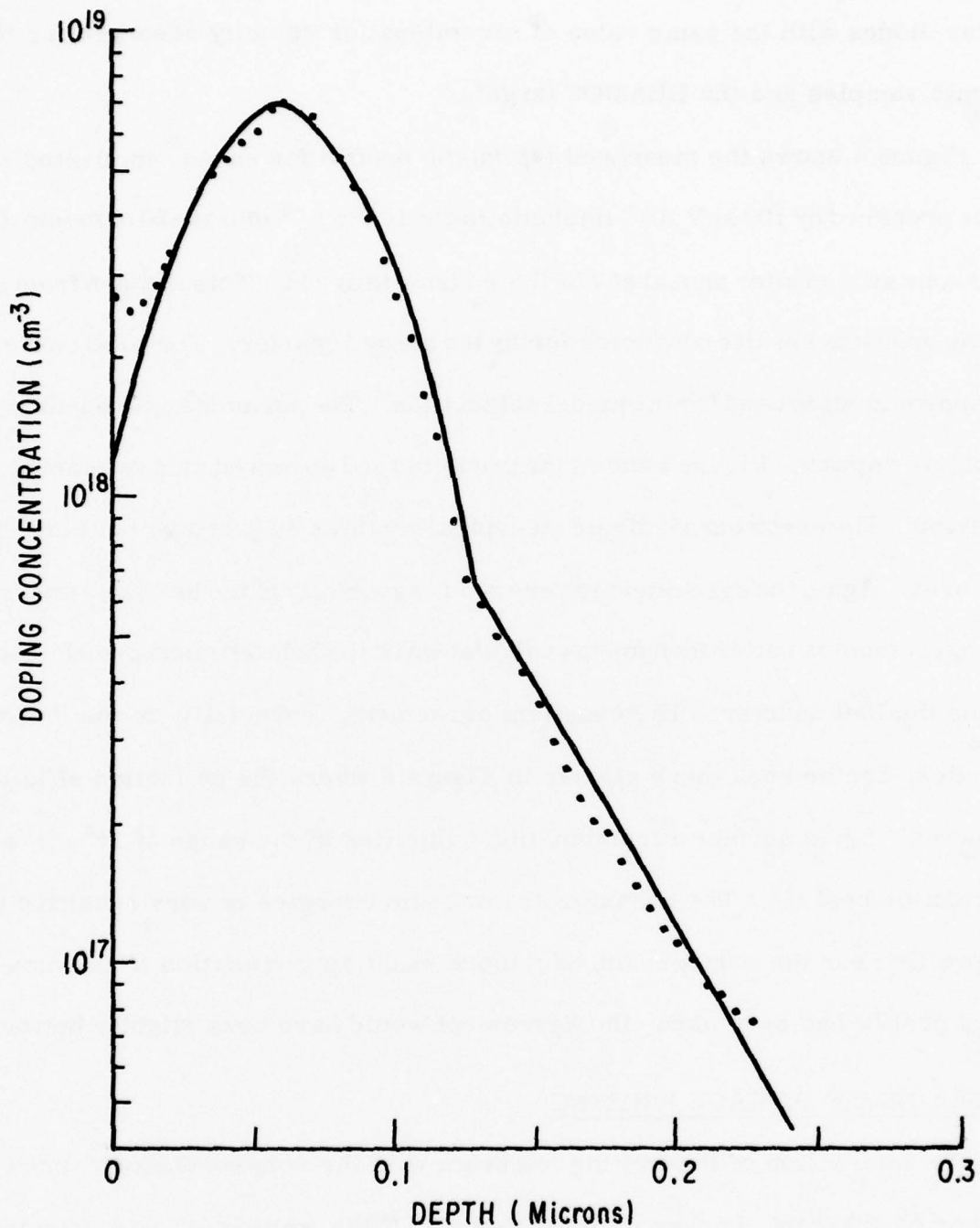
Figure 4. Measured Doping Profile for 100 keV Arsenic Implantation at 10^{14} cm^{-2} into Silicon After Anneal at 770°C for 1 Hour-- Sample A22. (Solid curve is the approximation used for the model calculations. Parameters are z_p = 0.06 μ, σ = 0.045 μ, N_p = 7 × 10^{18} cm^{-3}, z_1 = 0.13 μ, W = 0.4 μ.)
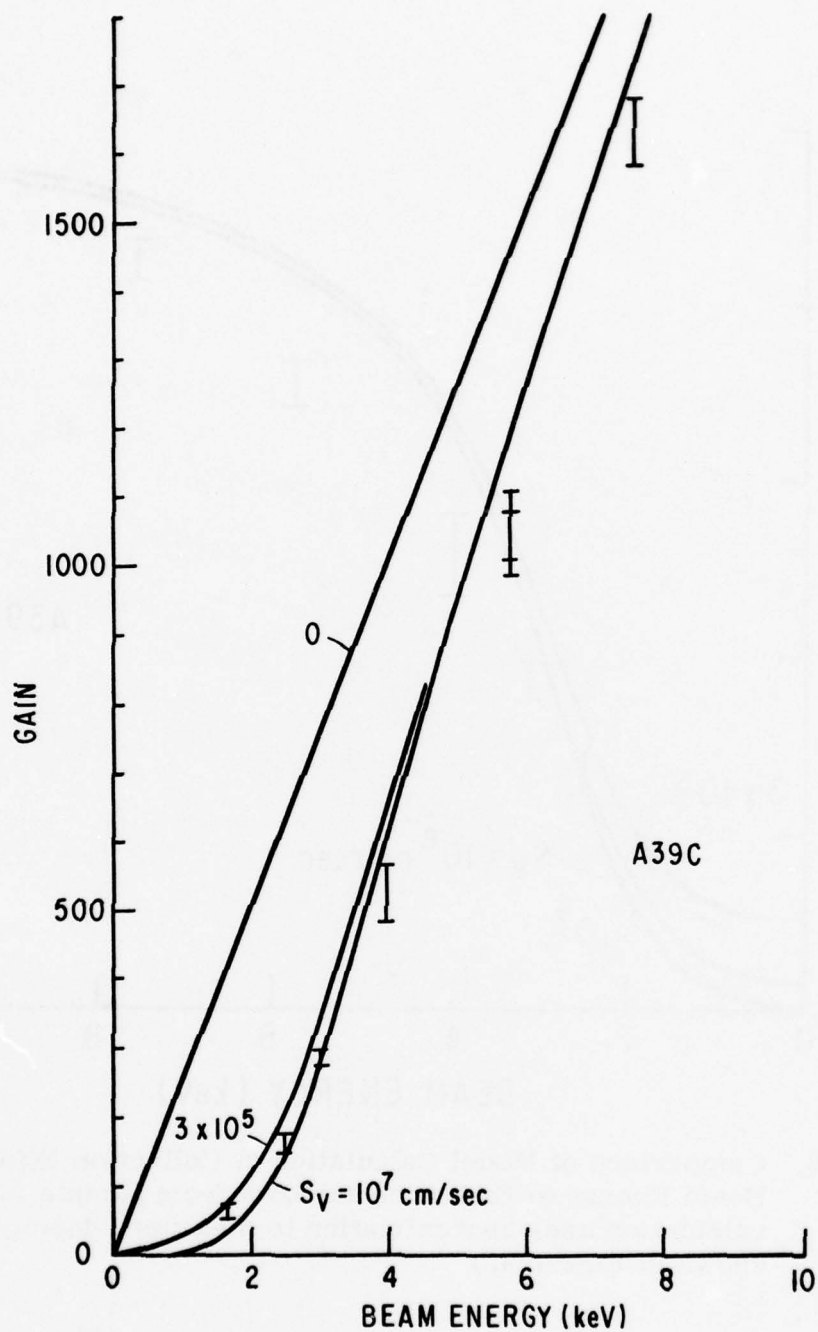
Figure 5. Comparison of Model Calculation for B Gain vs Beam Energy to Experimental Data from Sample A39C. (Model calculation uses approximation to the measured doping profile shown in Figure 4.)

13
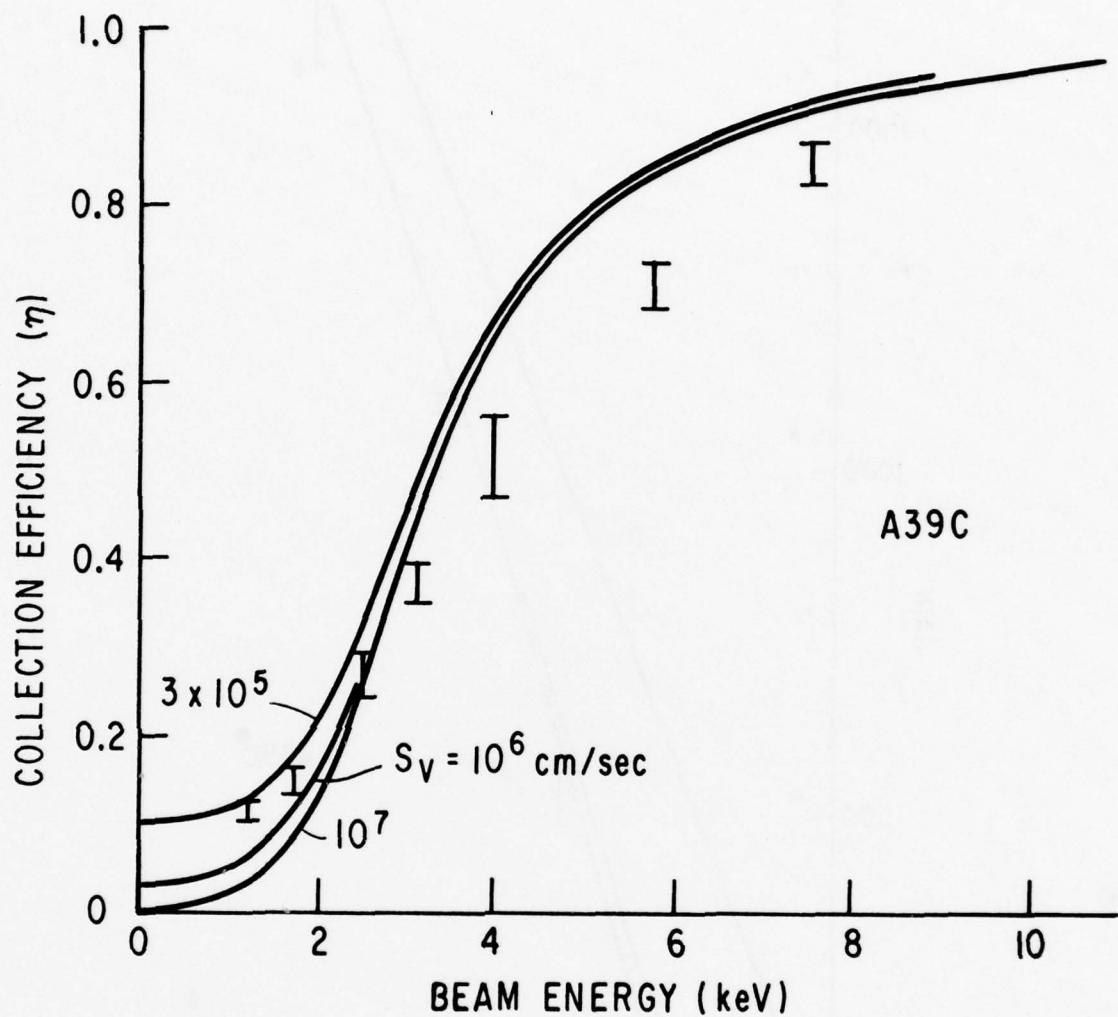
Figure 6. Comparison of Model Calculation of Collection Efficiency vs Beam Energy to Experimental Data from Sample A39C. (Model calculation uses approximation to measured doping profile shown in Figure 4.)

14

produced so as to trap the minority carriers generated by the reading beam and produce low readout signals. If a sufficient number of active dopant is implanted (~ 2X background level), the strongest fields will be produced by formation of actual diode depletion regions. This is the mechanism for doping writing originally postulated for the ion-implant surface diode memory concept.

However, the writing ion beam can also damage the material causing other changes. Two important types of damage are: (1) generation of recombination sites and (2) generation of deep traps. Since the number of generated damage sites can be 1000 or more per incident ion, this type of writing has a potential for much higher writing rates. Two types of damage writing can be distinguished: recombination writing and compensation writing.

Generation of recombination sites would produce local carrier recombination and reduce the readout signal by causing local recombination of the generated electron-hole pairs.

Generation of deep traps would reduce the free carrier recombination in the written region. At a high enough writing fluence, the material would become intrinsic. The effect of these deep traps is therefore much like doping writing except that the written region does not change doping type. However, depletion fields are still produced which tend to trap the generated carriers until they recombine.

Since the possibility of compensation damage writing was not appreciated until late in the third quarter, no attempt has yet been made to model this. Experiments are in progress to discriminate between the two types of damage

writing. These are described in the following section. This section describes modeling of the damage writing due to introduction of recombination centers. The predicted behavior of this type of writing will be one tool used to discriminate between the two types of damage writing.

INTRODUCTION OF RECOMBINATION INTO THE CARRIER DIFFUSION MODEL

During the second quarter, bulk recombination was introduced into the computer program as:

$$\tau = \begin{cases} \tau_1 & z < z_1 \\ 1_{sec} & z > z_1 \end{cases} \tag{3}$$

This type of step function approximation was suitable for studying the effect of bulk recombination in relation to the question of the origin of the gain deficit or dead layer observed in planar diodes. However, this type of recombination profile has two disadvantages for modeling of damage writing. First, as noted during the last quarter, the abrupt discontinuity in the recombination profile causes some problems in convergence of the interaction. Second, this type of profile is a poor approximation of the actual damage profile expected. Damage profiles are discussed in a following section. The damage profile introduced into the model is shown in Figure 7. This damage profile is based on the assumptions that the number of damage sites has a Gaussian distribution and that the recombination rate, $1/\tau$, is proportional to the number of recombination sites. The second assumption is essentially that the recombination sites are independent. As discussed earlier, this model ignores the possibility of compensation type writing. Quite probably both types operate simultaneously.

16
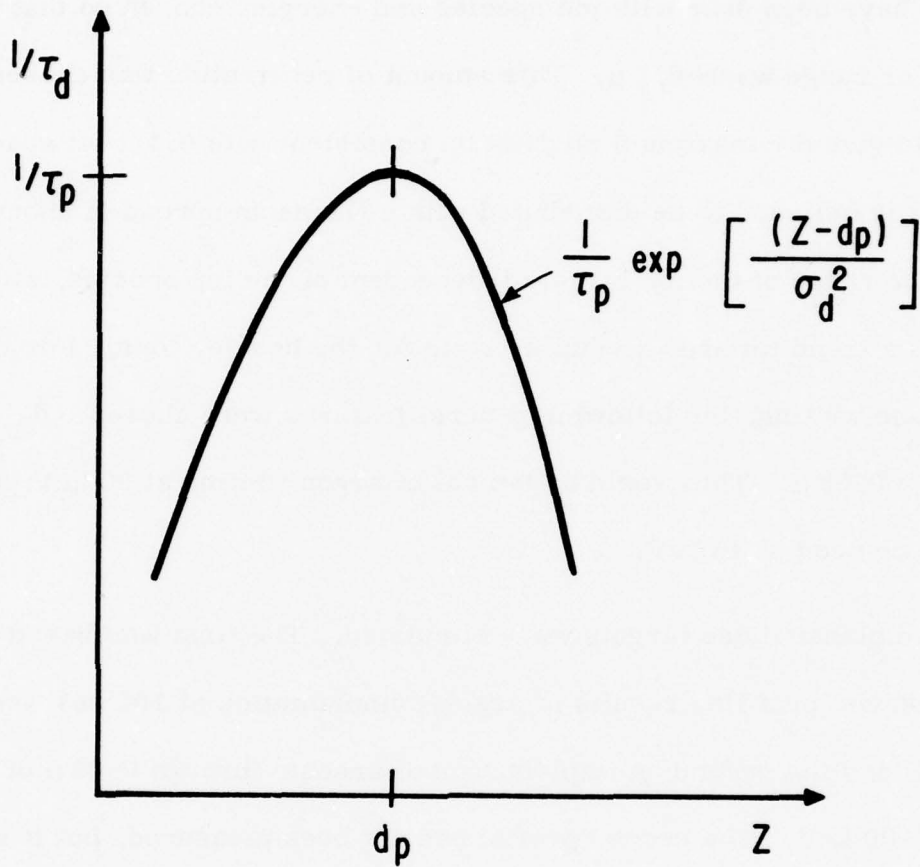
Figure 7. Recombination Distribution for Damage Writing
Simulations. [Parameters are d_p (depth of dis-
tribution's peak), τ_p (lifetime at distribution's
peak) and σ_d.]

To simulate damage recombination writing, the measured arsenic implanted profile was used. Modeling of the gain vs energy behavior using this profile was described earlier in this section. Most of the damage writing studies have been done with ion species and energies chosen so that the penetration or range was ~0.1 μ. This amount of penetration was chosen because it should give the maximum modulation consistent with 0.1 μ bit spacing. Damage is believed to be distributed with a Gaussian spread of about 0.6 times the range of the ion largely independent of the ion species, although there is a trend towards a smaller ratio for the heavier ions. For this type of damage writing, the following general features were chosen: $d_p = 0.08$ μ and $\sigma_p = 0.05$ μ. This would be typical of argon writing at 80 keV, for example, or neon at 40 keV.

Two planar diode targets were simulated. The first was based directly on the anodic profiling results of arsenic implantation at 100 keV and annealed at 770°C and the second on implantation of arsenic through 0.08 μ of thermal SiO_2 at 100 keV. The second profile has not been measured, but it was calculated from the first profile assuming that the thermal oxide has no effect except to remove the first 0.08 μ of the implanted ion distribution. This is what was observed by Schwettmann for arsenic implantation through anodic oxides. Work is in progress to measure this profile.

Figure 8 shows the predicted gain vs beam energy for the 100 keV implant with no oxide and several peak recombination times, τ_p. Figure 9 shows similar data for the 100 keV implant through the oxide. Figure 10 shows the

18
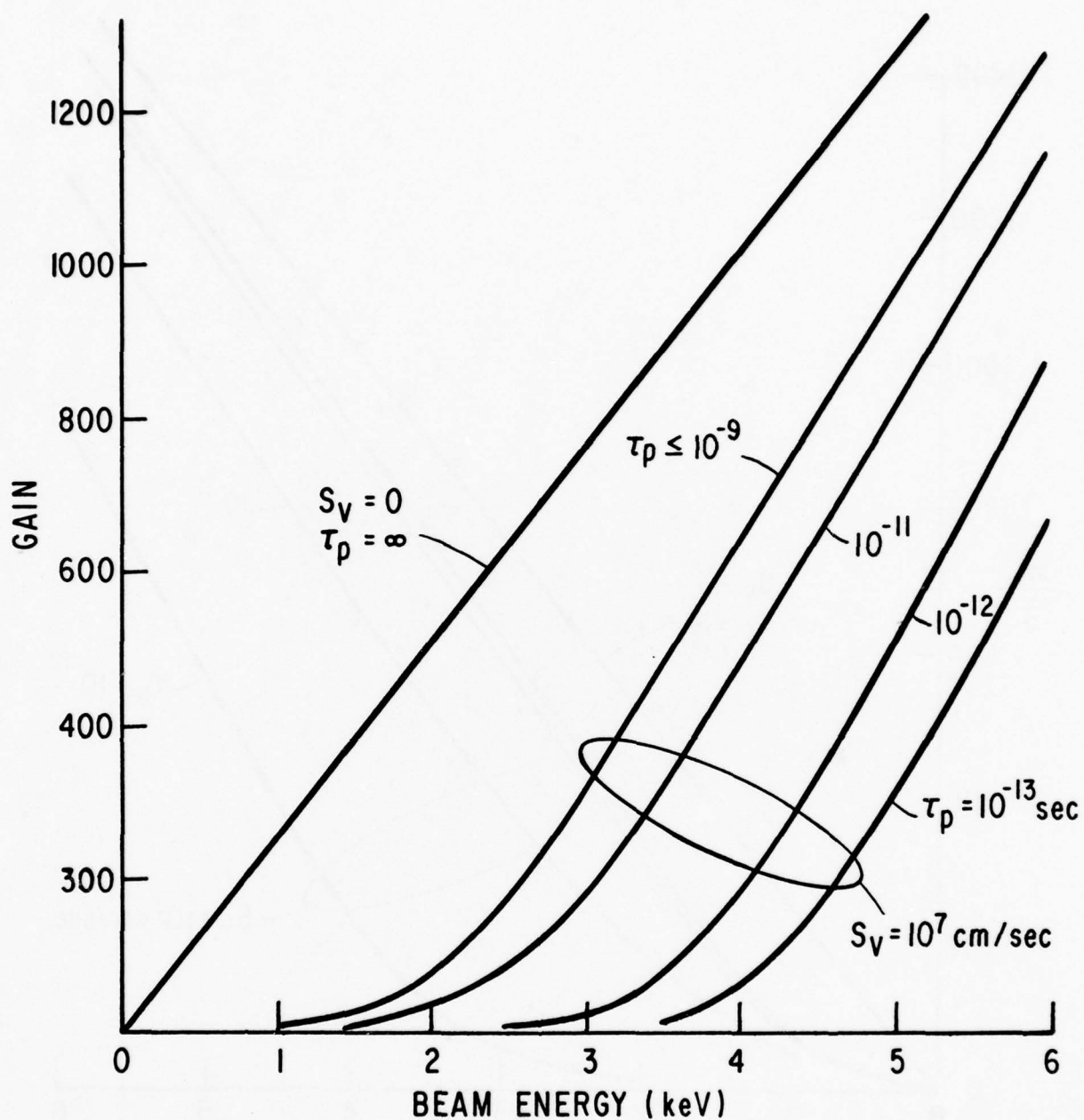
Figure 8. Damage Writing Simulation. [Model prediction of gain vs beam energy for a planar diode fabricated by 100 keV arsenic implantation into silicon. Recombination parameters are (see Figure 1) $d_p = 0.08\ \mu$, $\tau_d = 0.05\ \mu$, and τ_p as defined in Figure 7.]
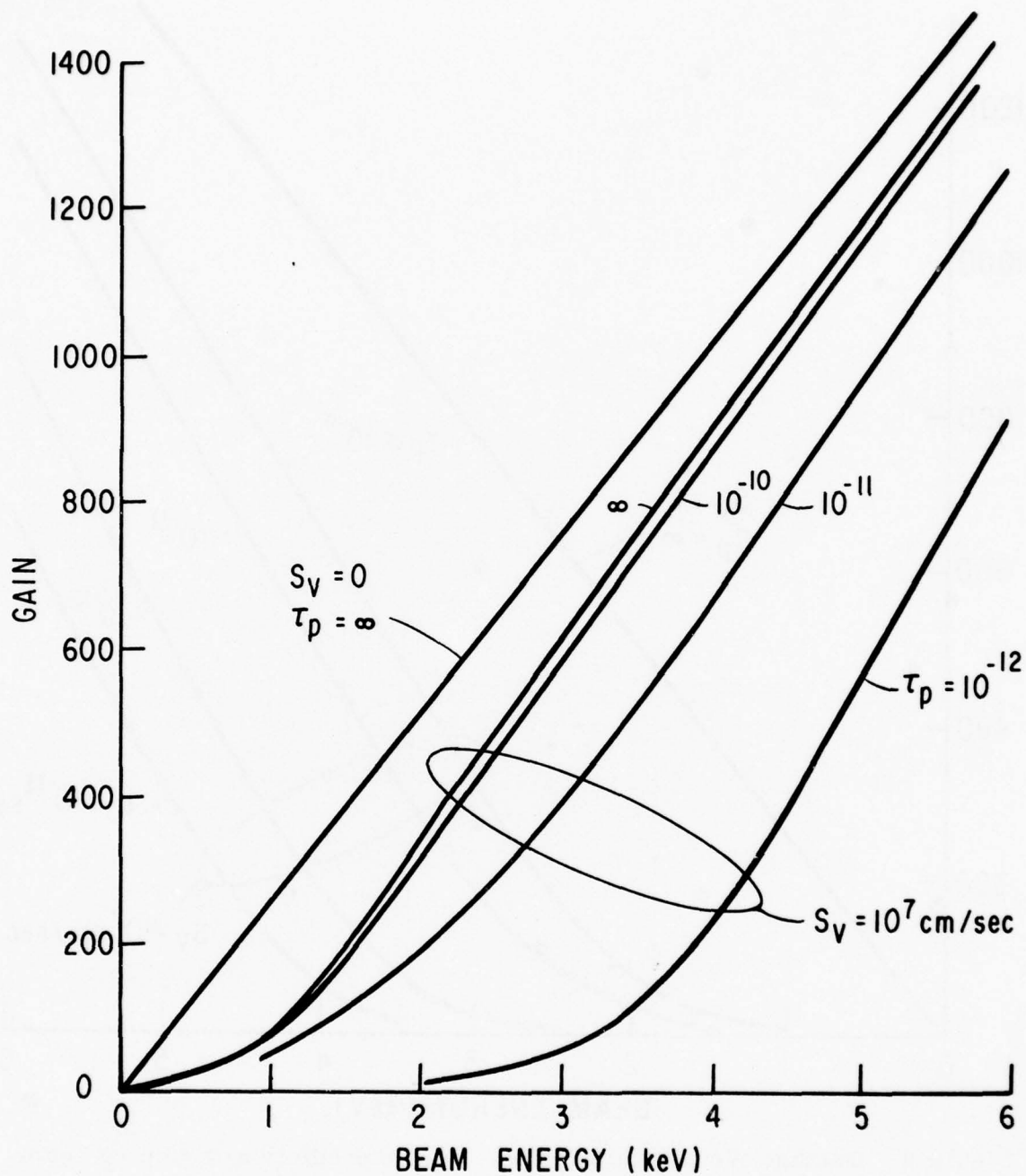
Figure 9. Damage Writing Simulation. [Model prediction of gain vs beam energy for a planar diode fabricated by 100 keV arsenic implantation through 0.08 μ of thermal SiO_2. Recombination parameters are (see Figure 1) $d_p = 0.08\ \mu$, $\sigma_d = 0.05\ \mu$, and τ_p as indicated on the figure.]
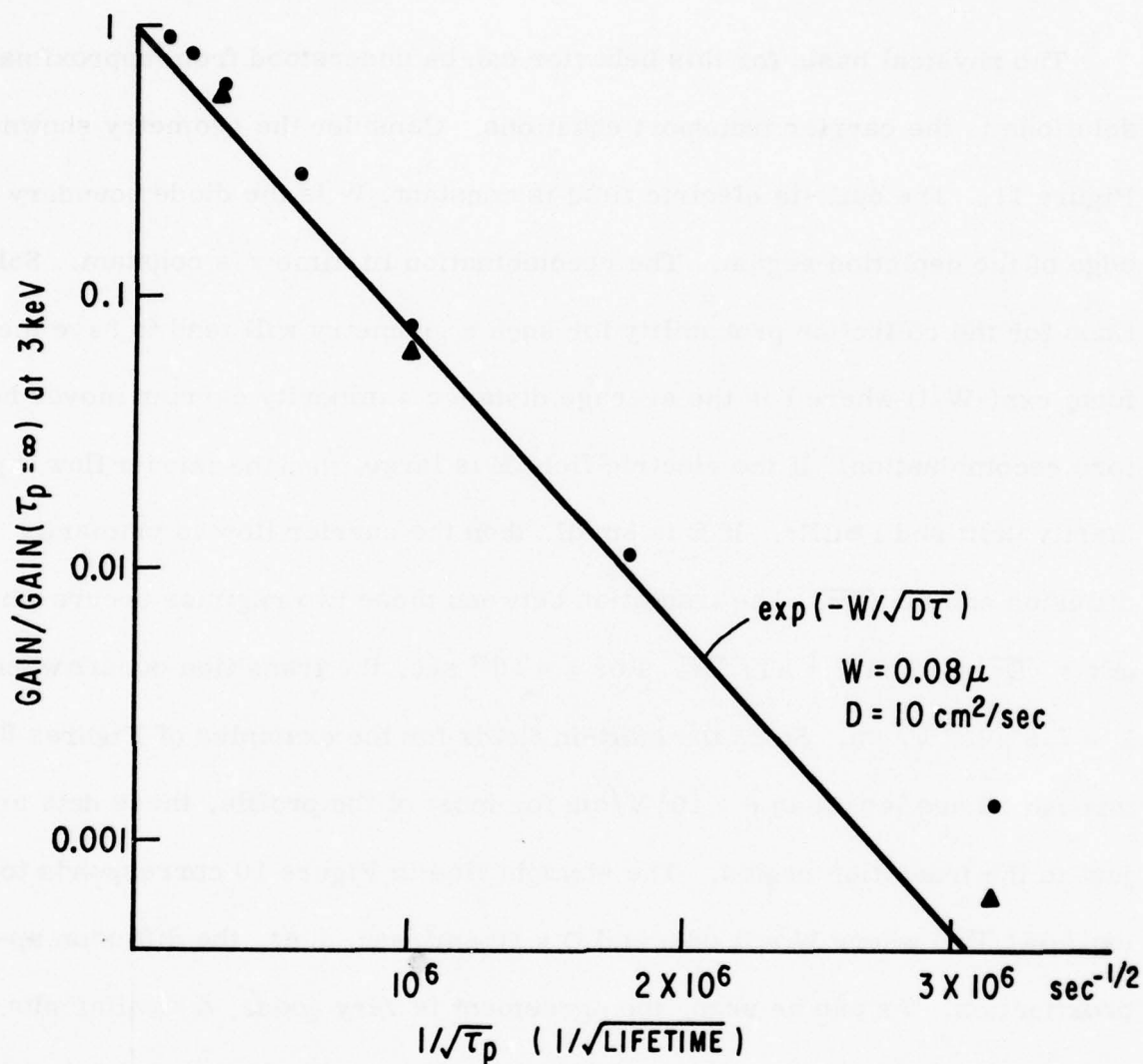
Figure 10. Gain at 3 keV Normalized to the Gain with $\tau_p = \infty$ vs τ_p. (Data from both Figures 3 (▲) and 4 (●). Straight line is the diffusion approximation.)

gain at 3 keV normalized to the gain with $\tau_0 = \infty$ vs $1/\sqrt{\tau_p}$. Data for both types of arsenic diodes are shown, and there is very little difference.

The physical basis for this behavior can be understood from approximate solutions to the carrier transport equations. Consider the geometry shown in Figure 11. The built-in electric field is constant. W is the diode boundary or edge of the depletion region. The recombination lifetime τ is constant. Solutions for the collection probability for such a geometry will tend to have the form exp(-W/l) where l is the average distance a minority carrier moves before recombination. If the electric field E is large, then the carrier flow is primarily drift and $l \cong \mu E \tau$. If E is small, then the carrier flow is primarily diffusion and $l \cong \sqrt{D\tau}$. The transition between these two regimes occurs when $\mu E \tau = \sqrt{D\tau}$ or when $E = kT/\sqrt{D\tau}$. For $\tau = 10^{12}$ sec, the transition occurs when $E = 7.9 \times 10^3$ V/cm. Since the built-in fields for the examples of Figures 8 through 10 are less than 6×10^3 V/cm for most of the profile, these data are just in the transition region. The straight line in Figure 10 corresponds to $\exp(-W/\sqrt{D\tau})$ where $W = 0.08 \mu$ and $D = 10$ cm^2/sec, i.e., the diffusion approximation. As can be seen, the agreement is very good. A similar plot against $1/\tau$ would not give a straight line, and hence this case is best described by the diffusion approximation.

Figure 12 shows a similar calculation for a higher built-in electric field. Here the doping profile was taken as 1.35×10^{18} cm^{-3} exp(-2 $\times 10^6$ cm^{-1} $\times$ z). This gives a constant built-in electric field of 5×10^4 V/cm. The damage profile was the same as the previous example. This field is too high to be

22
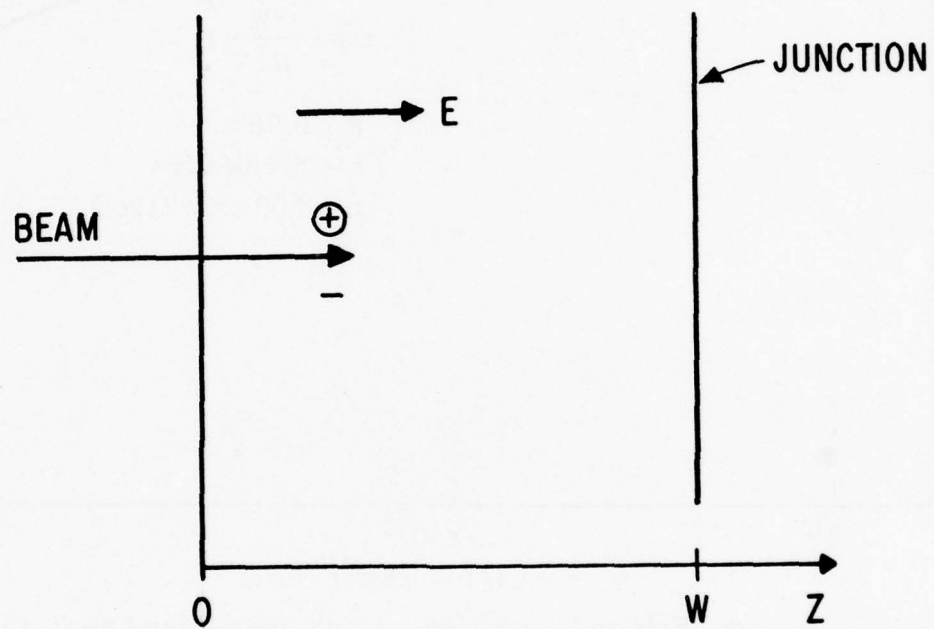
Figure 11. Geometry for Carrier Transport
with Recombination

23
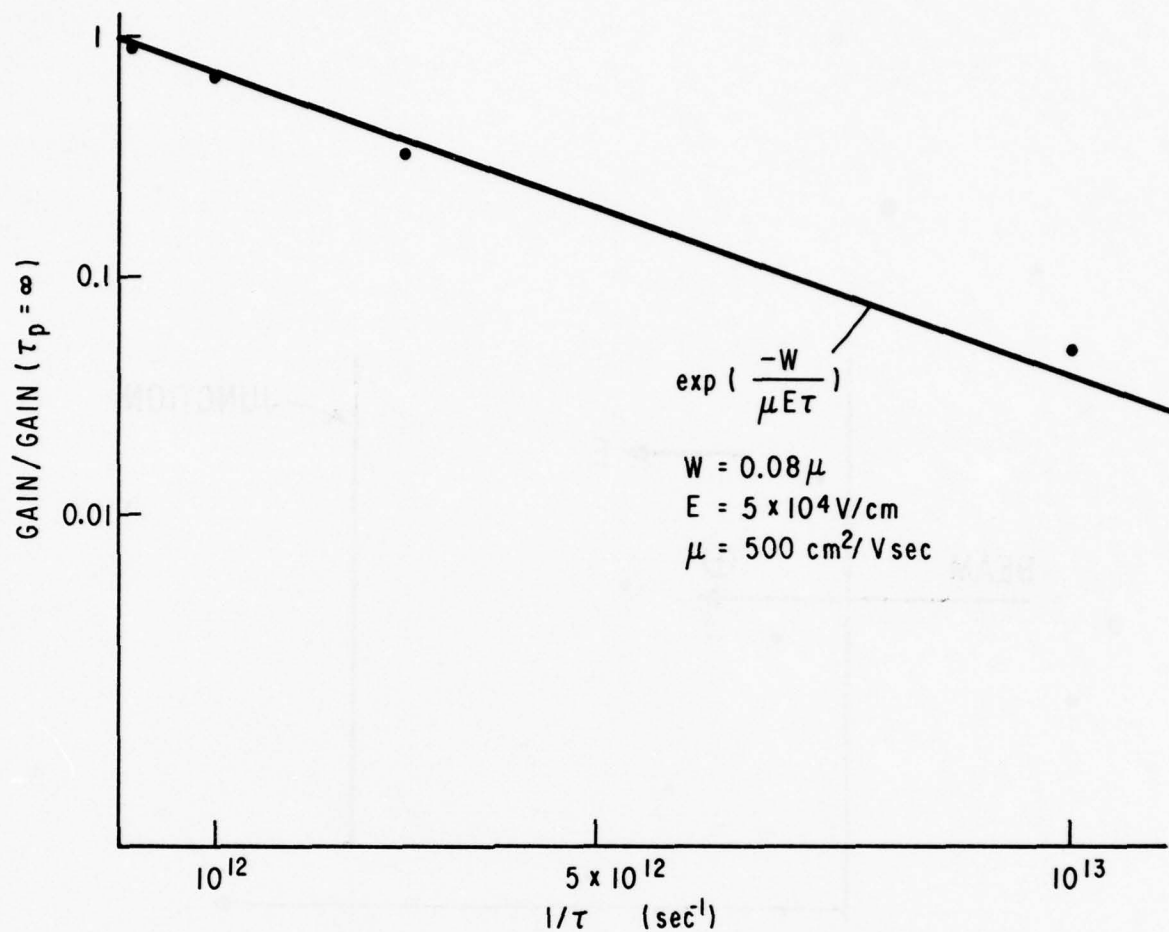
Figure 12. Damage Writing Simulation. (Data normalized as in Figure 4. Built-in electric field 5×10^4 V/cm due to a doping profile 1.35×10^{18} cm^{-3} exp(-2×10^6 cm^{-1}z). Straight line is drift approximation.)

24

physically realizable, since with a mobility of 400 $cm^2/Vsec$ this corresponds

to a drift velocity of 2.5×10^7 cm/sec which is 5 times larger than the maxi-

mum drift velocity of holes in silicon. However, it serves to illustrate a

mathematical point about the solutions. Now the data are plotted against $1/\tau$

which gives a better fit than $1/\sqrt{\tau}$ to a straight line. The solid line corresponds

to $\exp(-W/\mu E\tau)$ with $W = 0.08\,\mu$, 5×10^4 V/cm, and $\mu = 500$ $cm^2/Vsec$.

Based on these calculations, it would be expected that the damage writing

experiments on the arsenic implanted samples would follow the diffusion ap-

proximation, i.e., the normalized gain should be proportional to $\exp(-W/\sqrt{D\tau})$.

Assuming independent and identical recombination centers, $1/\tau$ should be pro-

portional to the number of recombination centers or the implant fluence

F ($1/\tau = KF$). Hence plots of measured log gain vs $\sqrt{F}$ should yield straight

lines, and from the slope, the proportionality constant K can be determined.

Section III

PLANAR DIODE EXPERIMENTS

SILICON SUBSTRATES

During the last quarter, several experiments on silicon planar collection diodes were undertaken to better define this structure with regard to high collection efficiency and reduced diode leakage. The studies included arsenic and boron implantations for formation of planar diodes and studies of annealing treatments and surface treatments.

During the previous quarter, 100 keV As^+ implantation through thermal SiO_2 was identified as a promising technique for producing planar diodes with high collection efficiency. The process which was identified as producing good structures was 100 keV As^+ implantation through 800 Å of thermal SiO_2 at a fluence of 10^{14} cm^{-2} into 10-20 ohm-cm p-type <111> float zone silicon at 7° off axis and room temperature. The annealing cycle used was 770°C for 1 hour in argon. A large number of wafers were implanted using these conditions to verify the process steps employed. These planar diodes will become substrates for writing experiments. Figure 13 shows the gain vs beam energy measurements for one of these samples after anneal at 800°C for 1 hour in argon. As can be seen, the results are variable when measured at different times and were found to be improved by an HF dip. It is believed that the low gain observed initially was due to poor contacts to the wafer. This was a concern from the beginning of the program but the early results did not indicate any severe problems. No corrective measures were undertaken, except the addition of a BHF (buffered hydrofloric acid) dip after anneal to

27

Figure 13. Gain vs Energy Measurements for 100 kV As$^+$ Implanted Planar Diode. (Implantation was for 10^{14} ions/cm^2 through 800 Å oxide into 10-20 ohm-cm p-type <111> silicon. Anneal was for 1 hour in argon ambient at 800 °C.)

remove any existing oxide layer. Some samples are now in process with implanted back contact layers to eliminate this problem in future experiments.

Figure 14 compares the effect of different annealing temperatures. The differences are marginal although the 750°C anneal still seems to produce diodes that exhibit the maximum collection efficiency. If these small differences are real, they are probably due to a slight broadening of the doping profile at the higher temperatures. This reduces the built-in electric field due to the doping gradient.

Four-point probe measurements of the sheet resistance of the implanted n-layer were made on the samples of Figure 14. The results are shown in Table 1. The sheet resistance is a measure of the total active doping concentration in the implanted layer. In order to determine the total active concentration, it would be necessary to make some assumptions about the variation of mobility in the layer due to doping variations and residual damage. However, there is a clear trend indicating higher sheet resistance at the lower anneal temperatures. This indicates the possibility of some residual damage or inactive arsenic at the lower anneal temperatures. However, the gain behavior does not seem to be affected.

Early experiments indicated that high temperature annealing, which can improve diode characteristics, produced undesirably thick dead layers. An experiment was conducted in which a sample originally annealed at 800°C for one hour (found optimum for implants through clean surfaces) was then given a 10 minute, 950°C "hot shot," hopefully to improve the diode. As can be
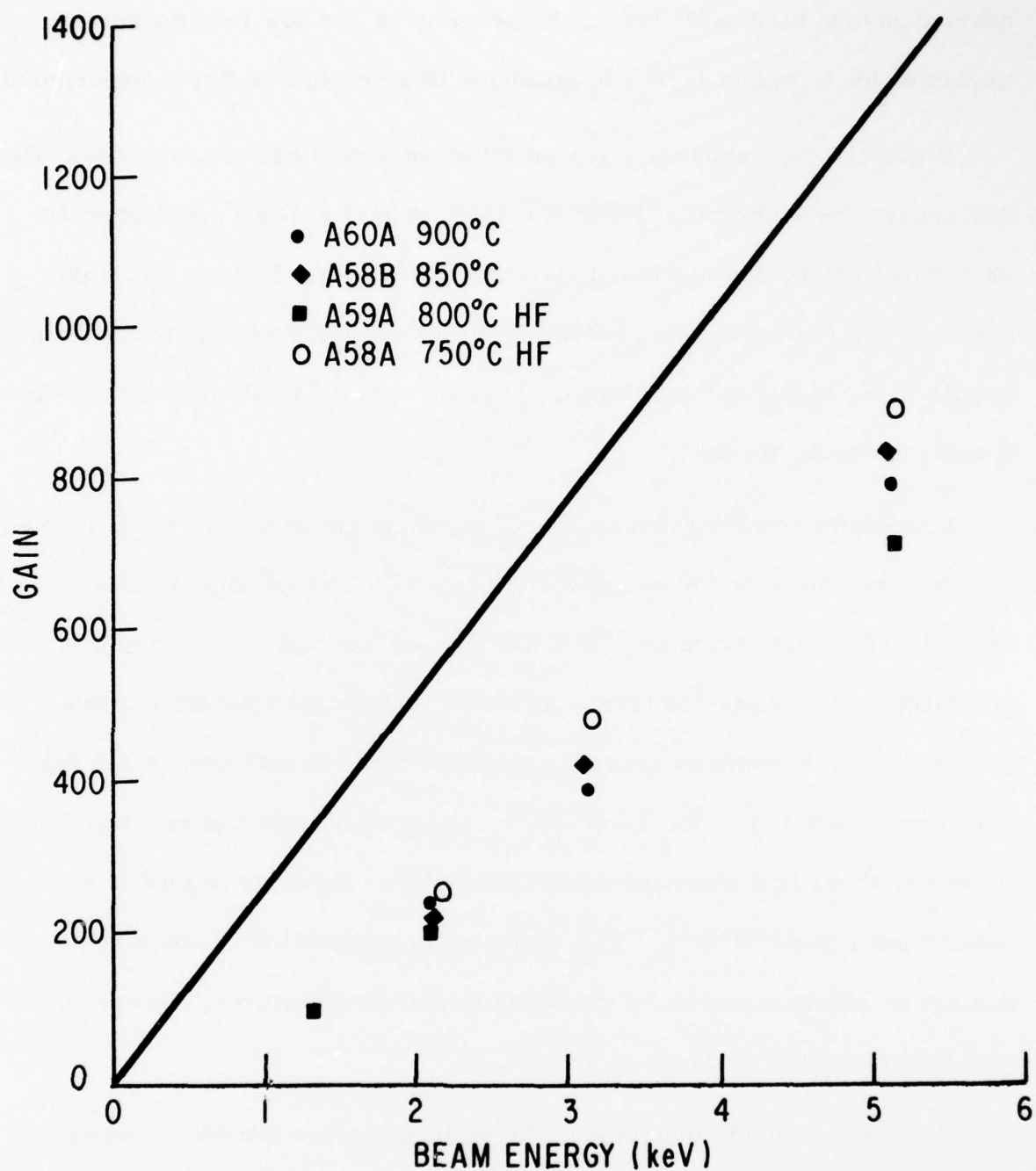
Figure 14. Gain vs Energy Measurements for Planar Diodes. (100 kV As$^+$ implants at room temperature 7° off axis to fluences of 10^{14} into 10-20 ohm-cm p-type <111> silicon. All anneals were of 1 hour duration in argon ambient.)

TABLE 1

FOUR-POINT PROBE MEASUREMENTS FOR PLANAR DIODES
ANNEALED ONE HOUR IN ARGON, IMPLANTED WITH 100 kV As$^+$
TO FLUENCES OF 10^{14} ions/cm^2 THROUGH 800 Å THERMAL SiO$_2$

Sample	Anneal Temperature (°C)	Sheet Resistivity (ohm/square)
A58A	750	2253
A59A	800	1985
A58B	850	1886
A60A	900	1736

seen in Figure 15, the "dead layer" thickness was not optimum and the diode was noisy and not of high quality.

Since it is possible that a p$^+$ surface will have better writing properties than an n$^+$ surface, there is a continuing interest in developing a p$^+$ on n planar diode collection diode as well as the n$^+$ on p diode now under development. Earlier work during the first quarter with boron implants gave poor results. Based on the modeling and experimental work with As$^+$ implanted samples, it is now known that a high built-in electric field at the surface is required for high gain. This field can be achieved by producing a steep doping gradient near the surface. One way to achieve a doping gradient near the surface is to implant through an oxide film of sufficient thickness to put the peak of the implant distribution at or on the SiO$_2$ side of the Si-SiO$_2$ interface. This has been found to significantly improve the arsenic implanted results (see Second Quarterly Report). To test this method, boron samples were prepared by room temperature boron implantation at 50 keV through
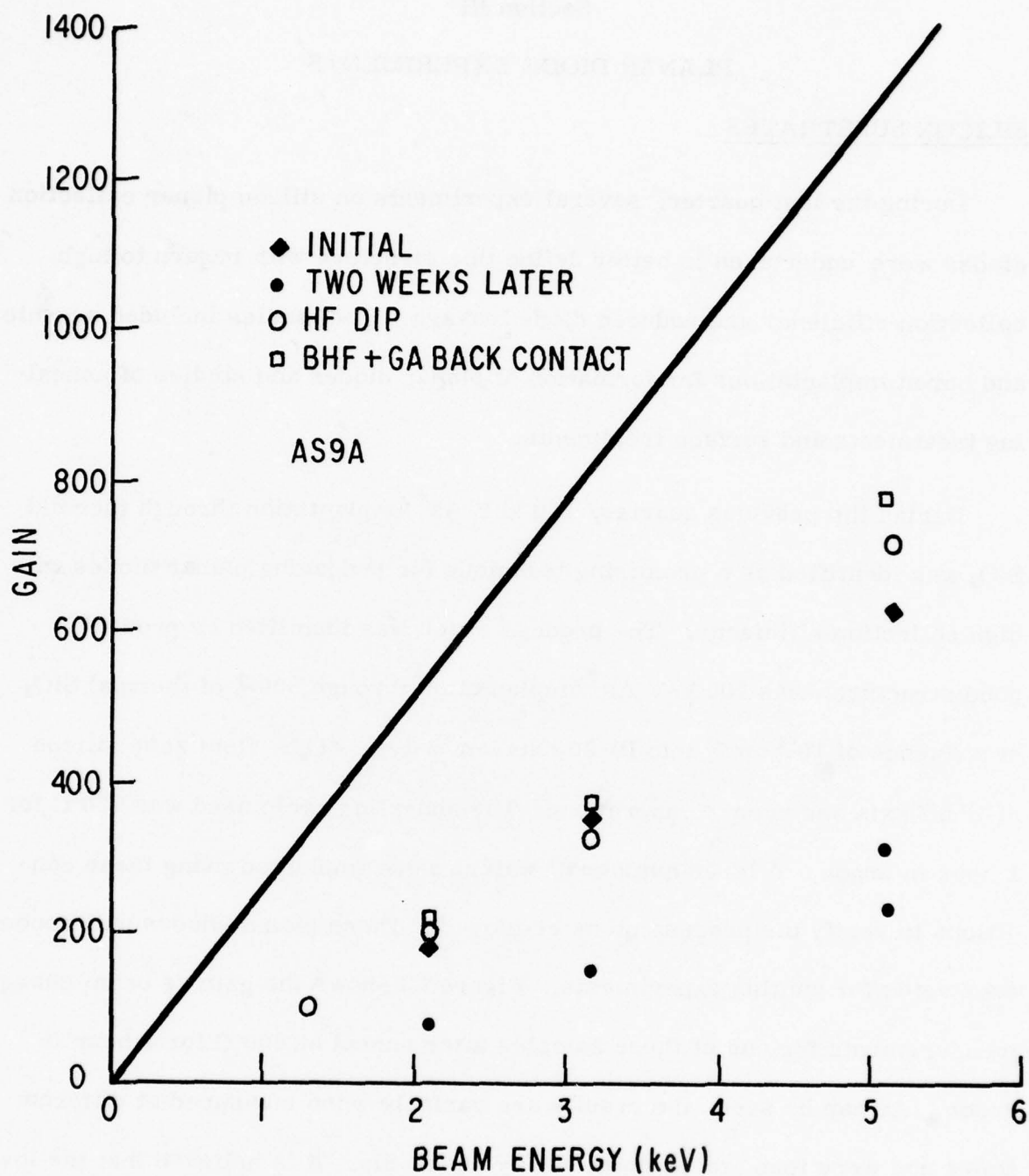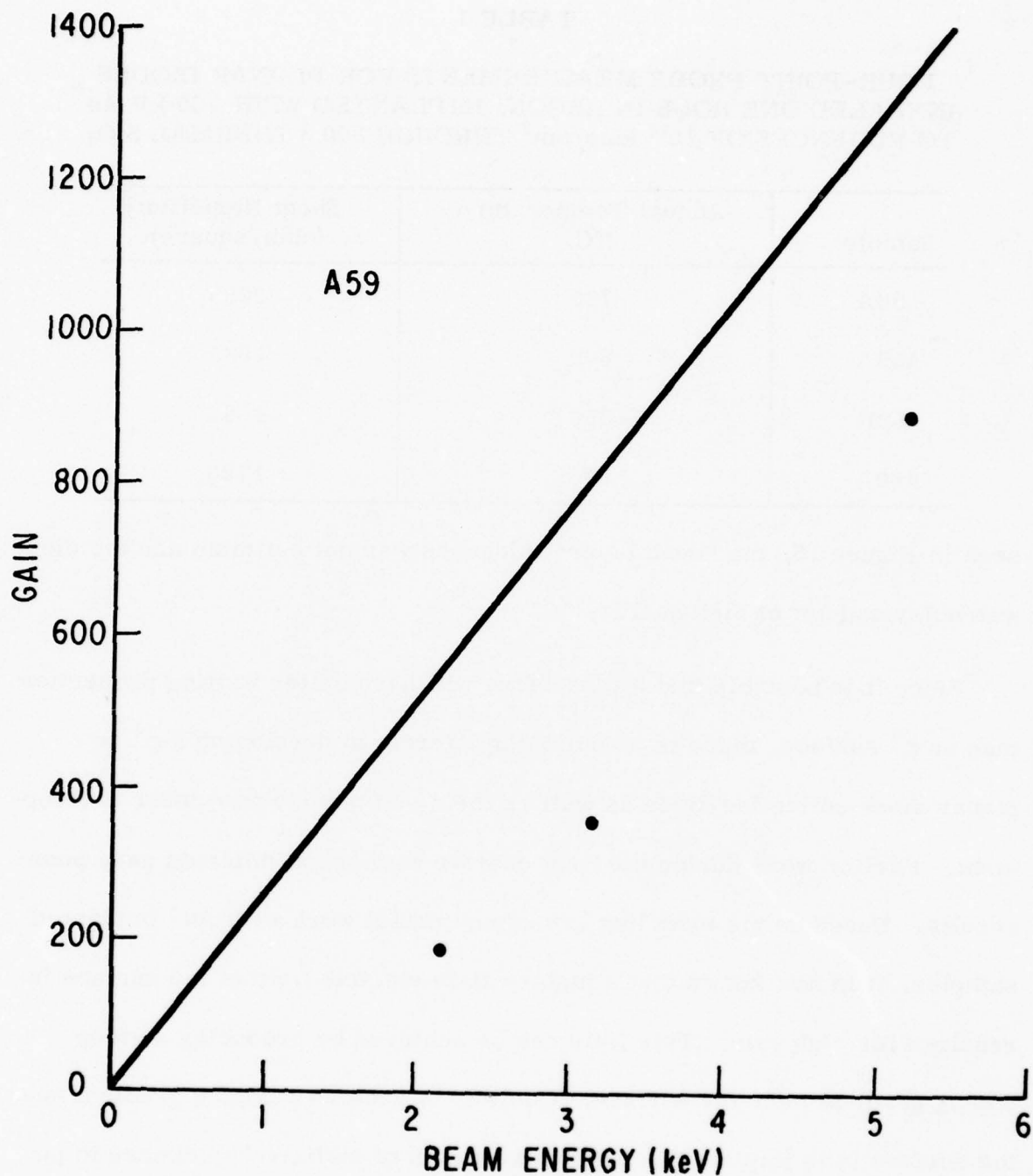
Figure 15. Gain vs Energy Measurements for 100 kV As⁺ Implanted Planar Diode. (Implantation was for 10^{14} ions/cm² through 800 Å oxide into 10-20 ohm-cm p-type <111> silicon. Anneal was for 1 hour at 800 °C, then 10 minutes at 950 °C in argon ambient.)

0.26 μ of thermal SiO_2. The fluence was 10^{15} cm^{-2}, 7° off axis. The material was 10-30 ohm-cm p-doped <111> float zone silicon. The samples were annealed at 900°C for 1 hour in argon to maximize the number of active sites as well as to remove radiation damage. Boron is known to require a relatively high temperature to activate all the boron atoms.

Figure 16 shows the measured gain vs beam energy. The results are very good with the gain at 2 keV as high or higher than for any of the arsenic samples. Data taken on two different days are shown. These look like very attractive substrate planar diodes. Further experiments on this type of structure are planned for the next quarter. As discussed in a following section, a p$^+$ on n structure may have some advantages for writing depending upon the writing mechanisms that are actually taking place.

To understand the reason for these good results, the gain behavior was modeled using the carrier transport model developed during the second quarter. The doping profile used is shown in Figure 17. This is based primarily on the experimentally measured doping profile for 50 keV boron implants at 10^{15} cm^{-2} at room temperature after a 30 minute anneal at 900°C. [2] The solid points are some of the experimental points measured by Crowder et al. [2] by radioactive tracer techniques. Similar profiles have been measured by various methods for 40 or 50 keV boron implants by other workers [3, 4, 5]. The steeper part of the profile is inferred primarily from Reference 3.

33
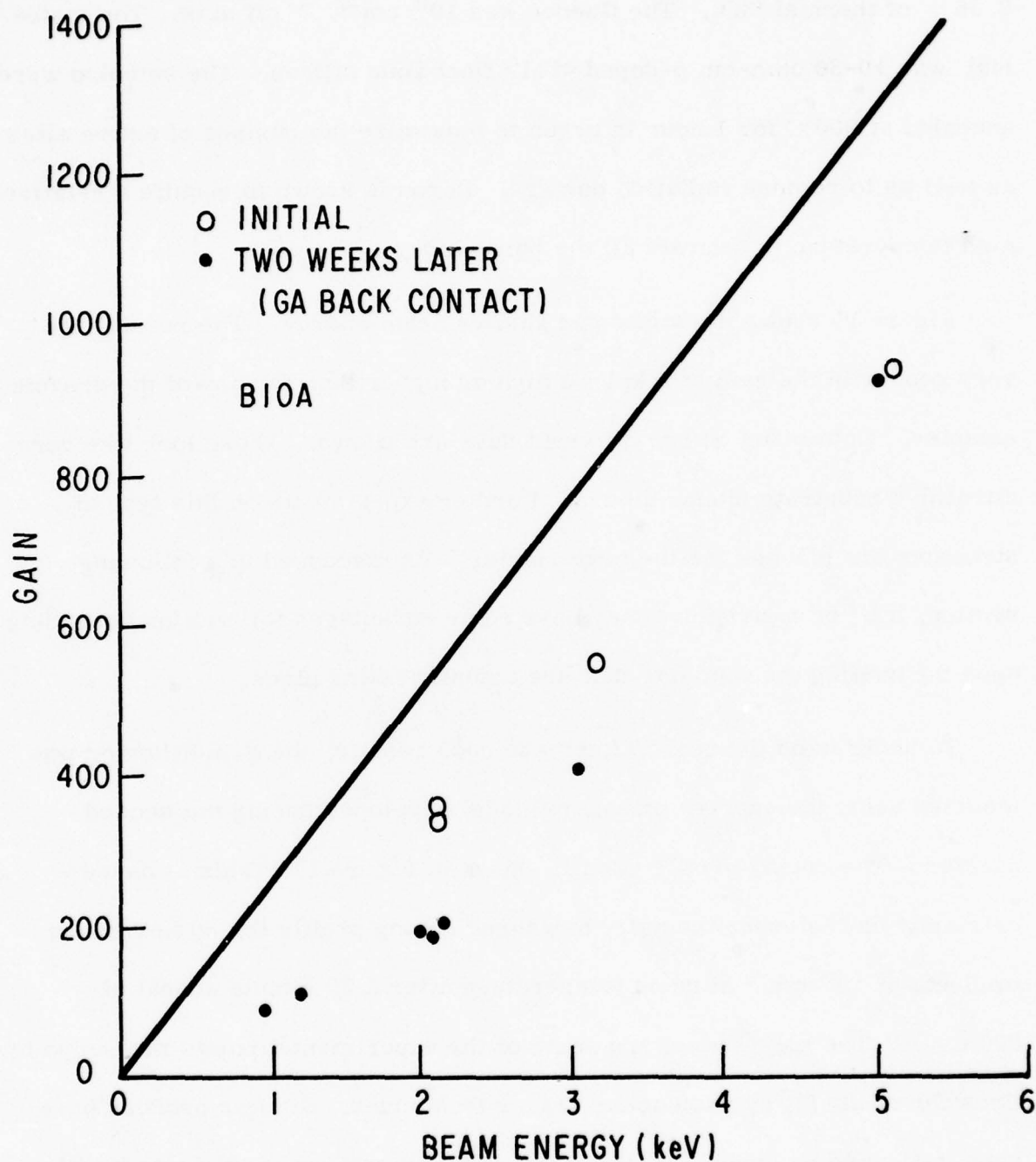
Figure 16. Gain vs Energy Measurements for 50 kV B$^+$ Implanted Planar Diode. (Implantation was for 10^{15} ions/cm^2 through 2600 Å oxide into 10-30 ohm-cm n-type <111> silicon. Annealing was for 1 hour at 900 °C in argon ambient.)
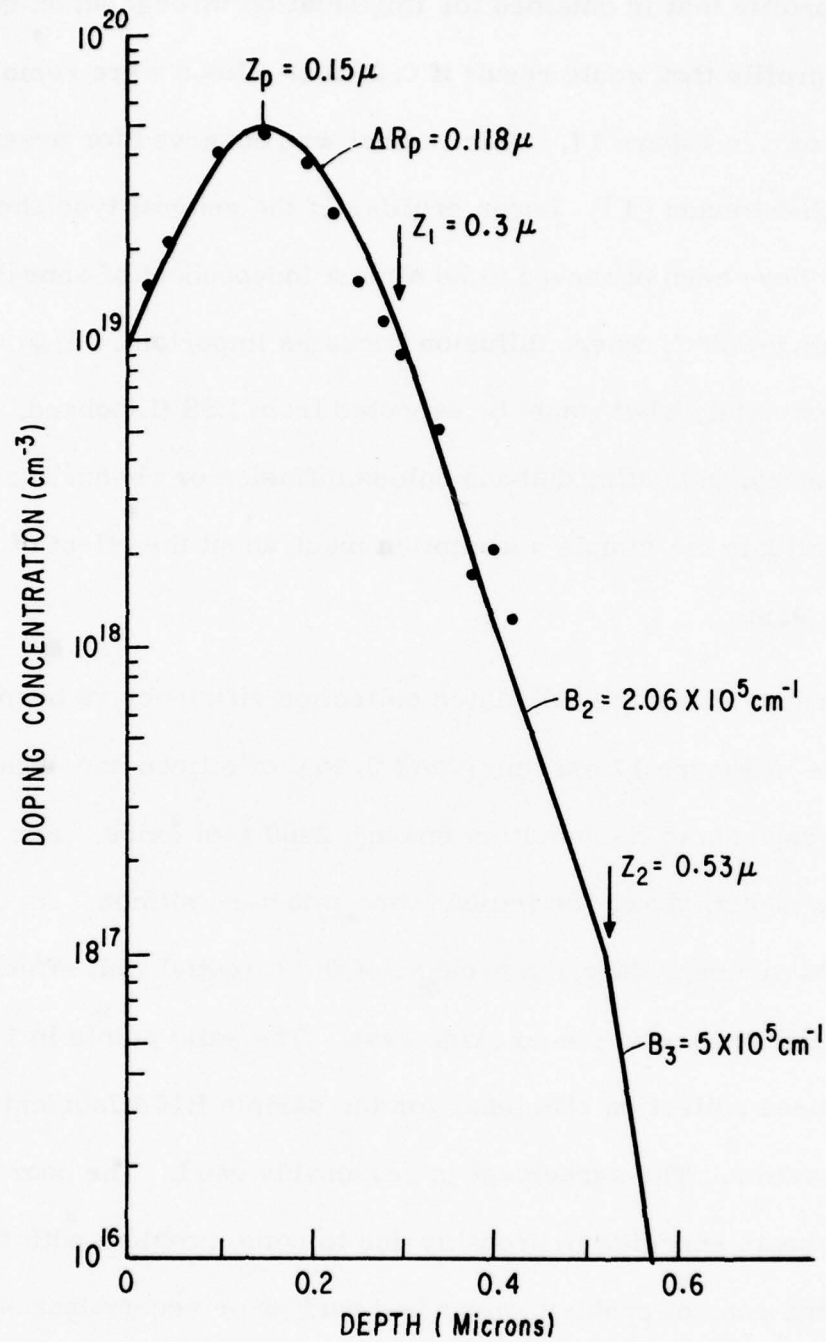
Figure 17. Doping Profile Used for Model Calculation
of Gain vs Beam Energy for 50 keV Boron
Implanted Sample (B10A) Described in Text.
(Experimental points (•) from Crowder et al.
[Ref. 2].)

The profile that is obtained for implantation through an oxide is assumed
to be the profile that would result if $0.26\,\mu$ of silicon were removed from the
profile shown in Figure 17. This is what was observed for arsenic implanta-
tion by Schwettmann [1]. Boron profiles of the general type shown in
Figure 17 have been observed to be almost independent of annealing tem-
perature up to 950°C, where diffusion becomes important. Also, the profiles
are approximately what would be expected from LSS (Lindhard, Scharff,
Schiøtt) theory, indicating that anomalous diffusion or channeling processes
might invalidate the simple assumption made about the effect of the oxide
during implant.

Figure 18 shows the calculated collection efficiency vs beam energy for
the profile in Figure 17 assuming that $0.26\,\mu$ of silicon has been removed.
This corresponds to implantation through 2600 Å of oxide. For comparison,
one curve is also shown for implantation into bare silicon. As can be seen,
the results are very different because of the potential well effect of the pro-
file near the surface in the no oxide case. The solid points in Figure 18 are
the measured collection efficiency for the sample B10A fabricated as de-
scribed earlier. The agreement is reasonably good. The poor agreement
at higher beam energies is probably due to some problem with the diode,
possibly the contact problem described earlier or recombination in the diode
depletion region on the reverse side of the diode. The higher gain data shown
in Figure 16 may reflect an unusually lower recombination velocity or a
measurement error. This high collection efficiency could not be repeated

36

and these data points were not included in Figure 18.   Further study will be

necessary to fully characterize this structure.   However, the initial results

are very encouraging.
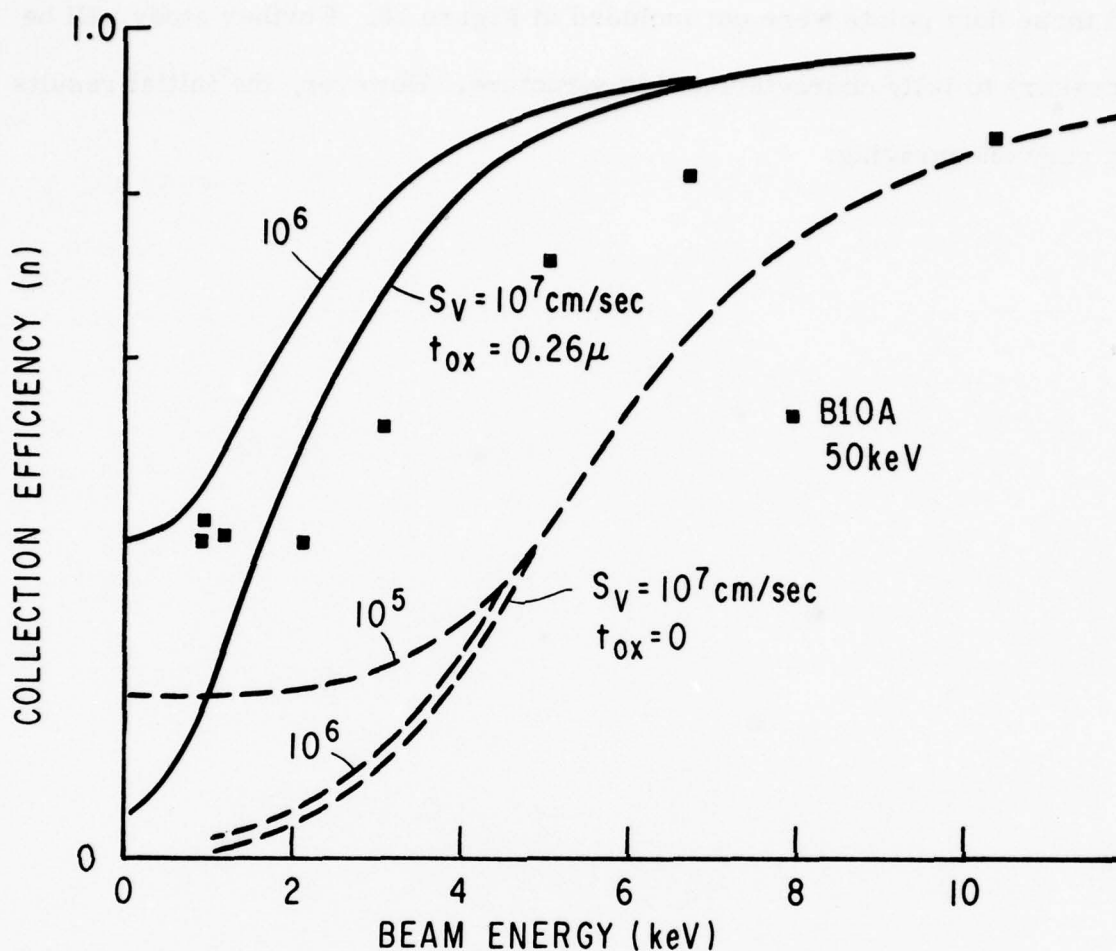
Figure 18. Calculated Collection Efficiency vs Beam Energy Compared
to Measured Points on Sample B10A. (Model calculations are
based on the carrier transport model and the profile in Fig-
ure 5. The solid curves are for implant through a 0.26 μ
oxide and the dotted curve for implant into bare silicon. Prep-
aration of sample B10A is described in the text.)

SECTION IV

ION WRITING

Experimental archival memory devices written using a variety of implanted inert ions for writing have corroborated the second quarter suggestion that ion damage, as well as ion doping, may be a viable means of recording information on the target for electron beam readout.

Implants of Ne^+, Ar^+, Xe^+, Kr^+, as well as Ta^+, and the previously studied He^+, were performed to gain more information as to which ionized atoms or molecules are best suited for writing as well as the actual mechanisms by which the target is altered sufficiently to result in modulation of readout current.

For these studies, planar diodes were prepared from 10-20 ohm-cm p-type <111> silicon, which was implanted with 100 keV As^+ ions, 7° off axis at room temperature to a fluence of 10^{14} ions/cm^2. After annealing for one hour at 770 °C in an argon gas ambient, mesa diodes were formed on the surface using a silicon etch. The samples were then coated with resist and patterned using the standard Air Force test pattern. These samples were then implanted with He^+, Ne^+, Ar^+, Xe^+, and Kr^+ to fluences of 5×10^{10}, 10^{11}, 10^{12}, and 10^{13} ions/cm^2 at energies of 30, 55, 100, 270, and 195 keV, respectively. Except for the deep penetrated helium (limited to ~ 0.2 μ at lowest available in-house ion implantation machine energy), ion beam energies were selected to put the estimated peak of the ion range distribution at ~ 0.1 μ. The resist mask was stripped in hot sulfuric acid (the resist surface cross-links as a result of the

39

exposure to radiation, making even thick coatings difficult to remove), and the wafers cleaned for insertion in the scanning electron microscope.

Figure 19 indicates the results of SEM (scanning electron microscope) studies of gain as a function of reading electron beam energy for various writing fluences of 55 keV Ne^+ ions. Open data points show results for measurements made in unwritten areas on the planar diode surface, while solid points refer to written areas receiving the indicated writing fluence. Even for as low a fluence as 5×10^{10} ions/cm^2, good readout is possible, as seen in the scanning electron micrograph of Figure 20, showing a planar diode signal, and in Figure 21, showing a scope trace of written and unwritten bars. The reverse bias characteristic of the planar diode for this sample is shown in Figure 22.

The results of a parallel set of experiments using 100 keV Ar^+ are shown in Figure 23. Again, good gain modulation is apparent, even at the lowest fluence. Similar results for Xe^+, Kr^+, and Ta^+ are given in Figures 24, 25, and 26 with the He^+ data following in Figure 27.

A number of other writing experiments are either already underway or being contemplated for completion during the fourth quarter. The goal is not only the selection of appropriate ion writing species and implant conditions, but also the determination of the actual mechanisms at work which result in written areas easily read out by the electron beam.

In creating ion affected areas which trap the electron beam generated carriers, several effects may be simultaneously at work. The interaction

Figure 19. Gain vs Electron Beam Energy Measurements for Written and Unwritten Areas. [Formed by implantation of 55 keV Ne+ into surfaces of planar diodes formed by 100 keV As$^+$ implantation in 10-20 ohm-cm p-<111> silicon, annealed at 770 °C 1 hour in argon ambient. (Solid points indicate written areas; open points indicate unwritten areas.)]

41
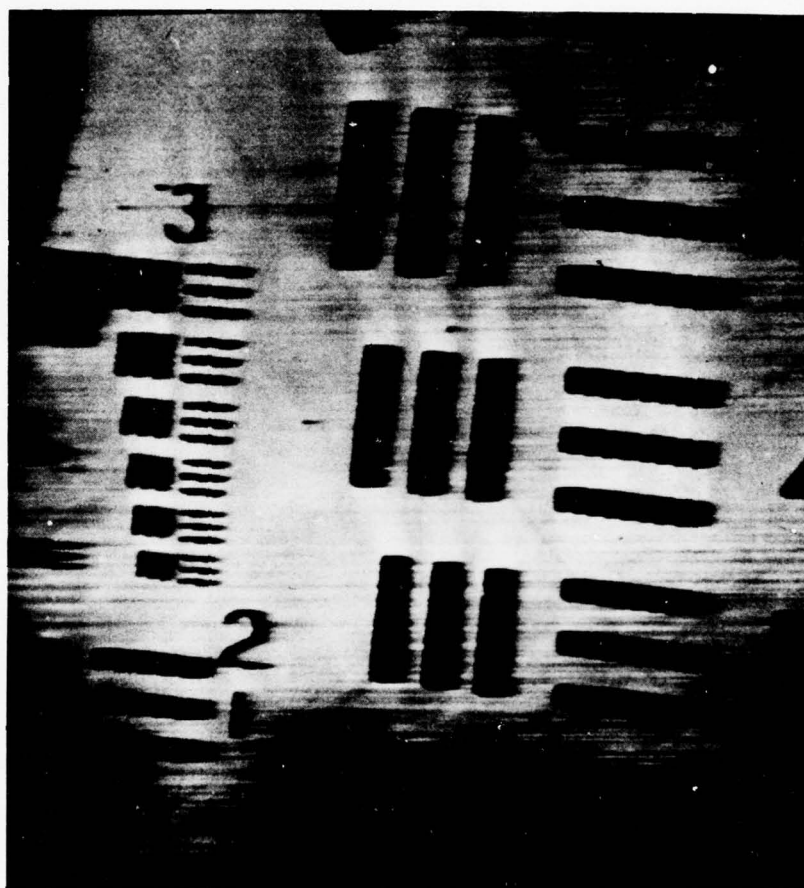
Figure 20. Scanning Electron Micrograph Showing
Collection Diode Signal at 3 keV for Sam-
ple A-25A, Written with 5×10^{10} ions/cm^2
55 keV Ne^+
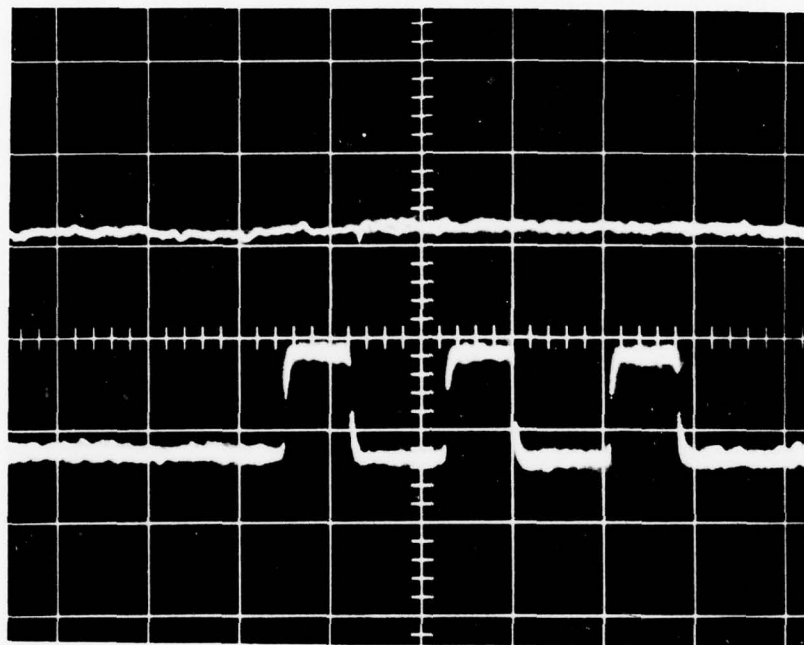
Figure 21. Scope Trace Showing Collection Diode Signal Read at 3 keV from Sample A25A, Written with 5×10^{10} ions/cm^2 55 keV Ne$^+$
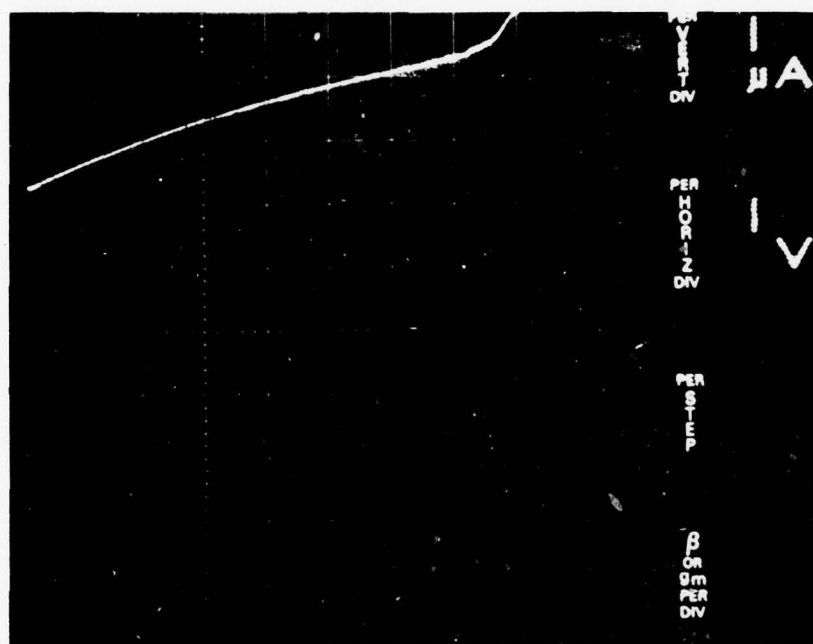
Figure 22. Reverse Bias Characteristic of Planar Collection Diode of A25A.
(Formed by 100 keV As+ implant annealed at 770 °C 1 hour in argon
gas ambient.)
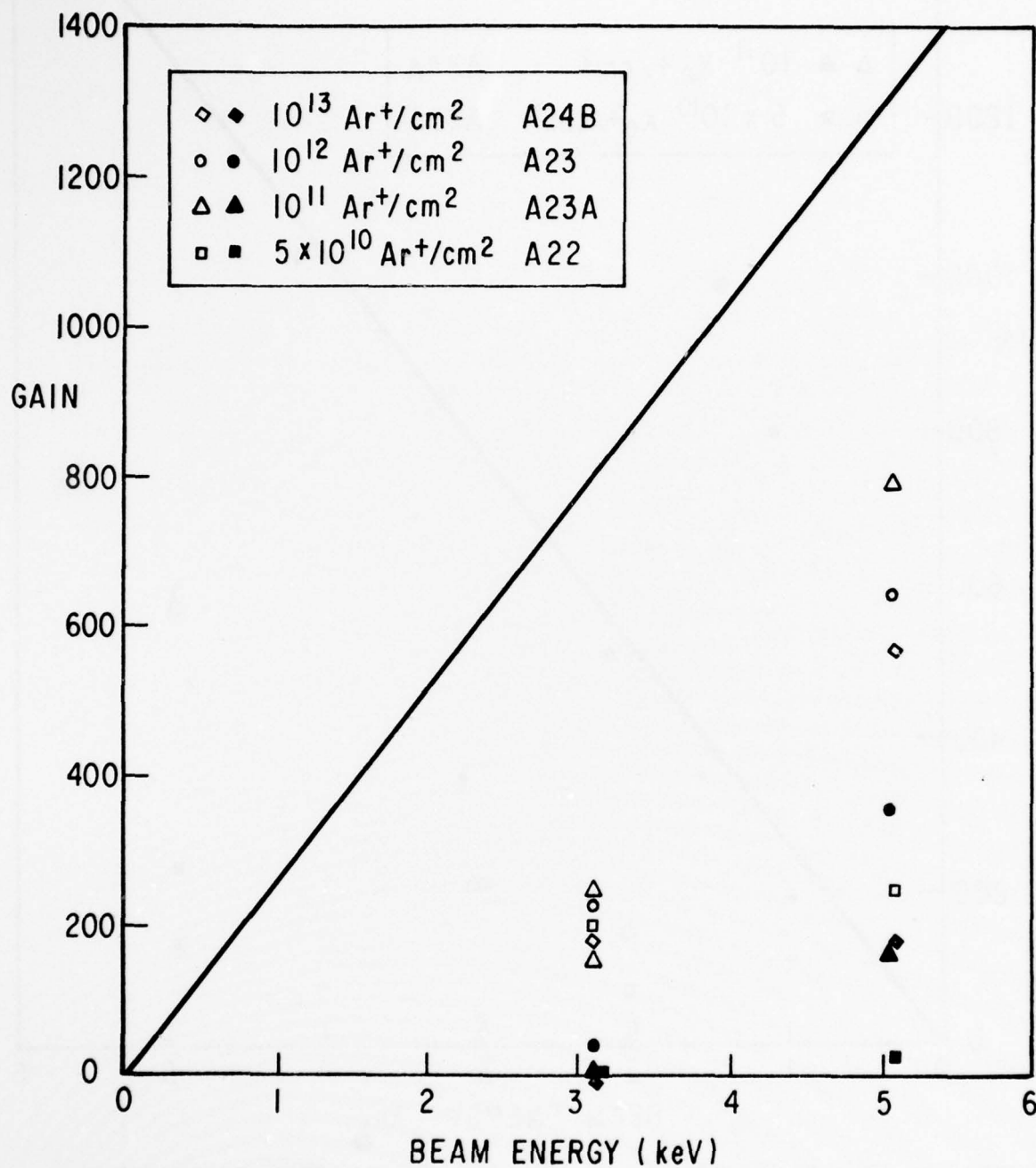
Figure 23. Gain vs Electron Beam Energy Measurements for Written and Unwritten Areas. [Formed by implantation of 100 keV Ar+ into surfaces of planar diodes formed by 100 keV As+ implantation at 10-20 ohm-cm p-<111> silicon, annealed at 770 °C 1 hour in argon ambient. (Solid points indicate written areas; open points indicate unwritten areas.)]

45
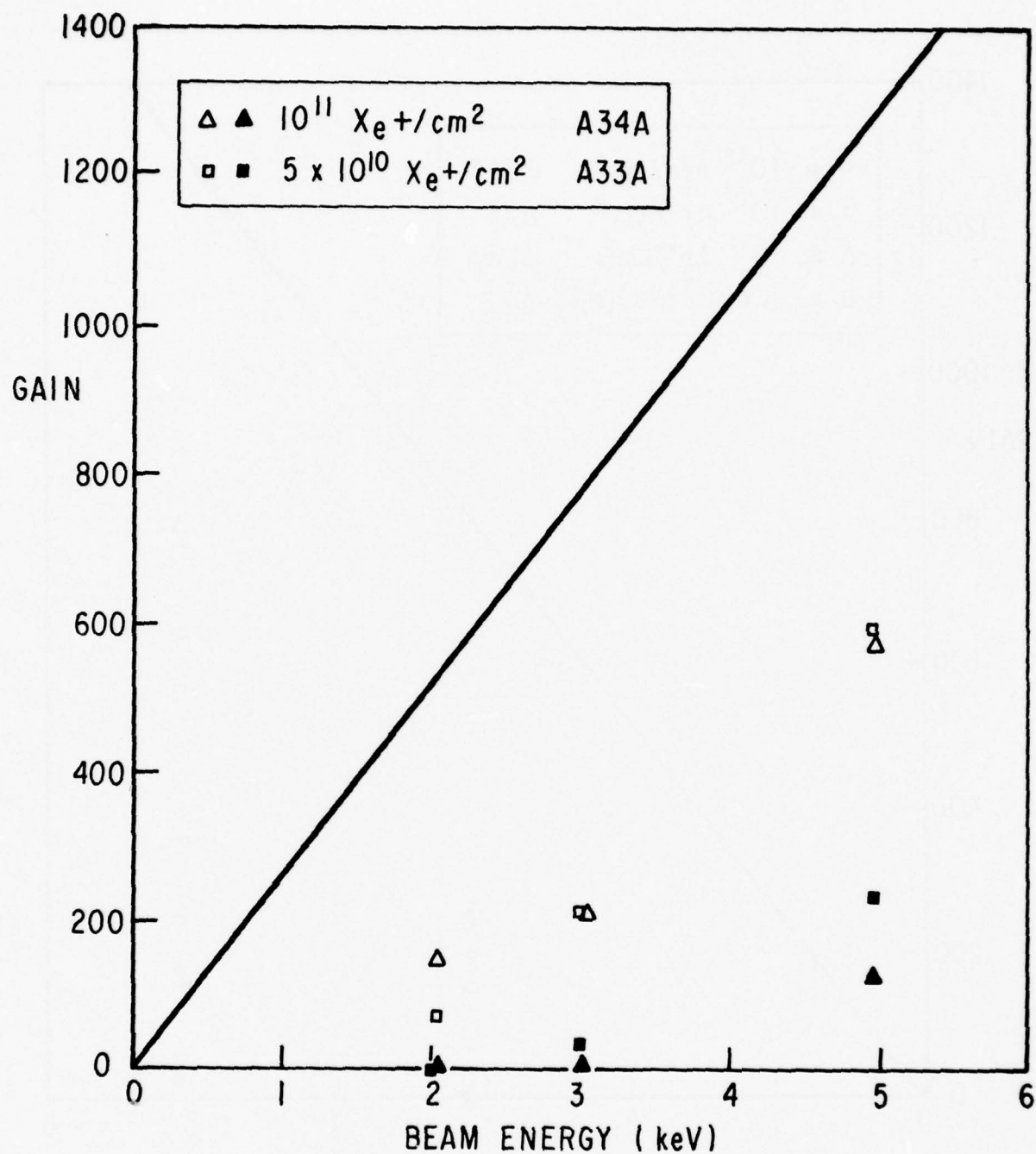
Figure 24. Gain vs Electron Beam Energy Measurements for Written and Unwritten Areas. [Formed by implantation of 270 keV Xe+ into surfaces of planar diodes formed by 100 keV As+ implantation in 10-20 ohm-cm p-<111> silicon, annealed at 770 °C 1 hour in argon ambient. (Solid points indicate written areas; open points indicate unwritten areas.)]

46
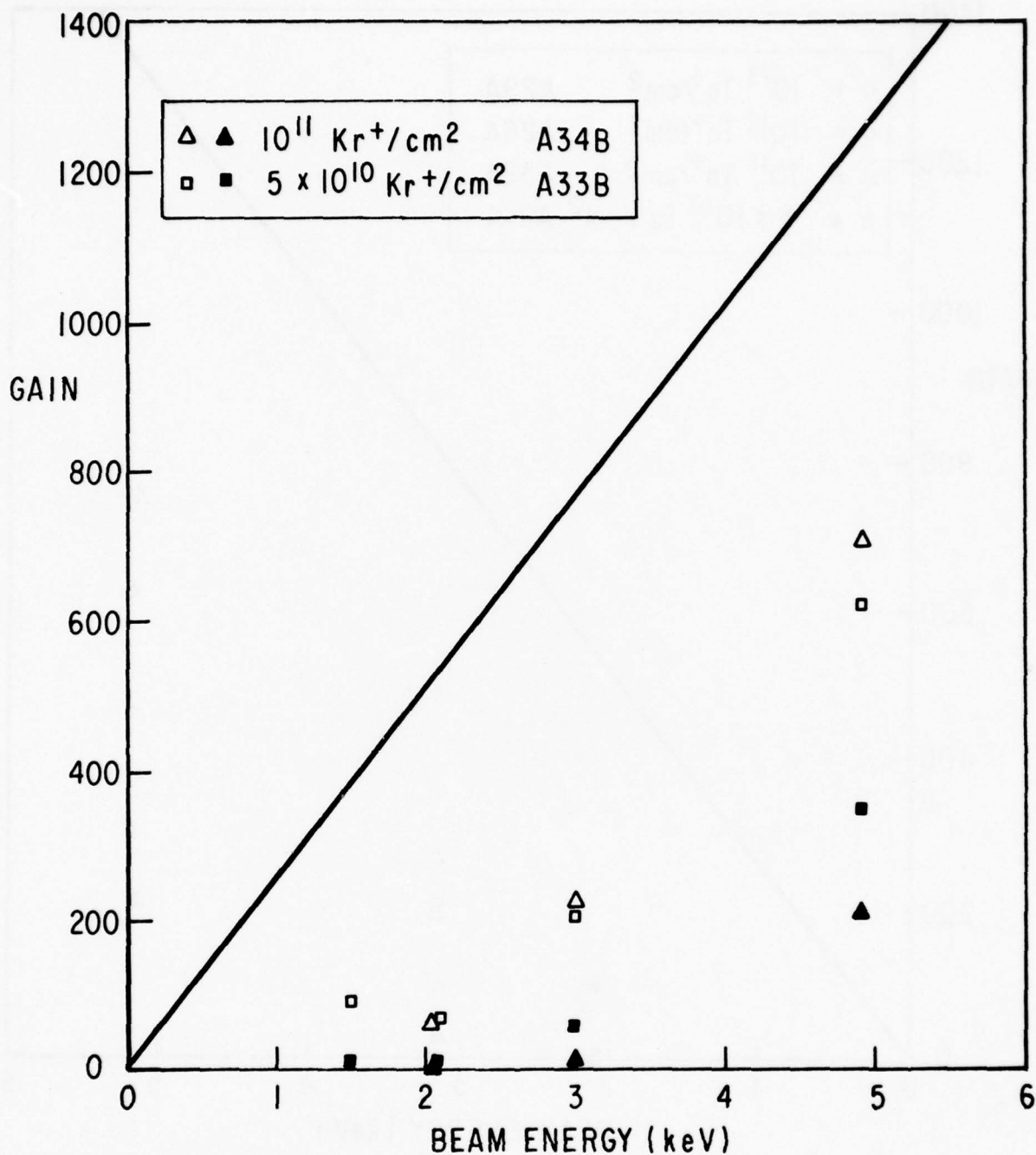
Figure 25. Gain vs Electron Beam Energy Measurements for Written and
Unwritten Areas. [Formed by implantation of 195 keV Kr+
into surfaces of planar diodes formed by 100 keV As+ implan-
tation in 10-20 ohm-cm p-<111> silicon, annealed at 770 °C
1 hour in argon ambient. (Solid points indicate written areas;
open points indicate unwritten areas.)]
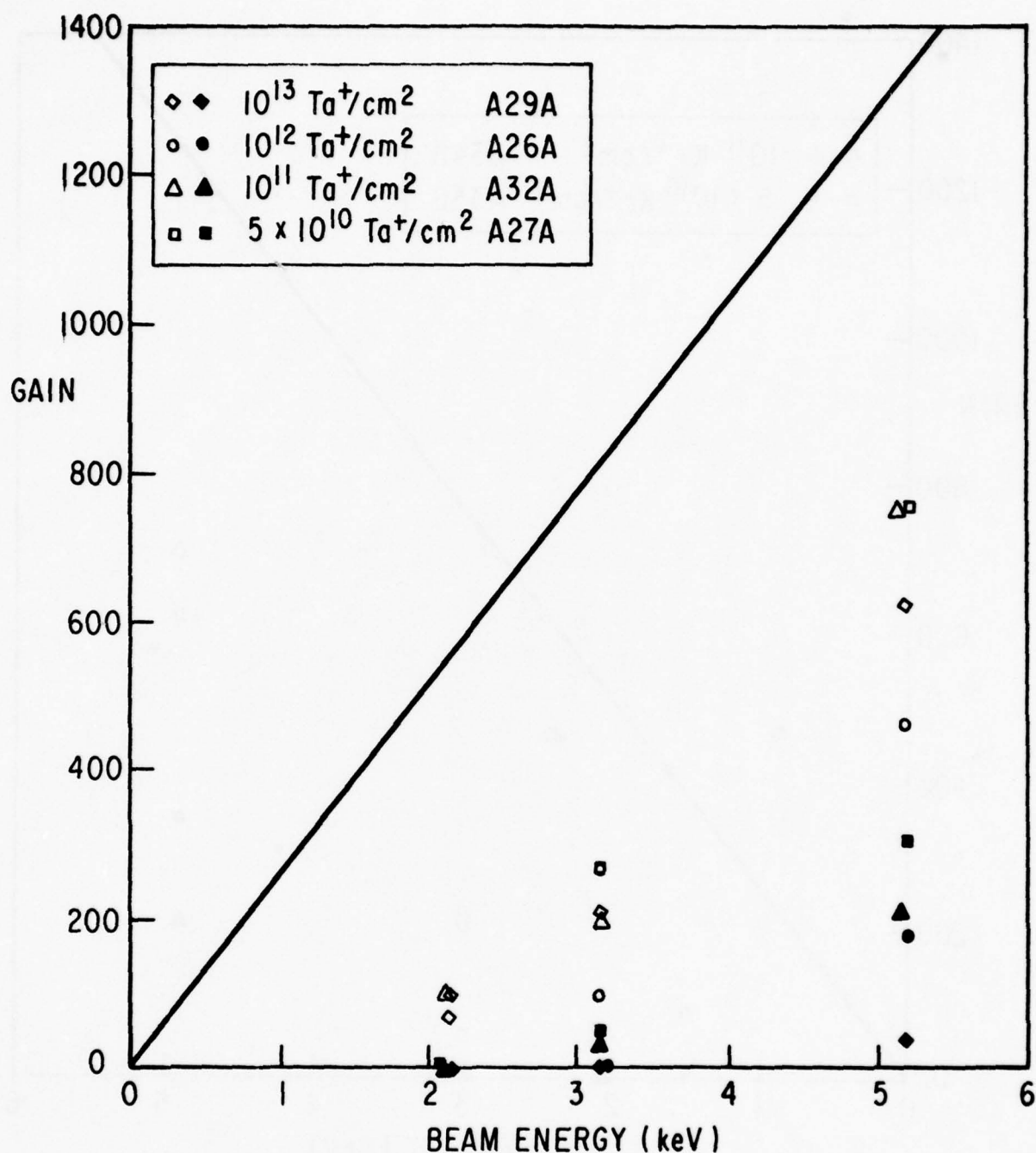
Figure 26. Gain vs Electron Beam Energy Measurements for Written and Un-
written Areas. [Formed by implantation of 340 keV Ta+ into sur-
faces of planar diodes formed by 100 keV As+ implantation in
10-20 ohm-cm p-<111> silicon, annealed at 770 °C 1 hour in argon
ambient. (Solid points indicate written areas; open points indicate
unwritten areas.)]

48

GAIN

1400

1200

◇ ● 10^{13} He$^+$/cm^2 A20
○ ● 10^{12} He$^+$/cm^2 A19
△ ▲ 10^{11} He$^+$/cm^2 A19A
□ ■ 5 x 10^{10} He$^+$/cm^2 A24A

1000

800

600

400

200

0

0   1   2   3   4   5   6
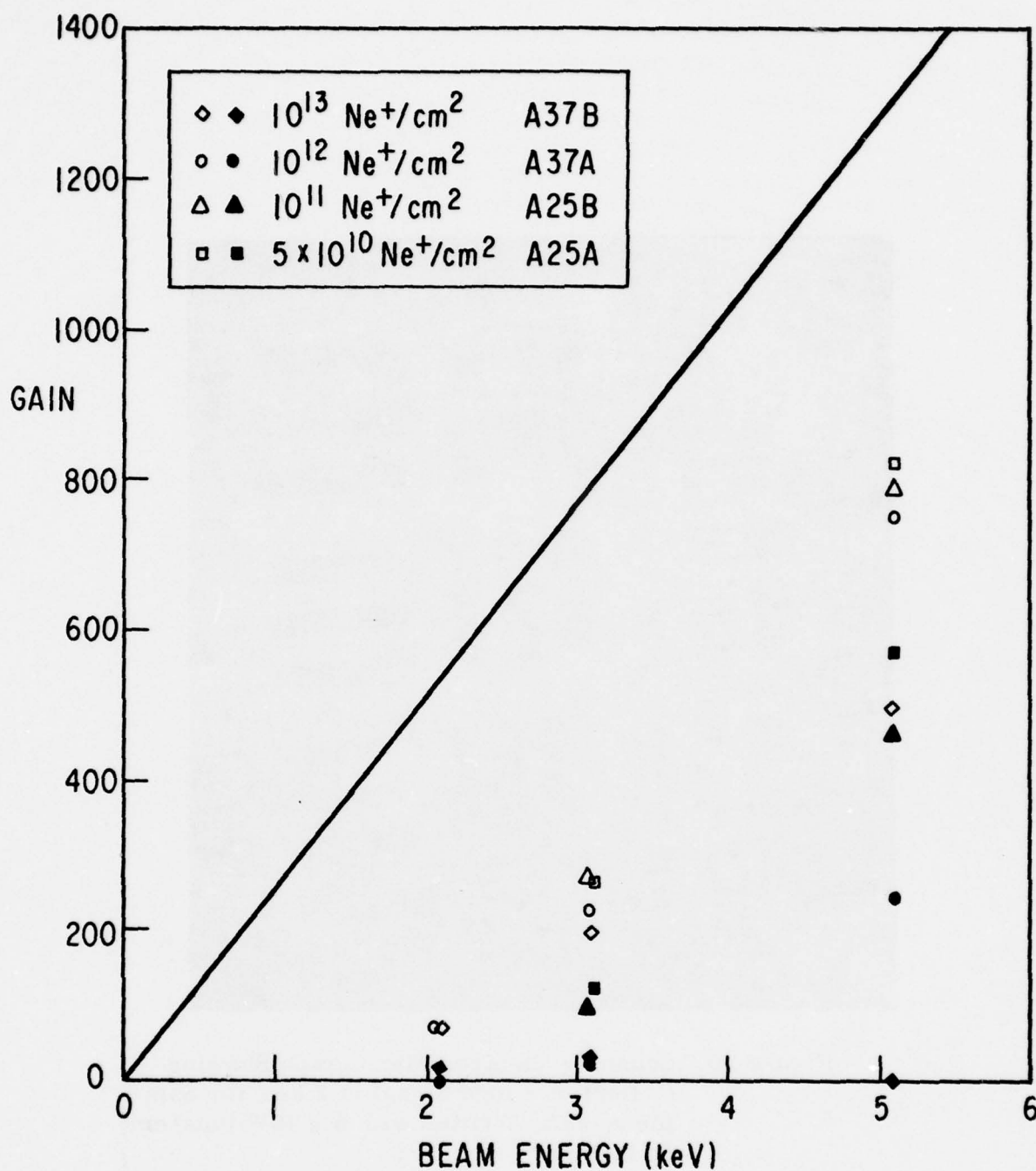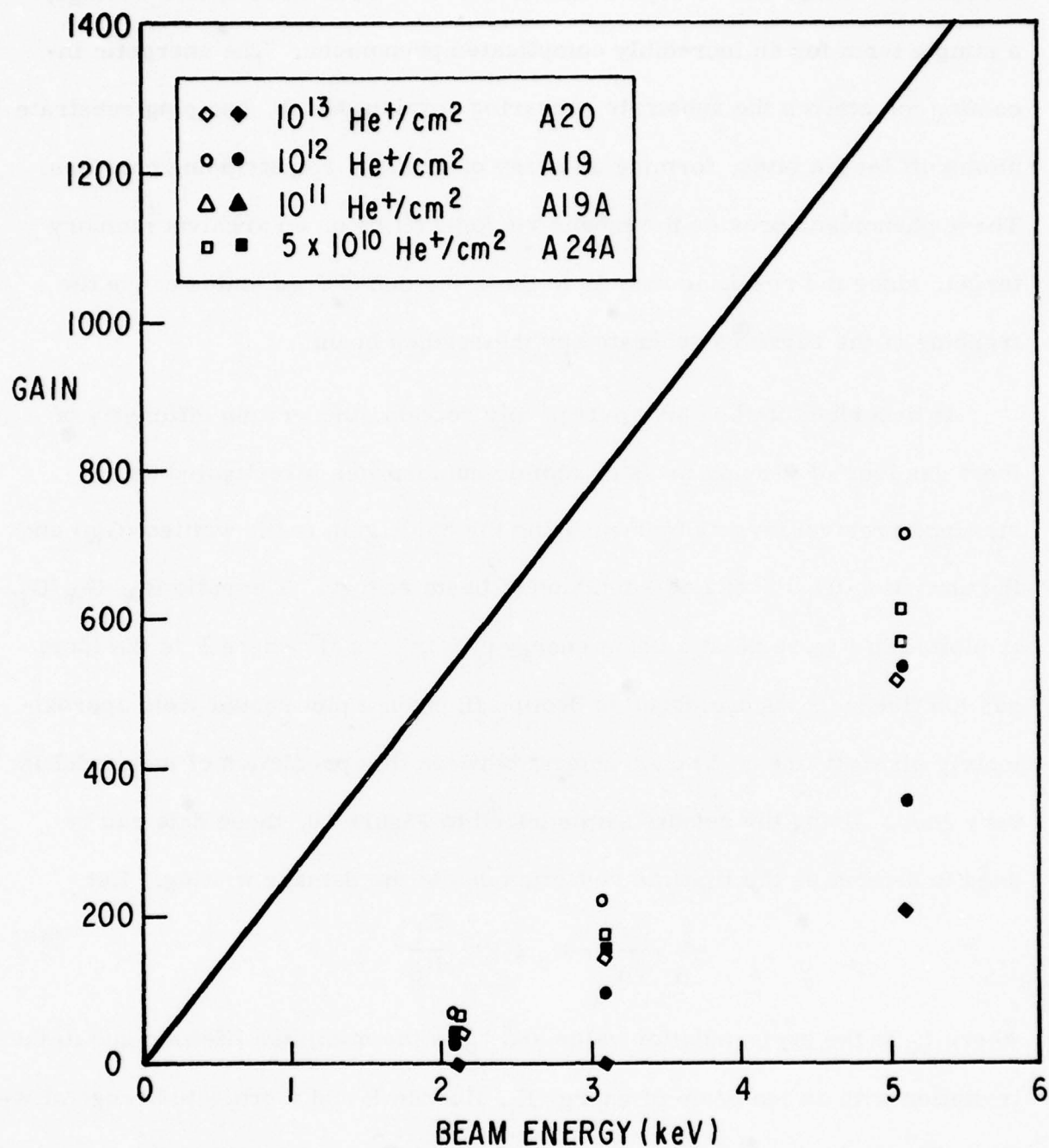
BEAM ENERGY (keV)

Figure 27. Gain vs Electron Beam Energy Measurements for Written and Un-
written Areas. [Formed by implantation of 30 keV He+ into sur-
faces of planar diodes formed by 100 keV As+ implantation in
10-20 ohm-cm p-<111> silicon, annealed at 770 °C 1 hour in argon
ambient. (Solid points indicate written areas; open points indicate
unwritten areas.)]

between incoming ion and crystalline substrate results in radiation damage, a simple term for an incredibly complicated phenomena. The energetic incoming ion strikes the substrate, shearing covalent bonds, bumping substrate atoms off lattice sites, forming an array of defects, and stripping carriers. These phenomena provide the means for ion writing on an archival memory target, since the resulting defects in their various charge states cause the trapping of the carriers generated by the reading beam.

As described in the early part of this section, the writing efficiency of inert gas ions of varying mass or atomic number was investigated using standard archival targets by measuring the diode gain in the written (G_W) and the unwritten (G_U) areas as a function of beam energy. The ratio $R_W = G_W/G_U$ is plotted in Figure 28 at a beam energy of 3 keV vs $\sqrt{F}$ where F is the inert gas ion fluence. As discussed in Section II, such a plot should yield approximately straight lines. The agreement between this prediction of the model is very good. Using the results summarized in Figure 10, these data can be used to determine the lifetime reduction due to the damage writing. Let

$$\frac{1}{\tau_o} + \frac{1}{\tau_p} = K_o \text{ x } F \text{ x } \frac{E_I}{R_p} \tag{4}$$

where τ_o is the preirradiation value and τ_p is the minimum lifetime due to the irritation with an ion beam of energy E_I, fluence F and a projected range of R_P. Normally, $\tau_o > \tau$ and τ_o is ignored. This is a very simple approximation which assumes that the ion beam produces uniform damage or lifetime reduction in a region from the surface to the peak ion penetration depth R_p. In the earlier calculation on which Figure 10 is based, the ion damage profile was assumed

50
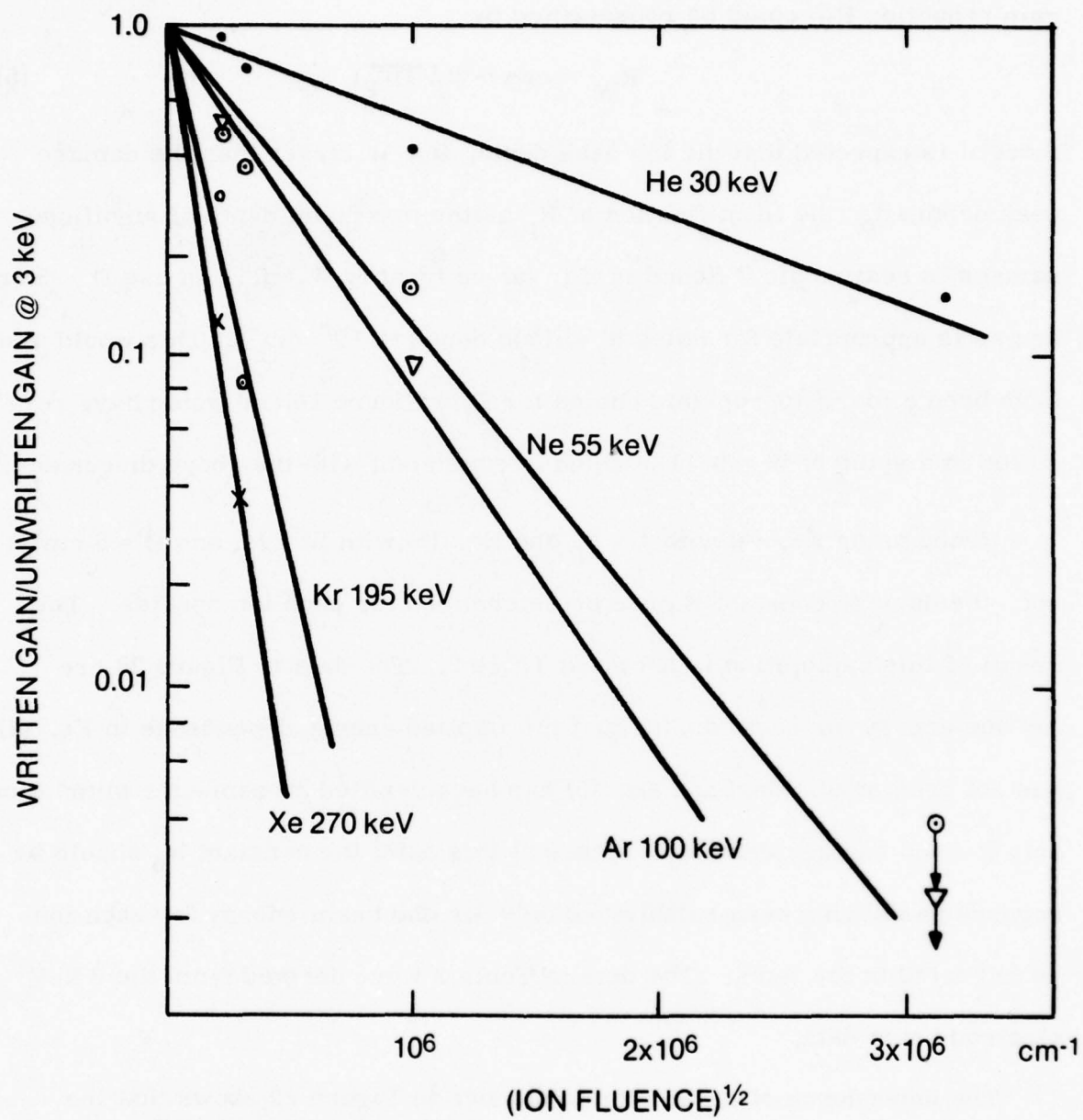
Figure 28. Written/Unwritten Gain vs Inert Ion Fluence

51

to be Gaussian, and the peak damage was placed at 0.08 μ below the surface. This calculation showed that to a very good approximation, the normalized gain reduction R_W could be represented by:

$$R_W = \exp(-W/\sqrt{D\tau_p}) \qquad (5)$$

Since it is expected that the ion peak depth, R_p, is larger than the damage peak depth, d_p, the identification of R_p as the maximum depth of significant damage is reasonable. Hence in Eq. (5) we identify $W = R_p$ and use $D = 5$ cm^2/ sec as is appropriate for holes in silicon doped to 10^{17} cm^{-3}. This would also have been a more appropriate choice for D in Figure 10 and would have resulted in a value of $W = 0.11$ μ which is consistent with the above discussion.

Hence using Eq. (4) with $\tau = \tau_p$ and Eq. (5) with $W = R_p$ and $D = 5$ cm^2/ sec, the damage constant K_O can be determined for each ion species. The result of this calculation is shown in Table 2. The data in Figure 28 are for one energy for each ion, so that the implied energy dependence in Eq. (4) has not been established and Eq. (5) has been verified by computer simulation only for one damage depth d_p. Hence at this point the constant K_O should be regarded as having been established only for one beam energy for each ion as indicated in the table. The data in Table 2 were derived from the 3 keV electron beam data.

The dependence of K_O on atomic number in Figure 29 shows that the increased writing efficiency noted for the heavier ions cannot be attributed simply to their higher energy loss rate in the material, since this effect is removed by the definition of K_O. Hence higher Z ions are essentially more damaging to silicon. This is not surprising since the heavier ions lost more

52

TABLE 2

CALCULATED DAMAGE CONSTANT K_O

Ion	Z	E_I (keV)	R_p (μ)	K_O $\left(\dfrac{cm^3}{sec\ keV}\right)$
X_e	54	270	0.1	2.0×10^{-7}
K_r	36	195	0.1	1.3×10^{-7}
A_r	18	100	0.1	0.33×10^{-7}
N_e	10	55	0.1	0.38×10^{-7}
H_e	2	30	0.2	3.6×10^{-9}

energy through nuclear collision and, in addition, the heavier ions produce higher energy silicon secondaries and tighter clusters of damage with more complex defects. These defect clusters might be expected to contribute significantly to lifetime reduction in the material, especially if these defect clusters produce collecting or depletion fields due to carrier compensation associated with the defects.

These data on writing efficiency will be used during the fourth quarter in designing high density writing experiments. The concept of K_O will permit scaling of the writing data to other ion beam energies.
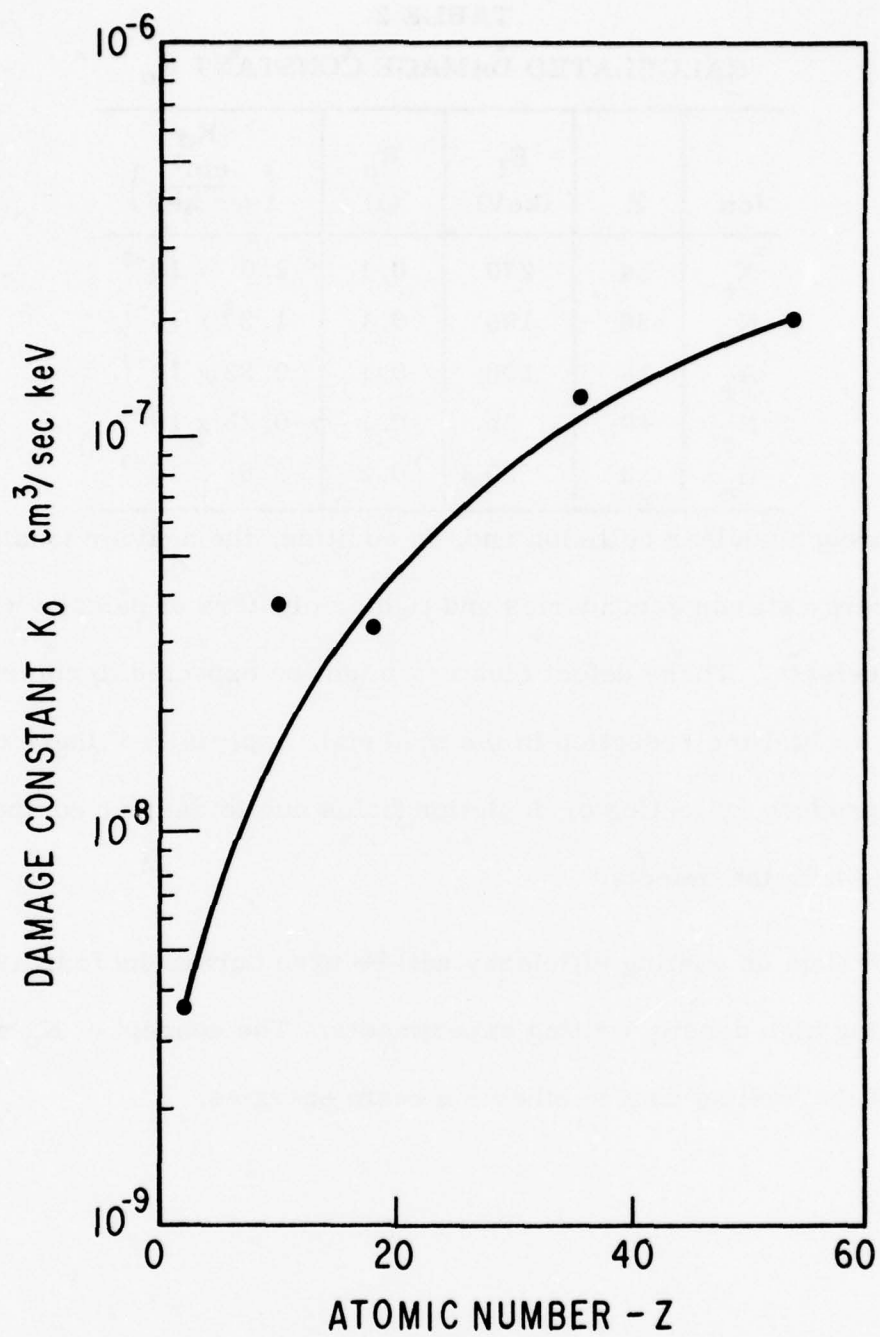
Figure 29. Damage Constant (K_O) vs Atomic Number (Z)

Section V

ALLOY JUNCTION EXPERIMENTS

THE ALLOY DIODE

There are two distinct mechanisms by which the "alloy diode" can invade the collection region of the substrate and so reduce collection efficiency:

- The first method depends upon a metal semiconductor alloy in which there is a substantial fraction ($\gtrsim 10\%$) of semiconductor contained at the eutectic temperature. This has the advantage that the eutectic temperature need only be <u>reached</u> (not exceeded) to create a physical intrusion of eutectic alloy into the collection region. Most of the candidates for this approach have large solid solubilities of the semiconductor in the metal slightly below the eutectic temperature creating a potential problem with thermal bias. These possible degradation effects are presently being investigated experimentally.

- The second method depends upon the creation of a heavily doped surface layer which would provide an electric field to oppose that of the collection region. In this case, the extent of the invasion of the collection region is determined by the collection diode doping level and, to a lesser extent, by the thickness and doping density of the surface regrowth layer. The existence of a "regrowth" layer requires that the eutectic temperature be exceeded by an amount sufficient to dissolve 10 Å or more of semiconductor in addition to that required for the eutectic concentration. The most important advantage of this method is that it permits the use of a large number of

55

metal semiconductor combinations and allows the choice of nearly any temperature range. In many cases, it would be necessary to dope the metal with a few percent of the dopant desired for the semiconductor regrowth layer. The most important consideration for the success of this approach is that the metal dissolve a useful quantity of semiconductor ($\gtrsim 10$ Å) at a temperature not too far above the eutectic. Unfortunately, some otherwise useful alloys such as Ge-In and Ge-Ga take up very little germanium until considerably higher temperatures. The Ge-Sn combination at T = 232°C may be superior in this respect.

The use of a low temperature alloy process has two major advantages:

1. Little or no thermal bias would be needed.
2. The temperature would be low enough to permit immediate reading of the diodes for verification.

A possible disadvantage is the fact that the wafers would be more sensitive to accidental temperature increases. The written memory could however be made more durable after writing by simply etching off the metal. We believe that the great advantage of being able to read while writing at the same station with the same electron optics, and even the same beam with reduced current, could be so valuable to the overall system design as to outweigh this disadvantage.

COMPUTER MODELING

As an aid to understanding the factors involved in the alloy diode approach and to help design and interpret the electron beam writing experiments, two

computer programs are being used. Both are quite detailed and specialized and are expected to provide reliable quantitative information. They have already had some influence on our thinking as will be described below.

The purpose of the first computer program is to study the effect of a thin, heavily doped surface layer on the potential and electric fields in the collection region. In this way it should be possible to determine the ideal collection diode doping profile. If the collection diode surface is too heavily doped, even a very heavily doped surface layer would have little effect on the collection probability.

An existing computer program [6] was modified to accomplish this end. The program provides a numerical solution to the one-dimensional Poisson equation near the surface in a semiconductor.

$$\frac{d^2\phi}{dx^2} = \frac{\rho(x, o)}{\varepsilon\varepsilon_o} \tag{6}$$

where ϕ is the potential, X is the distance from the semiconductor surface and $\rho(x, \phi)$ is the charge density. The simplifying assumptions made are:

1. Parabolic bands with one density-of-states effective mass for electrons and another for holes

2. Band structure and impurity energy independent of doping density

3. Quasi-equilibrium: all occupation probabilities related to a single Fermi energy

Fermi-Dirac statistics are used throughout and any impurity profile may be used. The outputs of the program are:

1. Potential vs distance

57

2. Field vs distance

3. Electron and hole concentrations vs distance

4. The above for different surface potentials and fields

5. MIS (Metal Insulator Semiconductor) C(V) curves for the system (with insulating film) in both depletion and inversion modes

6. The expected result of a deep depletion profiling measurement [7]

7. Surface channel carrier concentration

The program was originally designed for ion implantation studies and has built-in provision for background doping plus Gaussian implant profiles with adjustable ionization energies (one donor and one acceptor). An additional donor and acceptor with separately adjustable energies and arbitrary profiles are readily included.

In the present application, the collection diode has been modeled with $10^{15}/cm^3$ boron background doping and a Gaussian arsenic implant of $10^{14}/cm^2$ fluence centered 402 Å _outside_ of the silicon. This corresponds approximately to a 100 keV implant through 800 Å of SiO_2 (using LSS theory)[8]. The semi-conductor surface band diagram (potential vs distance from the surface) is shown in Figure 30. On the same figure is shown the effect of the addition of a very thin, heavily doped, alloy regrowth surface layer consisting of $2 \times 10^{12}/cm^2$ acceptors. The surface layer has substantially reduced the collection field everywhere and has reversed it (created a "dead" layer) within 300 Å of the surface. An increase in the alloy regrowth doping density or decrease in the implantation fluence could greatly increase the width of this "dead" layer.
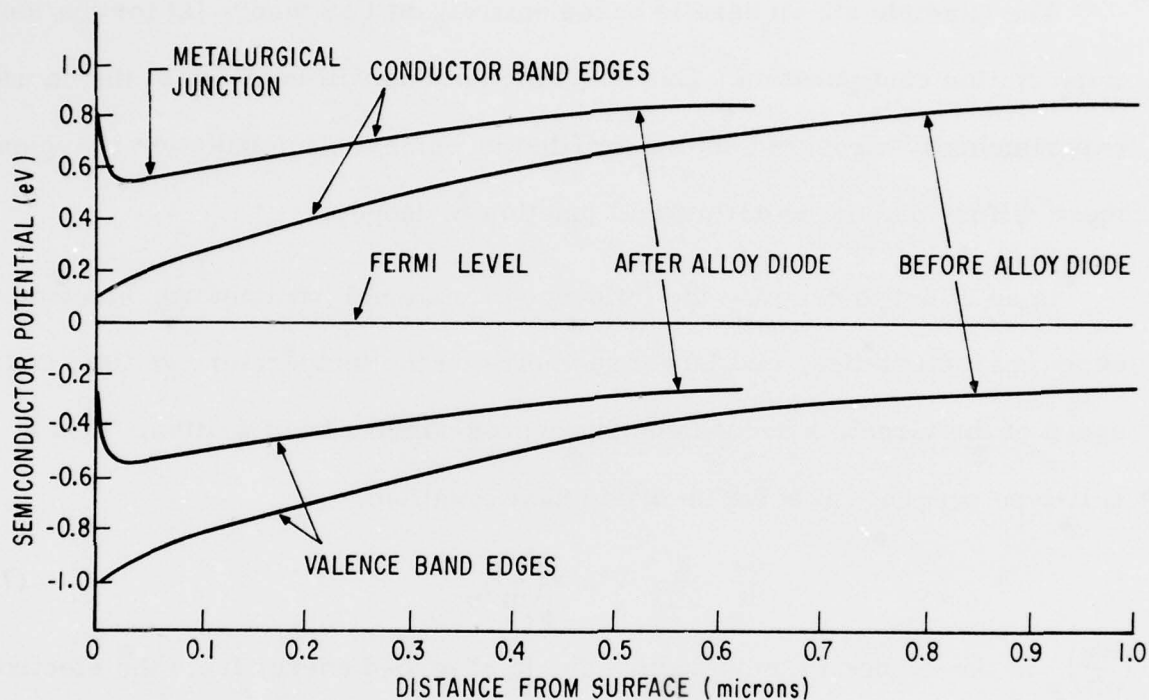
Figure 30. Surface-Adjacent Silicon Band Edge Energies Plotted vs Distance
from the Surface. (The shift due to a surface alloy regrowth con-
taining $2 \times 10^{12}/cm^2$ donors is shown. In this diagram, no bias is
applied to the collection diode whose metallurgical junction is only
500 Å from the surface.)

59

Figure 31 shows the electric field for the same configuration with and without the regrowth layer. Note that in both Figure 30 and Figure 31, the collection diode is shown unbiased. The metallurgical junction is only 500 Å from the surface.

The example shown here is based entirely on LSS theory [8] for the ion implantation configuration. Our next calculations will conform to the correct, experimentally measured doping profiles in which the implantation is typically more diffuse and the metallurgical junction is deeper.

In an effort to examine the influence of material parameters, electron beam characteristics, and target geometry on the temperature vs time and space of the target, a second computer program has been written. It is a cell-type program to solve the basic heat equation:

$$\frac{du}{dt} = \frac{K}{cD} \, V^2 u + \left(\frac{du}{dt}\right)_p \tag{7}$$

$\left(\frac{du}{dt}\right)_p$ is the change in temperature due to absorbed energy from the electron beam. Here u is the temperature, t = time, K = thermal conductivity, c = specific heat, D = density. The quantity cD is the volume specific heat which is about 1.65 J/cm^3 °C for most materials. The quantity K/cD is the thermal diffusivity. Because of the radial symmetry of the present problem, Eq. (7) was reduced to two dimensions by transforming to cylindrical coordinates in which it becomes:

$$\frac{du}{dt} = \frac{K}{cD} \left[\frac{1}{r} \frac{d}{dr} \left(r \frac{du}{dr}\right) + \left(\frac{d^2 u}{dZ^2}\right) \right] + \left(\frac{du}{dt}\right)_p \tag{8}$$

The coordinate Z is the depth into the target and r is the horizontal distance from the vertical electron beam axis.

60
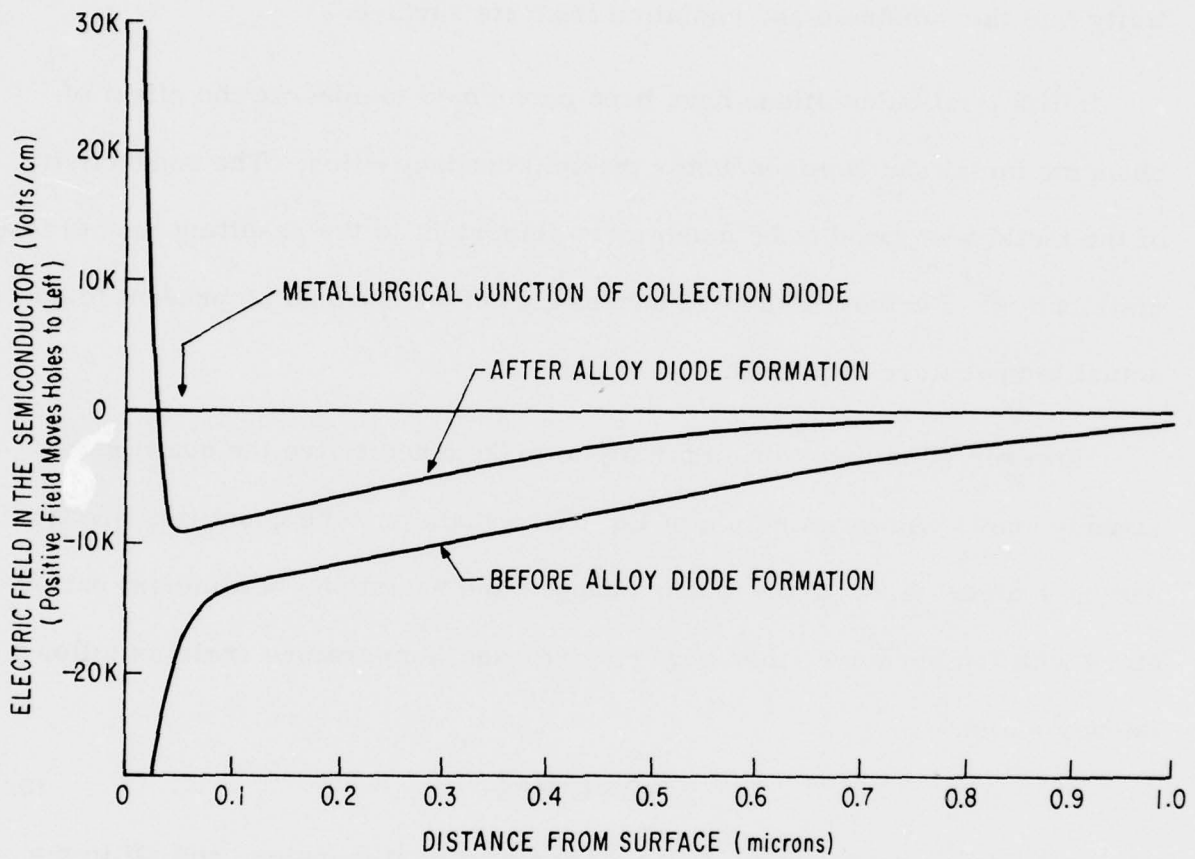
Figure 31.   This Is the Same Case as Figure 30, Except that It Is the Electric Field ($-\nabla\phi$) Which Is Plotted

The program permits the use of different materials with different (and temperature-dependent) parameters. It also permits phase changes during heating with associated latent heats. Heat input is generated with an arbitrary (but radially symmetrical) powder density input pattern and is lost by conductivity into the substrate and radiation from its surface.

Initial trial calculations have been performed to observe the effect of changing metal and semiconductor thermal conductivities. The conductivity of the metal was found to be much more important to the resulting temperature distribution. Further trials are necessary before it would be prudent to quote actual temperature increases.

However, this program is simply to make quantitative the qualities we already know. An examination of Eq. (7) reveals how the quantities involved can be scaled. If we ignore phase changes and variations of material parameters with temperature, then power, size, and temperature scale as follows (steady state):

$$\Delta U \sim K\, P/X \tag{9}$$

where P = total input power, X is a linear scaling dimension, and ΔU is the final temperature increase of any given position. So there are really only three parameters of any importance in achieving a large ΔU:

1. <u>Thermal conductivity.</u> Having a very low thermal conductivity serves a dual purpose. It allows a large temperature increase, and equally important, provides adjacent bit thermal isolation. The increased ΔU does little good if nearly bit sites are overheated.

62

a. Metal film. In addition to choosing metals with low K, the effect of the K can be greatly modified by deposition parameters. In experiments during this quarter, we observed a 5X reduction in electrical (and therefore thermal) conductivity in our sputtered 1000 Å aluminum films compared with evaporated films. We intend to devote further effort to exploit these surface topography effects. Also, the introduction of small amounts of selected impurities can greatly alter K without seriously affecting the alloy properties.

b. Semiconductor. The relatively (to silicon) low K of germanium has already been noted. We believe that this value is low enough to allow an adequate ΔU, but if further reduction proves to be necessary, it is possible to reduce K by more than 5X by using a Si-Ge alloy [9]. The associated reduction in carrier mobility would not be intolerable.

2. Power input. For a given dimension of device, the best way to increase power density input is to increase the density of the materials used so that they will have increased stopping power for the electron beam. This permits using a higher voltage beam to irradiate the same volume.

3. Device size.

a. Beam spot size: This is perhaps the most critical parameter of all. The Coates and Welter field emission write station should produce focused spots 1000 Å in diameter at 3 to 5 keV. Field

emission sources have the potential to be imaged to much smaller diameters.

b. Use of a heavy metal (e.g., indium, tin, etc.) will permit using a thinner metal film on the surface with resulting greater confinement of the beam power.

ALLOY JUNCTION - EUTECTIC WRITING EXPERIMENTS

During the first six months of this contract, alloy junction writing experiments were performed using a Q-switched Nd: YAG laser as the energy beam. The laser equipment (Electro Scientific Model 25 laser trimmer) is computer controlled for:

- x-y specimen position

- laser pulses per specimen position

- laser power delivered per pulse

The equipment, therefore, permits a multiplicity of operating conditions.

The experimental effort conducted during the first two quarters was aimed at demonstrating that alloyed bit sites could be formed with the beam energy of a laser. The memory substrate selected for the experiments was a silicon n-p planar diode coated with a thin aluminum layer. A description of the experiments and the results obtained are detailed in the first two quarterly reports. The following paragraphs summarize the important achievements during the first six months.

During the first quarter, it was shown that junction writing could be accomplished using multiple pulses of the laser beam. Single laser pulse

64

writing of typically 150 nsec duration was also demonstrated. Memory-type readout was successfully shown from laser irradiated areas before and after removal of the aluminum layer. A Cambridge Mark IIA stereoscan electron microscope was used to read out the alloyed bit sites. These experiments verified that writing could be achieved on a time scale compatible with a 10^7 bits/sec writing rate.

Average and peak power measurements were made for the laser beam over its full range of operation. Based on these measurements, it was estimated that power densities in the range of 10^7 to 10^8 W/cm^2 were used in the writing. Considerable surface damage of the aluminum layer was evident in written areas indicating that power well in excess of that required for eutectic alloying was used. Angle lap and stain measurements of the written areas further confirmed this by showing aluminum at depths of 5 to 6 μ below the Al/n-Si interface. Anticipated depths for eutectic alloying are expected to be approximately 1/3 to 1/2 of the thickness of the aluminum layer or approximately 300 to 500 Å.

Based on the achievements of the first quarter, experiments during the next three months were aimed at demonstrating eutectic alloying of the written regions, again using the laser system. Means for reducing the laser beam energy and at the same time maintaining stable operation became a problem. The power measurements made earlier showed considerable variation in the pulse amplitude, and hence the peak power from pulse to pulse. This power variation, coupled with the lack of data for the reflectance and thermal properties of the sputtered aluminum layer, made calculations of the target

65

temperature rise as a function of laser operating point virtually impossible. In view of these difficulties in predicting the target temperature rise as a function of laser energy, the laser system was set at its most stable operating point and the beam energy reduced in controlled steps with Schott glass neutral density filters. At each filter valve, a 10 x 10 array of spots on 20 μ centers with 10 pulses per spot was exposed. The range of filter produced laser exposure variations from those showing visible surface damage to the aluminum layer to no visible surface damage. Memory readout was obtained at all of the filter settings. This implied that eutectic alloying had been achieved because the aluminum surface was not melted at the highest filter setting, yet a laser affected area was observed with target readout. This was further confirmed by target gain vs read beam landing energy measurements. These measurements were found in agreement with the target model and indicated writing depths on the order of 500 Å as expected for eutectic alloying.

The eutectic alloying experiments during the second quarter were accomplished with 10 pulses per spot. The third quarter laser writing experiments were aimed at demonstrating eutectic alloying with a single laser pulse per spot. This was accomplished with the Al-Si target previously used. Laser writing was also demonstrated this quarter using a Au-Si target as previously proposed in the First Quarterly Report. The third quarter experiments and the results of these experiments are described in this section of the report.

LASER WRITING EXPERIMENTS

The laser writing experiments were conducted again this quarter using the Model 25 Electro Scientific Industries laser trimmer, which is described in detail in Section VI of the First Quarterly Report. Readout and analyses of the written areas were done on the Cambridge scanning electron microscope. The operating parameters for the laser were the same as those used in the second quarter eutectic writing experiments, since they produced the most stable beam. The lamp drive current was 22 A, Q-switch rep. rate 2 kHz, 60 mil aperture and 10% beam splitter. A photograph of the laser output pulse for these conditions is shown in Figure 32. The laser was programmed to produce rows of single pulses per spot. A typical full width at half maximum pulse width of 150 nsec is achieved at this operating point.

The first experiments were conducted on an Al-Si target. The substrate was a planar n on p silicon diode. Resistivities of the n and p layers were 1 ohm-cm and 400 ohm-cm respectively. The n layer thickness was 2.8 μ. The top surface of the n layer was plasma etched and sputter coated with 1000 Å of aluminum to remove and prevent regrowth of the native oxide layer. A cross section of the target is shown in Figure 33.

With the aforementioned operating conditions for the laser, rows of single pulse per spot laser writing was done at the neutral density (ND) filter valves shown in Figure 34. Laser writing was started using a 0.1 ND filter and increased in steps ending with a 0.7 ND filter. The last visible writing as viewed on the laser video monitor occurred with a 0.6 ND filter. One further

67
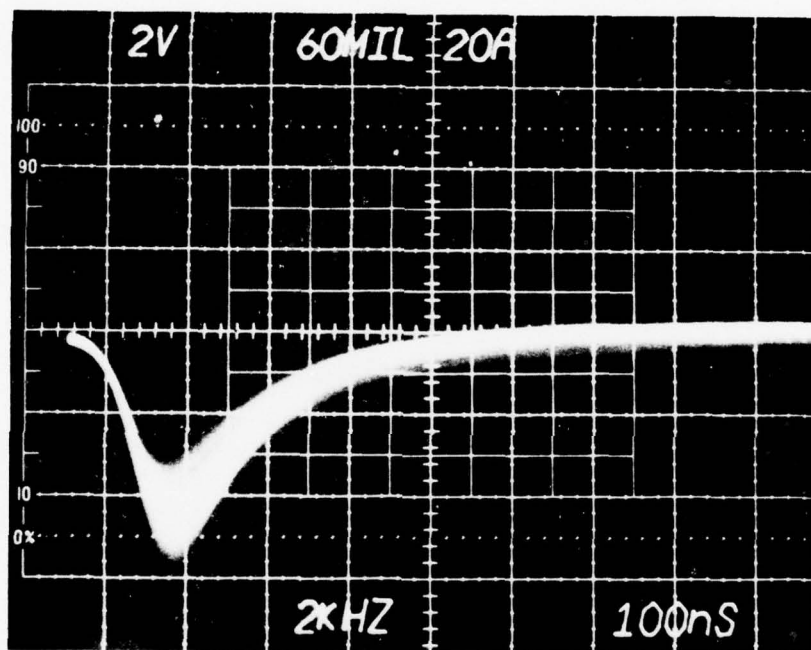
Figure 32.   Laser Output Pulse

1000 Å

2.8μ

SPUTTERED
Al. LAYER

N-TYPE Si

p SUBSTRATE
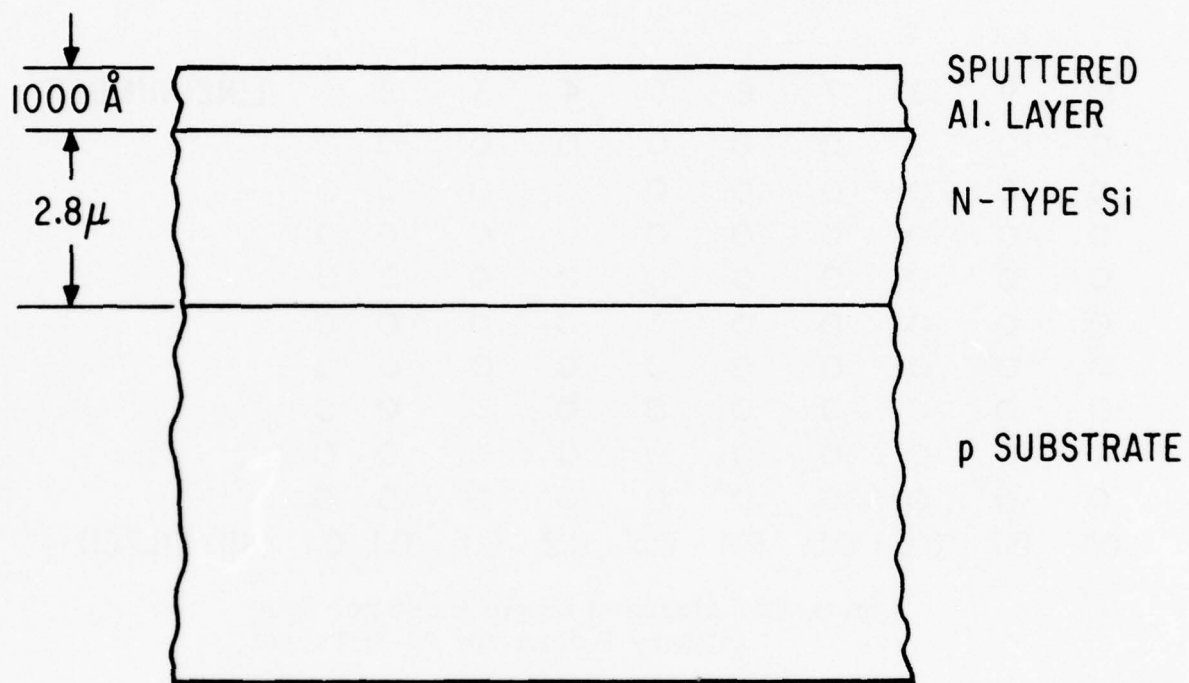
Figure 33. Target Cross Section

Figure 34. Sketch of Single Pulse per Spot
Laser Pattern for Al-Si Target

step was recorded using a 0. 7 ND filter followed by a line of spots using a 0. 1 ND filter.

The target, with metal layer intact, was read out using the Cambridge scanning electron microscope. The planar diode signal was used to z modulate the SEM display. As shown in the photograph in Figure 35, memory readout was obtained at *all of the laser energies employed*. Even though this is the most stable operating point for the laser, there is still considerable power variability as can be seen from the planar diode signals at various filter factors. Target gain was measured at 10 kV beam energy for a representative spot for the neutral density filter valves. These data are plotted on the curves for gain vs beam energy calculated with a one-dimensional target model as shown in Figure 36. This model is described in Section II of the Second Quarterly Report and was used in Section V of that report for the analysis of alloy writing depths. As noted in Section V of that report, there is an excellent fit between the model and experimental curves for beam energies greater than 7 kV. Using the gain vs beam energy curves for the model, the gain vs dead *layer thickness curve at 10 kV shown* in Figure 37 was developed. The measured gains at 10 kV for the laser written spots were used in conjunction with Figure 37 to estimate the dead layer thickness, T_D, for each written area and the aluminum layer itself. The writing depth, W_D, was estimated by subtracting the dead layer thickness for the aluminum layer from the dead layer for the written area. The data for the written areas are summarized in Table 3.

71

Figure 35.   Planar Diode Readout
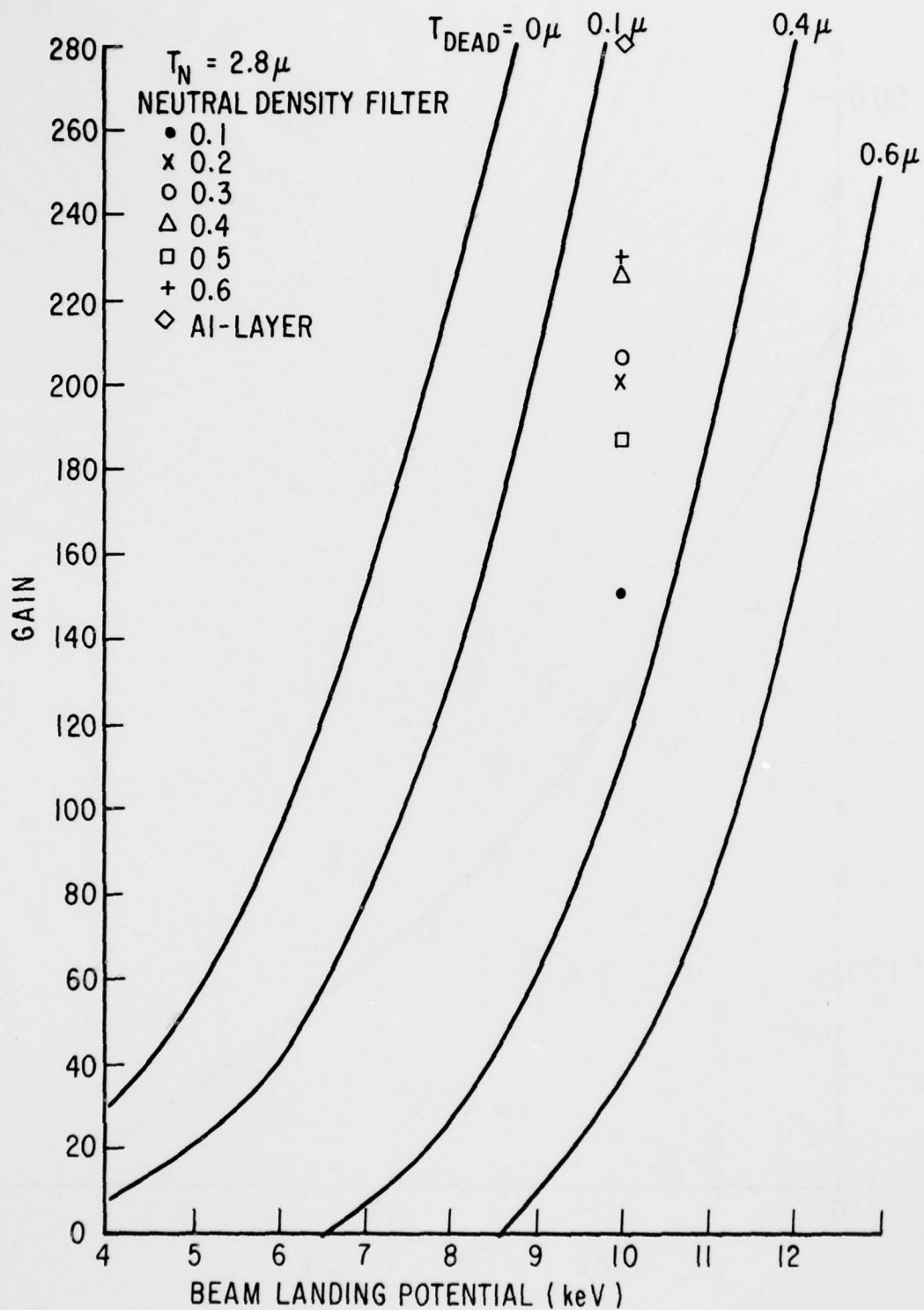
Figure 36.   Target Gain vs Beam Landing Potential
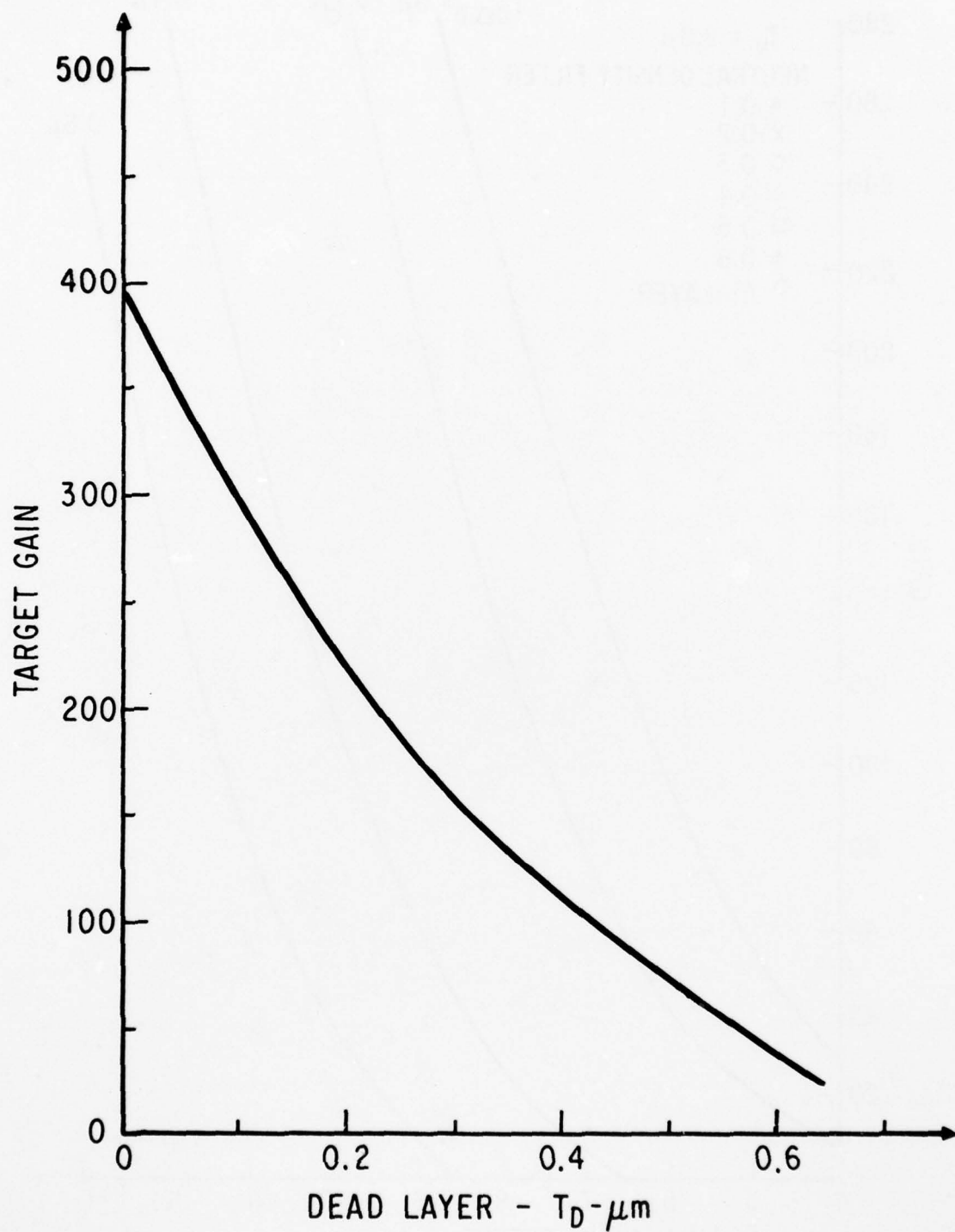
Figure 37. Target Gain vs Dead Layer Thickness
Based on the One-Dimensional Model

TABLE 3

WRITING DEPTHS FOR SINGLE PULSE LASER WRITTEN
SPOTS BASED ON THE ONE-DIMENSIONAL TARGET MODEL

Gain at 10 kV	T_D (μ)	W_D (μ)	Target Area
280	0.12	0	Al-layer
151	0.26	0.14	0.1 ND filter
201	0.23	0.11	0.2 ND filter
206	0.22	0.10	0.3 ND filter
226	0.19	0.07	0.4 ND filter
187	0.245	0.125	0.5 ND filter
229	0.185	0.065	0.6 ND filter

The writing depth at a neutral density filter of 0.5 seems to be erroneously deep. This could be due to the variability in laser power or experimental error in the gain measurement. These targets will be reevaluated during the next reporting period. The new Coates and Welter write station is being equipped with a specially designed target holder and will be used for these tests. The target stage is described in Section VI of this report.

The single pulse per spot writing depths are compared with 10 pulse per spot writing depths from the last quarter in Table 4. For the more deeply written spots, the writing depth achieved with a single laser pulse per spot seems to be approximately half that of the writing depth achieved with 10 pulses per spot. However, these data must be more thoroughly checked and analyzed with percent modulation measurements before any conclusions can be reached. Several possible explanations exist:

- Multipulse writing driving the dead layer deeper
- Reflectivity changes of aluminum surface from pulse to pulse

TABLE 4

COMPARISON OF WRITING DEPTH W_D FOR SINGLE PULSE PER SPOT AND 10 PULSE PER SPOT LASER WRITING

ND Filter	W_D (μ) 1 pulse/spot	W_D (μ) 10 pulses/spot
0.1	0.14	0.24
0.2	0.11	0.21
0.3	0.10	0.22
0.4	0.07	0.14
0.5	0.125	0.08
0.6	0.065	0.05

- High thermal conductivity effects on multipulse mode

- Laser power variations from pulse to pulse

As can be seen from the experimental results, a more thorough investigation of the single pulse per spot writing and the multipulse per spot writing must be made. This is planned for the next quarter and will be done with the new Coates and Welter field emission write station. However, laser writing with a single pulse per spot with no visible surface damage to the aluminum layer was achieved. This, in conjunction with the writing depths at the lower laser beam energies, indicates that the main goal of this quarter (i. e., eutectic alloying with single pulse per spot) was achieved.

In addition to the single pulse per spot writing on the Al-Si target just described, laser writing experiments were conducted on a Au-Si target. It was pointed out in Section VI of the First Quarterly Report, that other metal semiconductor systems such as Au-Ge, or Au-Si might be useful for alloy targets based on solubility considerations at the eutectic point. The writing

and readout method for these systems would depend on preventing electron hole pair generation in the written region because the area is actually a metal or metal with semiconductor crystallites imbedded.

In order to test this concept, a Au-Si target was made in the same manner as the Al-Si target except that the metal layer was 1000 Å of sputtered gold. The laser operating conditions were the same as those used for the Si-Al target. Again single pulse per spot exposures were made. Fifty lines were exposed at a neutral density filter value of 0.1 and then single lines covering the neutral density filter range from 0.1 to 0.4 as shown in Figure 38 were exposed. At the highest filter factor of 0.4, writing was no longer visible on the laser television monitor. Planar diode readout was observed using the Cambridge scanning electron microscope (Figure 39). No further tests were made on this target. However, it can be concluded that memory-type readout can be achieved with metal-semiconductor systems other than the conventional semiconductor dopant metals such as the Column III metals.

During the next reporting period, laser written targets will be evaluated as described. In addition, electron beam formed bit sites will be written using the Coates and Welter field emission column. Initially, silicon substrates will be used, followed by germanium targets.
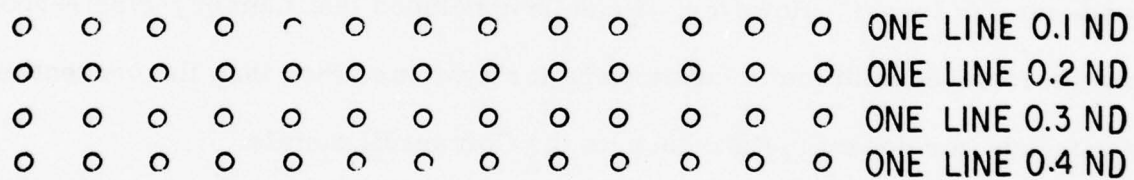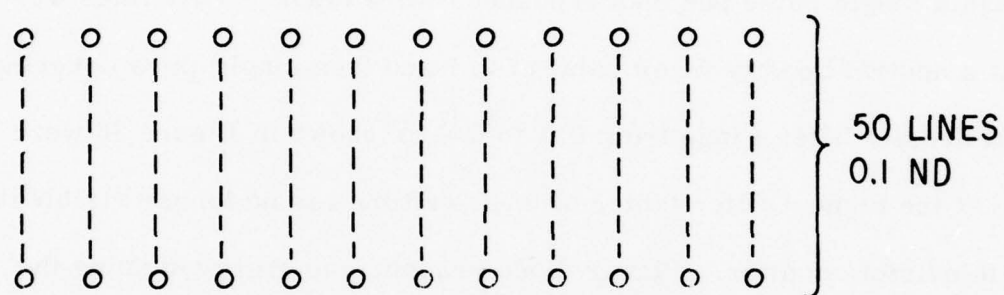
Figure 38.   Sketch of Single Pulse per Spot Laser Pattern for Au-Si Target
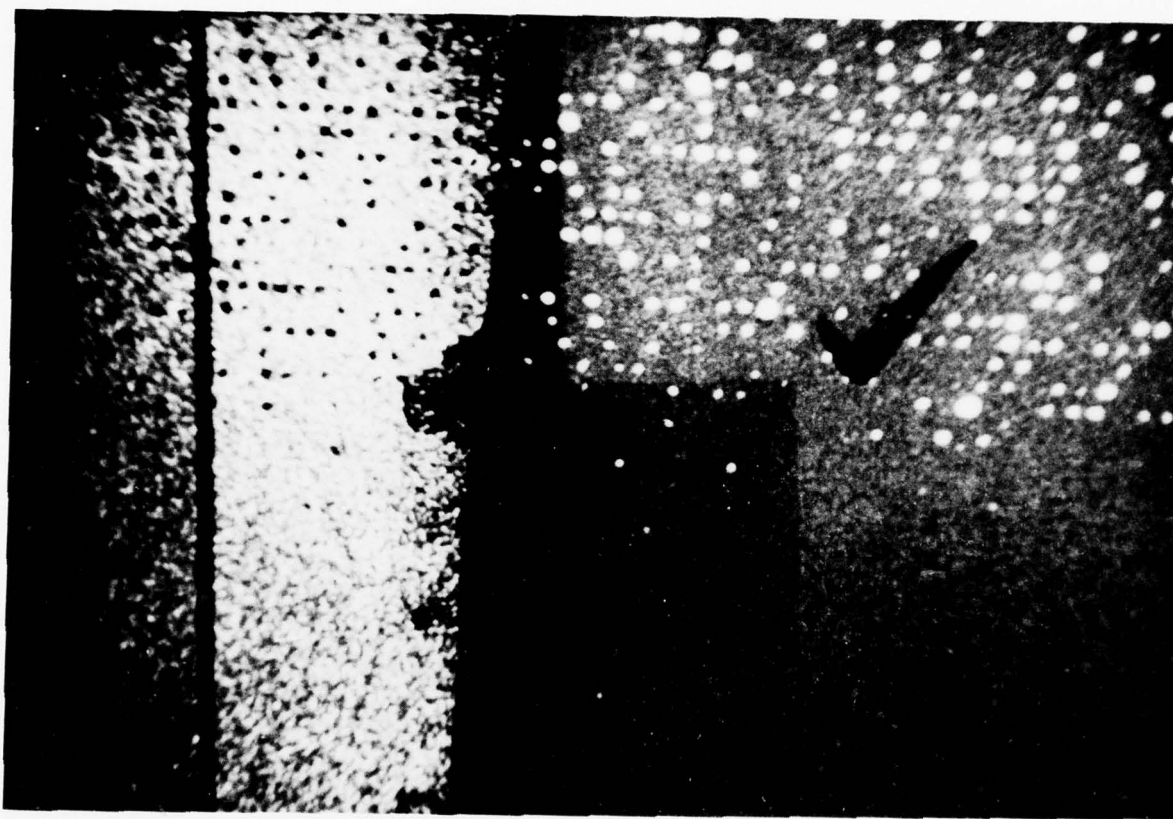
Figure 39.   Planar Diode Readout Single Pulse per Spot Laser Pattern

SECTION VI

ALLOY JUNCTION EXPERIMENTAL WRITE STATION

INTRODUCTION

The alloy junction storage concept consists of the use of a finely focused electron beam to locally heat a substrate to form an alloy between a thin surface layer metal and a semiconductor. Several interrelated experimental studies are planned to determine the applicability of this approach as a viable memory. As a first step, a laser was used as the energy beam. The laser-formed bit sites proved that single pulse, localized beam heating could alloy suitable materials at the eutectic temperature. This does not necessarily prove that electron sources can deliver enough energy in the time frame to form an alloy. Experimental verification of an electron beam's capability is deemed necessary.

Very early in this phase of the contract, a field emission electron beam write station was specified and contracting officer approval granted for its purchase. An order was placed June 1976 with the Coates and Welter Instrument Corporation for the column and associated drive electronics and power supplies. A 120-day delivery promise was received.

Specification of the electron beam requirements for forming alloy junctions is an integral part of the Phase I study. Therefore, the analysis to determine the optimum configuration for an electron beam column had not been undertaken at the time it was necessary to place an order. The approach chosen for specifying the column was to describe the beam requirements in

81

terms of beam current and spot size to meet theoretical estimates of beam energy necessary to effect the alloy. The method of selection and specification of the column is described in detail in the First Quarterly Report. The basic specifications for the column are:

I_b = beam current $\geq$ 150 nA

d_s = 1000 $\mathring{A}$ = spot size

V_l = landing potential = 3 kV $\leq V_l \leq$ 5 kV

This equipment was delivered during the third quarter of the contract period and made operable. Modifications to the equipment for alloy junction writing experiments have been started and many are complete. This section of the report describes the write station, its performance to date, and the status of modifications for alloy junction experiments.

ELECTRON BEAM WRITE STATION

The Coates and Welter Instrument Corporation modified the electron optics of a Model 104A scanning electron microscope to meet the spot size and beam current requirements at low beam landing energies required for alloy junction writing. A photograph of the equipment is shown in Figure 40 and a column schematic diagram is given in Figure 41. The column has a field emission electron source housed in an ultra high vacuum region that is both internally and externally pumped to a pressure of 10^{-10} to 10^{-9} Torr. The gun chamber is differentially pumped through a conductance limited aperture so that the main column pressure can be approximately 1000 times greater than the gun chamber. The gun chamber can be closed off with an isolation valve to allow rapid changing of target samples. The first lens is a specially

82
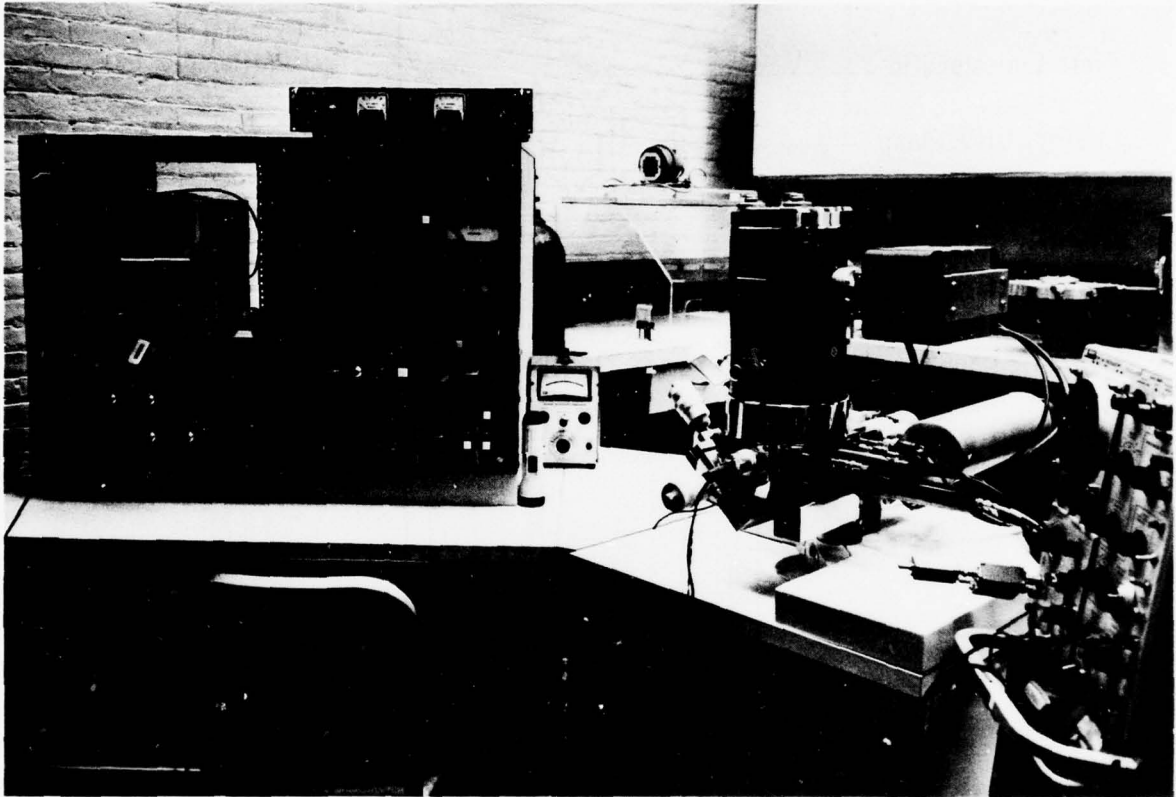
Figure 40. Electron Beam Write Station
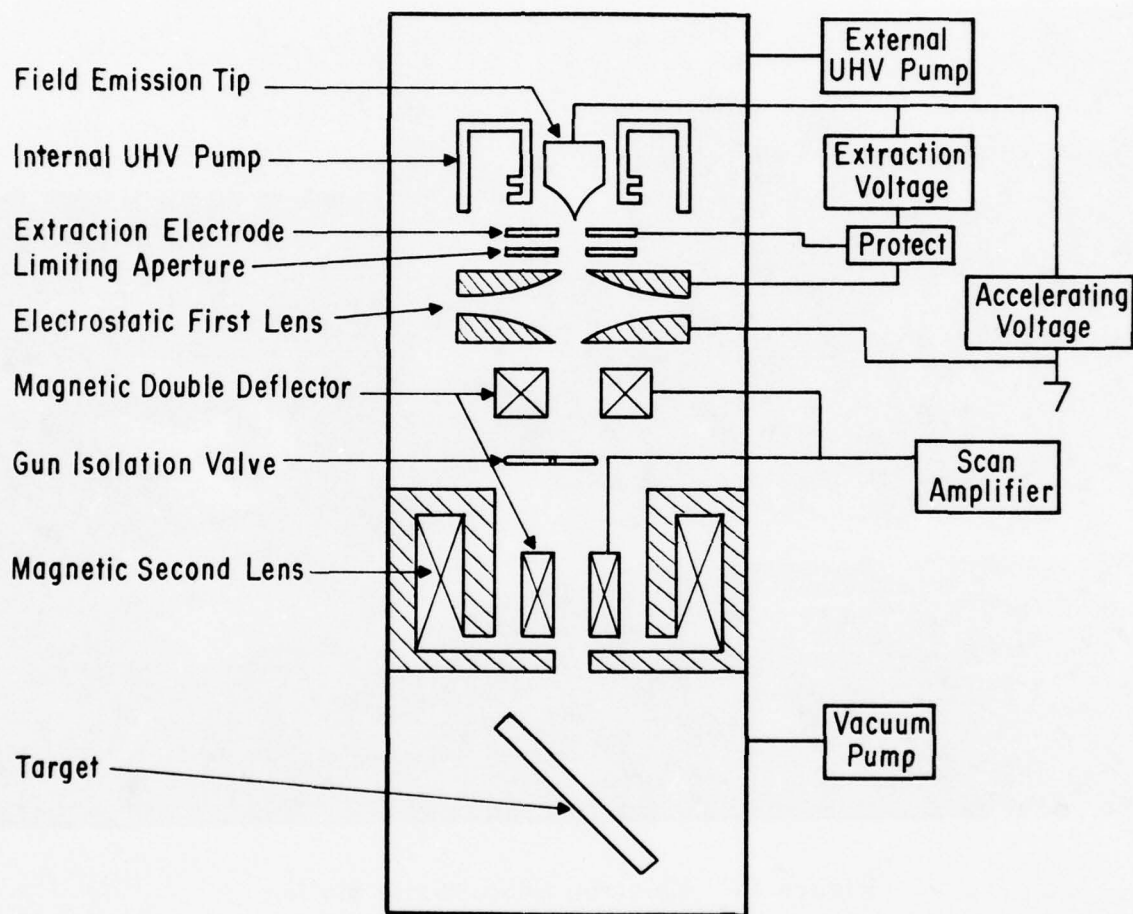
Figure 41. Schematic Diagram of an Electron Beam Write Station

designed low aberration electrostatic lens, and the final lens is a high quality low aberration magnetic lens. As delivered, the target plane accepts a standard Coates and Welter specimen stub which is normally sloped at 45°. External mechanical controls allow x, y translations of 0.8 in. and tilt from 0° to 100° and 360° rotation for the target sample. Beam scanning electronics operate at normal television rates.

Several modifications were made to the column by the manufacturer which were required to achieve the alloy junction writing requirements. The field emission source was designed to be capable of operating in the temperature aided field mode as well as room temperature field mode. An enlarged beam limiting aperture was installed to meet the high beam current requirements. Both of these modifications sacrifice normal resolution through increased chromatic and spherical aberrations. However, the spot size specified was achieved. Beam blanking was added and consists of deflecting the beam off an aperture by electrostatic deflection requiring standard T^2IL (0, +5 V logic levels) to deflect the beam. The blanking drive electronics were not supplied by Coates and Welter; however, external pin connections were provided. External scan input is also provided to the deflection amplifiers and requires a ±2 V signal above ground. This is required in order to provide the proper scanning drive for alloy junction writing experiments. The normal secondary electron collection package (i.e., scintillator, light pipe, photomultiplier, and the photomonitor) was not purchased since it is not required for alloy junction experiments. The secondary electron collection package was generously provided by Coates and Welter on a temporary loan basis to aid in the initial setup of the equipment. The photomonitor package, however, was not supplied.

85

EQUIPMENT MODIFICATIONS FOR ALLOY JUNCTION EXPERIMENTS

The column modifications described in the preceding paragraphs were made by Coates and Welter Instrument Corporation to meet the beam current and spot size requirements for alloy junction writing experiments. Electronic blanking and deflection circuitry has been incorporated by General Electric. Along with these, several further adaptations and modifications must be made to the equipment to make it useful for alloy junction target work. These are:

- Slow scan deflection drive

- Vernier magnification control

- Sample stage for alloy junction target readout

- Heated target stage for alloy junction electron beam writing

All of these additions to the equipment's capabilities are in progress and are completed or nearing completion.

As previously mentioned, the Coates and Welter instrument operates at standard video rates. For alloy junction writing and reading experiments, slower and/or variable scanning rates are required depending on the field size and target frequency response. For this purpose, a slow scan electronics drive package has been assembled and is now in operation. This package uses a 5103N Tektronix oscilloscope with two type 5B10N Tektronix time base generators to produce variable raster scan control. The raster can be displayed on the oscilloscope with line and field blanking. The individual sweeps, with suitable attenuation, are also supplied to the external deflection amplifier inputs of the Coates and Welter instrument for control of the electron beam. A type 5A22N differential amplifier is also included in the oscilloscope package.

86

This unit can accept signals from either the target signal or at least tempo-
rarily from the secondary emission photomultiplier to z modulate the raster
displayed on the oscilloscope. This allows simultaneous viewing of the scanned
area in the column. External banking signals for the beam, which are
synchronized with these scans, will be added in the future for specific writing
experiments.

When operating in the external scan drive mode, vernier control over the
magnification or field size in the column is lost. Only three coarse field size
positions are achievable corresponding to nominal 10X, 100X, and 1000X
magnifications when operated under internal scan control. A vernier magni-
fication control for the external scan drive has been built and is operational.
It subdivides the field size at each of these coarse settings into any of 10
possible smaller field sizes. The control is a dual (x, y axis) selector
switch that resistively divides both the external x and y sweep inputs. At
each coarse selection, the full field size can be achieved as well as nominal
division of this field size by the factors 1.4, 2, 3.2, 5, 7, 10, 14, 20, 32.2,
and 50.

A special target holder has been designed and built for readout measure-
ments of both laser written and electron beam written alloy junction surface
diodes. This target holder is similar to target holders previously used in
the Cambridge Mark II stereo scan SEM for readout of laser written alloy
junction surface diodes. A photograph of the target holder is shown in
Figure 42. The base of the holder is made of brass and can accept targets of
up to 0.6×0.6 in.^{2} A copper spring contact for making electrical connection
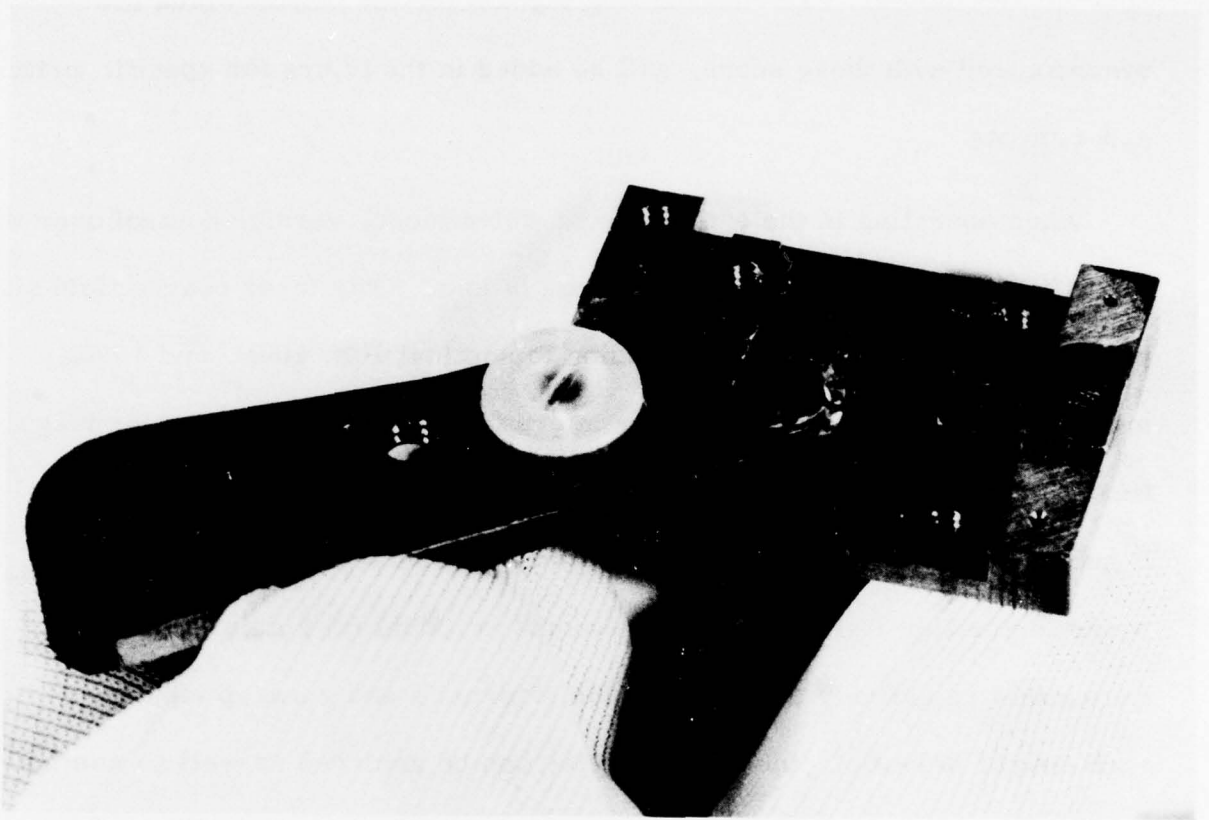
Figure 42.   Target Holder Used in the Electron Beam Write Station

to the target n-layer is mounted on the outer lip of the holder. There are also 20 mil diameter holes drilled deeply in the outer lip of the holder to provide a Faraday cup structure for beam current measurements. The brass holder is mounted on a stainless steel stub that fits into the standard Coates and Welter stage and therefore tilt, rotation, and translation control of the stage are possible.

For alloy junction writing with the electron beam, thermal bias of the target will be required. A special heated target stage has been designed and built for this purpose. Presently the stage is being assembled into another vacuum station for tests and calibration. A photograph of the heated stage is shown in Figure 43. The base plate of the target holder is similar structurally to the target stage described in the preceding paragraph. However, it is made of molybdenum because of outgassing and metal semiconductor consideration at the elevated temperatures at which it will operate. The moly base plate is drilled and fitted with ceramic sleeves through which the rhenium heating filament is threaded. Because of the elevated temperatures at which the stage will be operated, the standard Coates and Welter specimen holder cannot be used. A fixed stainless steel stem holds the sample stage to the base plate where the Coates and Welter stage mounts. The target will be held normal to the beam axis and at the proper height. Tilt and rotation control of the stage had to be sacrificed but x, y translations are still available. Not shown in the photograph in Figure 43 are aluminum heat shields that provide confinement of the heat to the target area. The temperature is monitored by a thermocouple that attaches to the moly base plate. The leads are brought out of the vacuum through a multipin header.
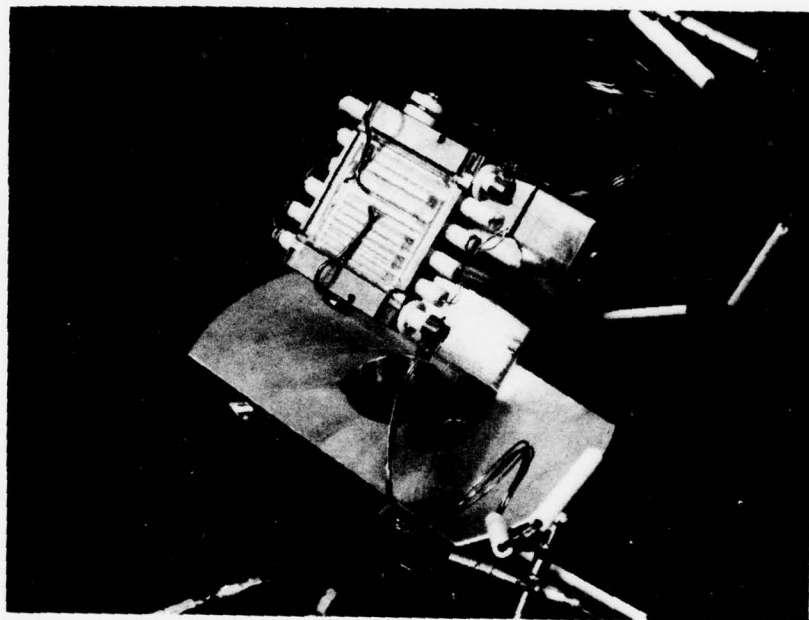
Figure 43.   Heated Stage Used in the Electron Beam Write Station

INITIAL TESTS

As mentioned previously, the Coates and Welter Instrument Corporation provided the secondary electron collection unit for the electron column on a temporary loan basis. This was indeed fortunate because it allowed operation of the equipment immediately without having to wait for the slow scan electronics with target signal modulation. A Coates and Welter field engineer provided initial instruction on the equipment, and several hours were logged on the machine whereby familiarity with the operation of a field emission column was obtained. For these purposes, a standard deposited gold mesh electron microscope specimen holder was used.

The gold mesh grid allowed the operator to gain experience in focusing and operating the column. However, it was soon replaced with the gold bars on a chrome plate glass substrate target shown in Figure 44. An engineering sketch of the gold on chrome bar pattern showing the pattern dimensions is given in Figure 45. With this target more quantitative information concerning the electron optical performance of the column can be ascertained. This target is mounted on a Coates and Welter specimen stub. There is also a 30 mil hole drilled in the specimen stub to provide a Faraday cup for beam current measurements. A photograph obtained by secondary emission readout from the column of a small portion of this target is shown in Figure 46. This portion of the target consists of 5 gold bars on 15 μ centers. A higher magnification secondary emission photo of one of the bars in this pattern is shown in Figure 47. A small speck is visible on this bar, indicating that a reasonably small beam spot size is being achieved. More quantitative measurements of
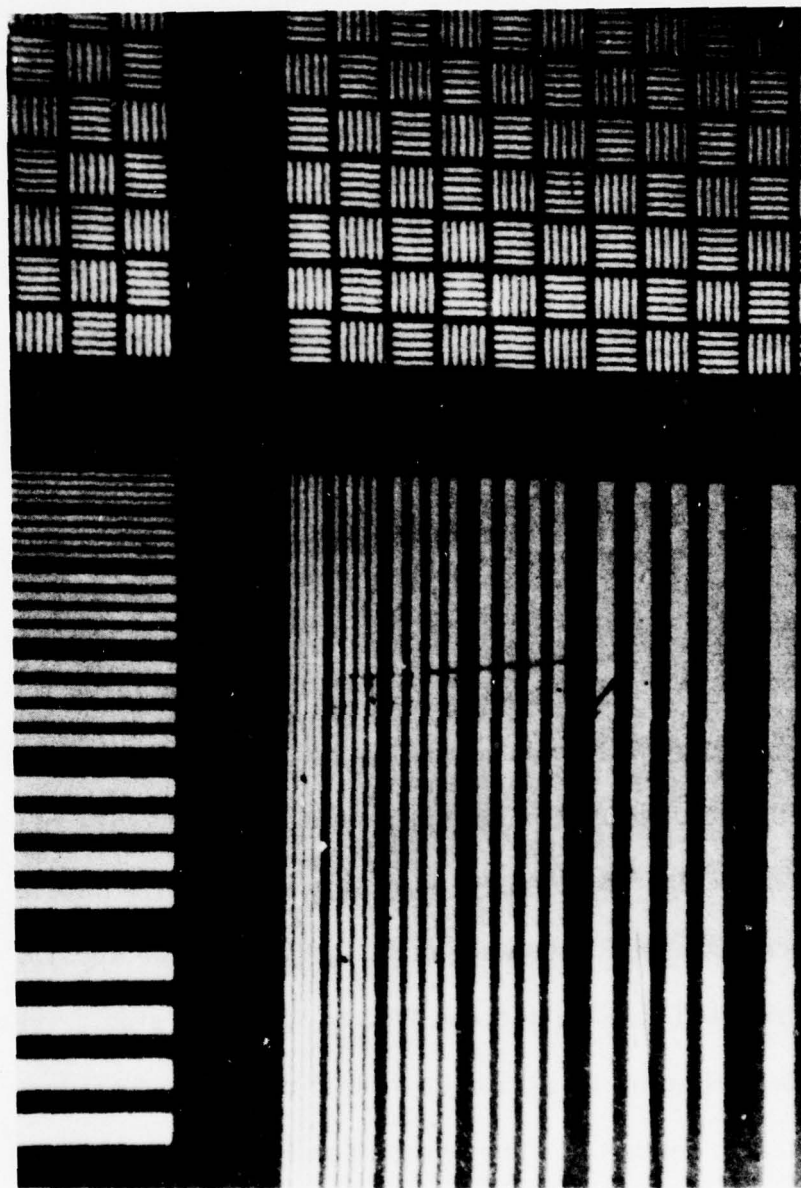
Figure 44.   Chrome Plate with Gold Bar Pattern Used in Beam
Focus Tests
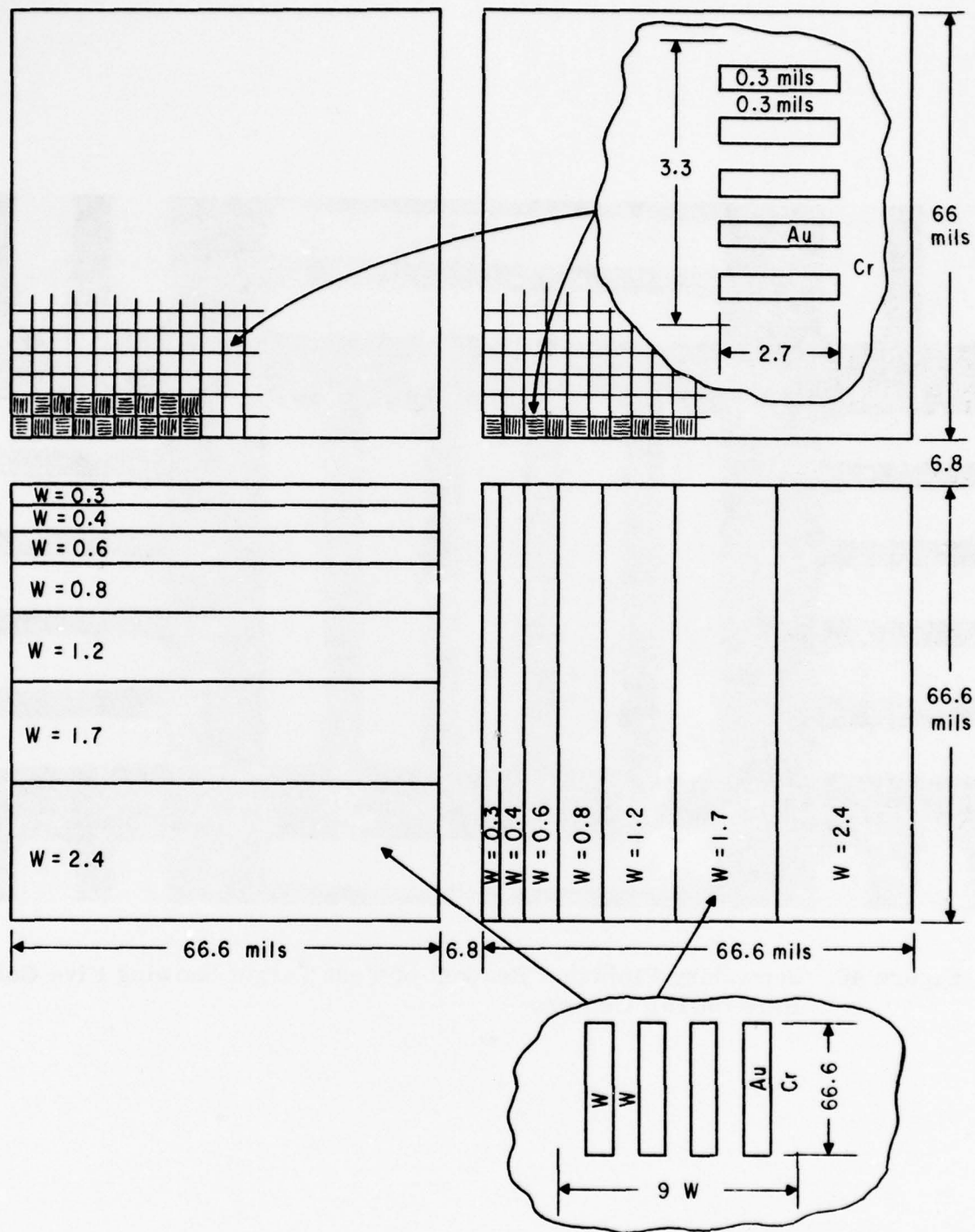
Figure 45.   Engineering Sketch of the Focus Test Target Shown in Figure 44

93
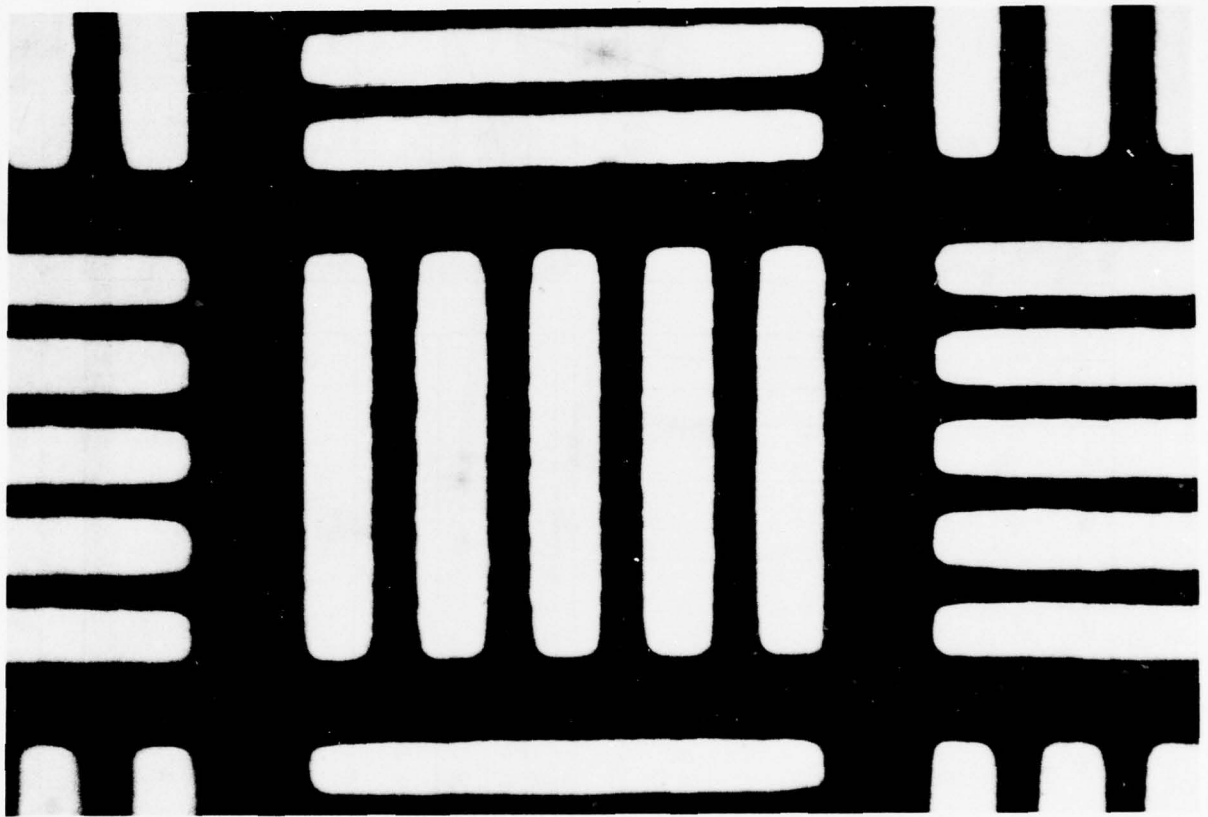
Figure 46.   Secondary Emission Readout of Test Target Showing Five Gold
Bars on 15μ Centers
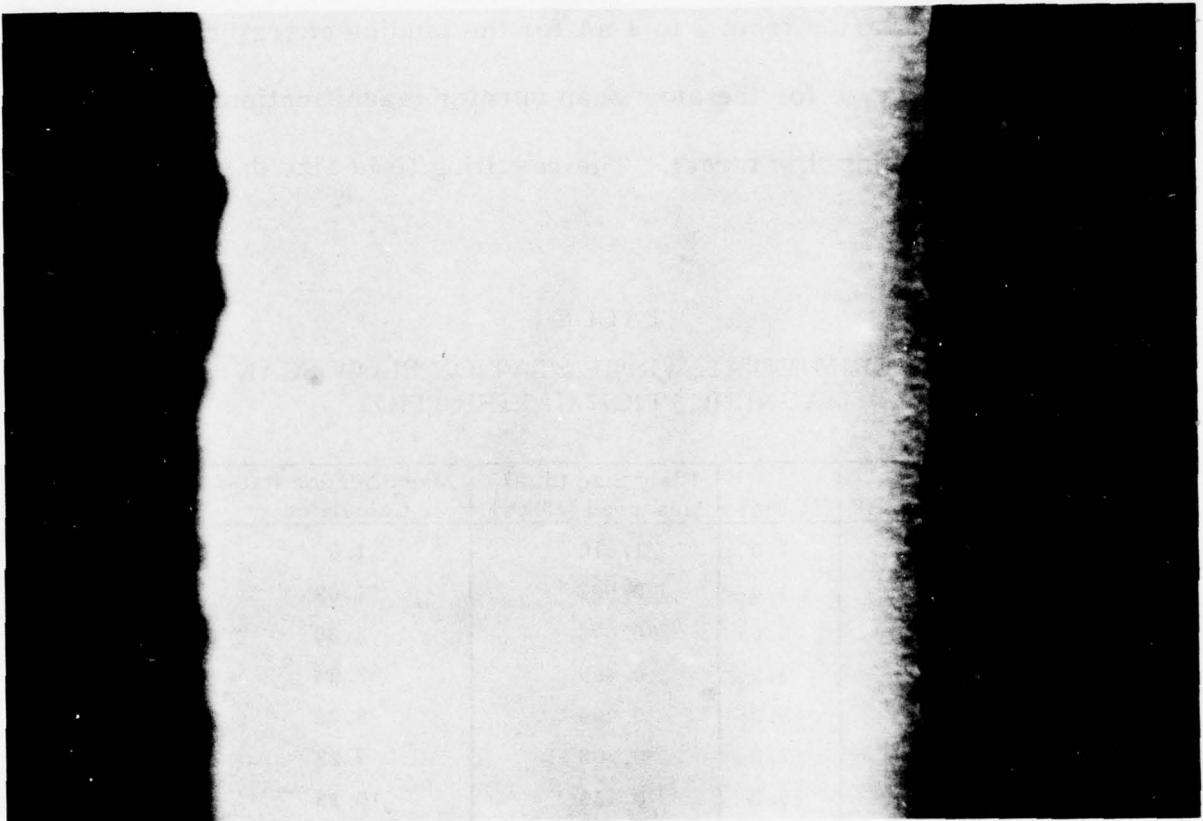
Figure 47.   Secondary Emission Readout of One Gold Bar Shown in Figure 46

spot size using the target signal modulation of the beam as it scans across the bar pattern are planned for the near future. These photographs were made at 15 kV beam landing energy with normal room temperature field emission. Beam current for normal field emission was measured in the Faraday cup and varied from 3 to 4 nA for the landing energy range of 5 to 15 kV. The field size for the slow scan vernier magnification control has been calibrated using this target. The resulting field size data are summarized in Table 5.

TABLE 5

EXPERIMENTAL WRITE STATION SLOW SCAN
MAGNIFICATION CALIBRATION

Step (Dial)	M Dial	Field Size (mm) Measured (15 kV)	Magnification Ratio Calculated
10	1.0	1.610	1.0
	1.4	0.997	1.62
	2.0	0.676	2.38
	3.2	0.455	3.54
	5.0	0.299	5.39
	7.0	0.233	7.22
	10.0	0.159	10.13
	14.0	0.114	14.12
	20.0	0.081	19.88
	32.2	0.050	32.2
	50.0	0.033	48.79
100	1.0	0.155	10.39
1000	1.0	0.0168	95.83

Coates and Welter personnel have also provided instruction for the temperature aided field emission mode of operation. Investigations of the beam current in the TFE (thermally aided field emission) mode show that stable emission of 100 nA was measured in the Faraday cup over the landing potential

range of 2 to 5 kV as summarized in Table 6. Higher stable beam currents of 150 and 200 nA were also measured in this landing energy range. These data indicate that the beam current specification has been met. Spot size measurements still have to be made.

TABLE 6

TFE BEAM CURRENT AT LOW LANDING ENERGY

Landing Potential (kV)	Beam Current--I_B (nA)	Emission Current--I_K (μA)	Comment
2	100	245	Stable
3	100	240	"
4	100	230	"
5	100	240	"

Future experiments planned for the column in the next quarter are spot size measurements over the landing potential range of 3 to 5 kV, tests of laser written diodes, and alloy junction writing using the finely focused electron beam.

SECTION VII

ARCHIVAL WRITE OPTICS STUDY

INTRODUCTION

An archival storage concept has been proposed that consists of information stored as tiny surface diodes on a large area planar diode. Two methods of forming these surface diodes are ion implantation by focused ion beam, and metal-semiconductor alloying by focused electron beam heating. During the first phase of this contract, both of these target concepts are being evaluated through theoretical and experimental studies along with a paper study of the write beam optics required for each. The results of these efforts will then be used to select the better memory approach for further development of an archival memory system.

The write beam optics studies were begun during this third quarter and are described in this section of the report. During this period, general topics were investigated. Some of these topics are beam current capability from resolvable and nonresolvable sources, source and lens system coupling, source capabilities, and lens characteristics. These properties are needed and will be used in detailed studies of the write optics configurations during the fourth quarter.

GENERAL OPTICAL CONSIDERATIONS

When considering large-scale memories, charged particle beams emerge as a strong candidate because they can be easily deflected, focused to small spot sizes, and produce large power densities. Because of these character-istics, they can interact with and alter matter in a variety of ways to produce

99

high density information recor ing at high data rates. The specific require-
ments on the charged particle beam are highly dependent on the recording
medium, storage effect, and system requirements. Generally these require-
ments reduce to developing a scanning microprobe optical system with the
maximum amount of current in the smallest possible spot commensurate with
the target resolution. These measurements arise because the bit density is
ultimately limited by the spot size and the data rate by the current contained
in that spot.

Factors that limit the minimum spot size and maximum achievable cur-
rent in a charged particle microprobe are:

- Diffraction effects
- Mechanical misalignment
- Source brightness
- Space charge
- Geometrical aberrations
- Electronic aberrations
- Deflection aberrations

In general, these factors cannot be eliminated. However, depending on the
optical configuration and the performance requirements, these parameters
vary in significance from negligible to beam limiting.

Currently, this research is aimed at information storage with bit sizes on
the order of 1000 Å and a data rate of 10^7 bits/sec. A precontract preliminary
analysis of the optics showed that the source capabilities and spherical aber-
ration of the imaging lenses were the most important optical effects. Diffrac-
tion limit was well below the spot sizes of interest, and space charge effects
were also negligible. The next most important aberration was the chromatic

100

aberration which is classed as an electronic aberration. Deflection aberrations which can be classified as geometrical, i.e., affecting spot size and position, and electronic, i.e., affecting position and repeatability of the beam, are important but not as important as the focal aberrations. The reason for this is that deflection aberrations limit the field size achievable, whereas the focal aberrations affect the basic probe formation. Furthermore, many of the deflection aberrations can be nullified quite easily by optical and electronic corrections. Mechanical aberrations can be potentially very troublesome. However, with accurate machining of optical components, good clean vacuum practices, and possibly some stigmatic correction, mechanical aberrations can be rendered negligible.

The precontract preliminary analysis indicated that a multi-lens probe system would be required to provide the coupling between the source and the desired spot requirements at the target. For the focused ion probe, this necessarily implies electrostatic optics, as shown in Figure 48, since the imaging properties are independent of the ion charge-to-mass ratio. For the focused electron writing probe, a two-lens magnetic system, as shown in Figure 49, or possibly a short focus plus relay matrix lens system (Figure 50), could be used. Conventional thermionic electron sources and plasma ion sources appeared marginally useful for beam writing systems. Field electron emission and field ionization sources appeared as much more interesting candidates. The Phase I optics studies will take a more accurate and indepth look at the performance of write optics configurations.

101
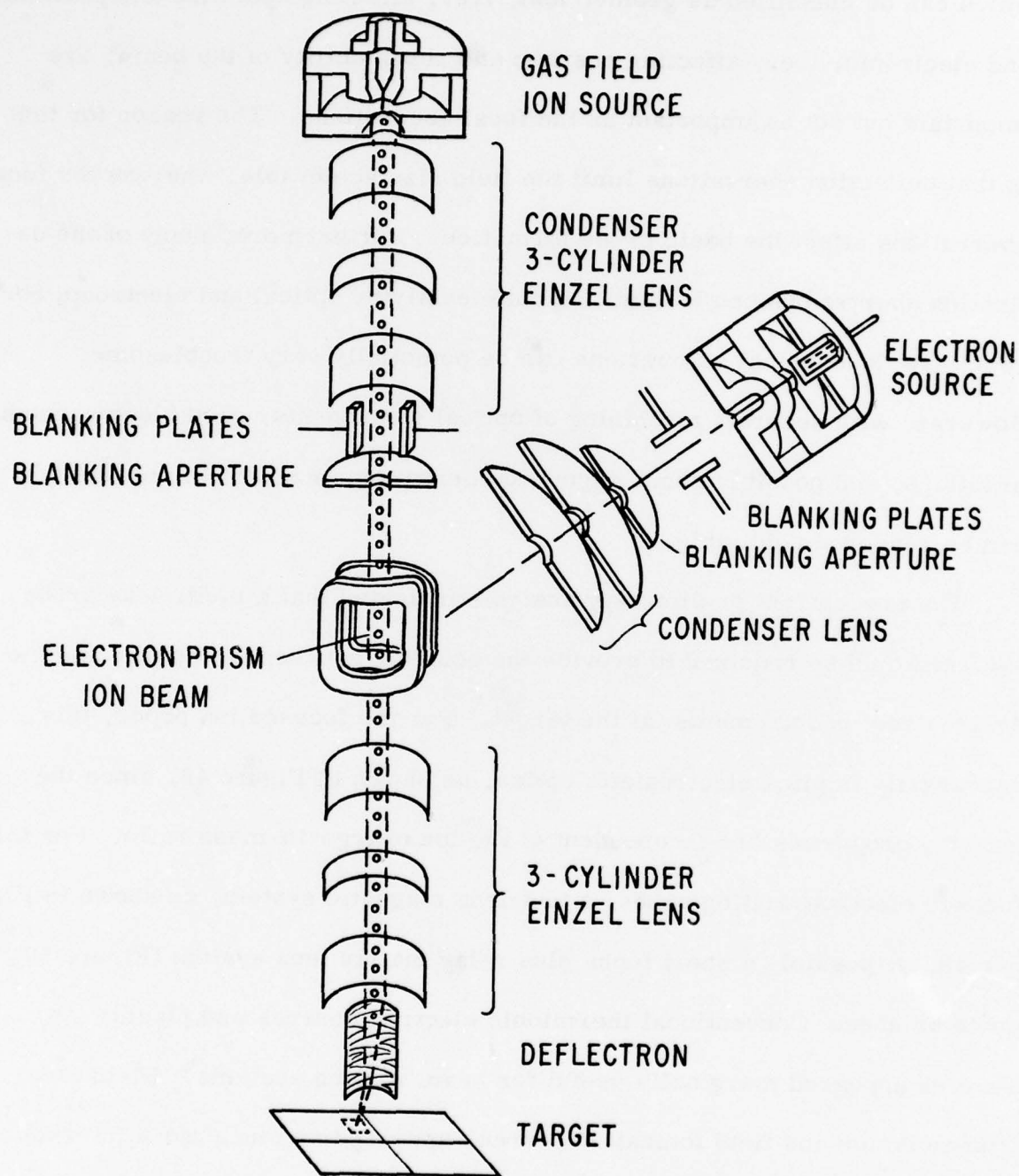
Figure 48.   Focused Ion Optics
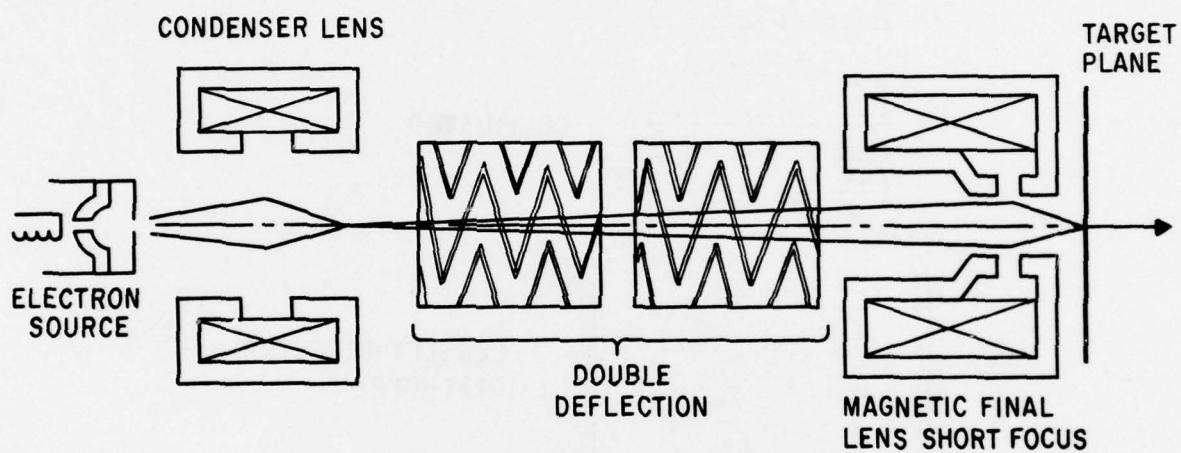
Figure 49.   Two-Lens All Magnetic Optics

103

ELECTRON SOURCE

BLANKING PLATES

CONDENSER LENS

COLLIMATOR

LENSLET SELECTOR
DEFLECTRON

TWO APERTURE
MATRIX LENS

FINE DEFLECTION
DEFLECTRON

STORAGE TARGET
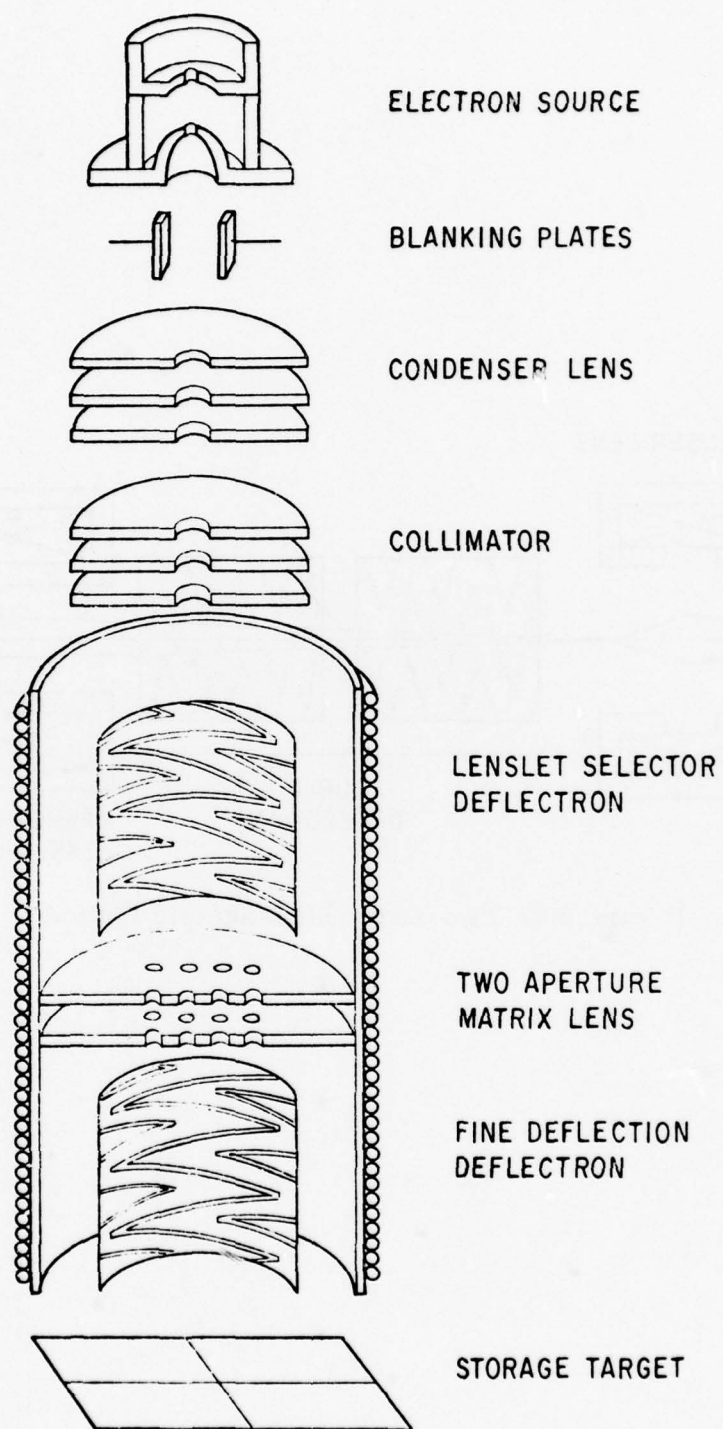
Figure 50. Short Focus Plus Relay Matrix Optics

CHARGED PARTICLE SOURCES

The fundamental building block of any charged particle optical system is the source. It must be capable of delivering the appropriate amount of current in a given solid angle such that the remaining optical components can achieve proper focal conditions of spot size and beam current at the final image. At present, the desired bit size for the archival memory is 1000 $\mathring{A}$. Therefore, the optics will be required to produce a final spot size less than or equal to this. For this spot size, field emission electron sources and field ion sources generally become particularly relevant [10]. Furthermore, research during Phase I of this contract has shown that ion damage writing with inert gas ions provides several advantages such as lower writing fluence and a wider selection of ion species for the ion implant concept. In view of these considerations, a detailed assessment of present electron and ion source characteristics, correlated with the source research at the Oregon Graduate Center, was undertaken during this quarter and is reported here.

Perhaps the most useful quantity in describing a charged particle source is the brightness, β, defined as the current, I, per unit area, dS, per unit solid angle, dΩ:

$$\beta = \frac{dI}{d\Omega dS} \tag{10}$$

The brightness normalized to the beam potential is constant along the beam trajectory of an optical system. Therefore, brightness provides a direct link in optical calculations between the source capabilities and the desired image properties. For any charged particle source with a Maxwellian

distribution of velocities, Langmuir[11] has shown that the brightness can be expressed in terms of cathode properties as:

$$\beta \approx \frac{j_o \, e V_o}{\pi k T_c} \tag{11}$$

where

j_o = cathode loading in A/cm^2

e = electronic charge = 1.6×10^{-19} C

V_o = beam potential in volts

k = Boltzmann constant in J/K

T_c = cathode temperature in K

This equation applies to conventional thermal electron sources and ion sources such as duoplasmatrons. This equation can also be used for field emission/ionization sources with a suitable redefinition of the thermal transverse energy, kT_c. However, because of the extremely small virtual source size (<50 Å), a much more useful quantity for these sources is the angular brightness in A/str. The most recent figures for brightness, as well as other parameters of interest such as cathode loading and beam energy spread, have been determined in the Phase I optics study for the most pertinent electron and ion sources.

There are many types of thermal electron cathodes such as W, Rh, LaB_6, Ba dispensers, etc. At the General Electric Research and Development Center, the barium dispenser cathode has been the workhorse for thermal cathodes. The primary reason for this is shown in Figure 51 in terms of zero field emission as a function of temperature. From these data it can
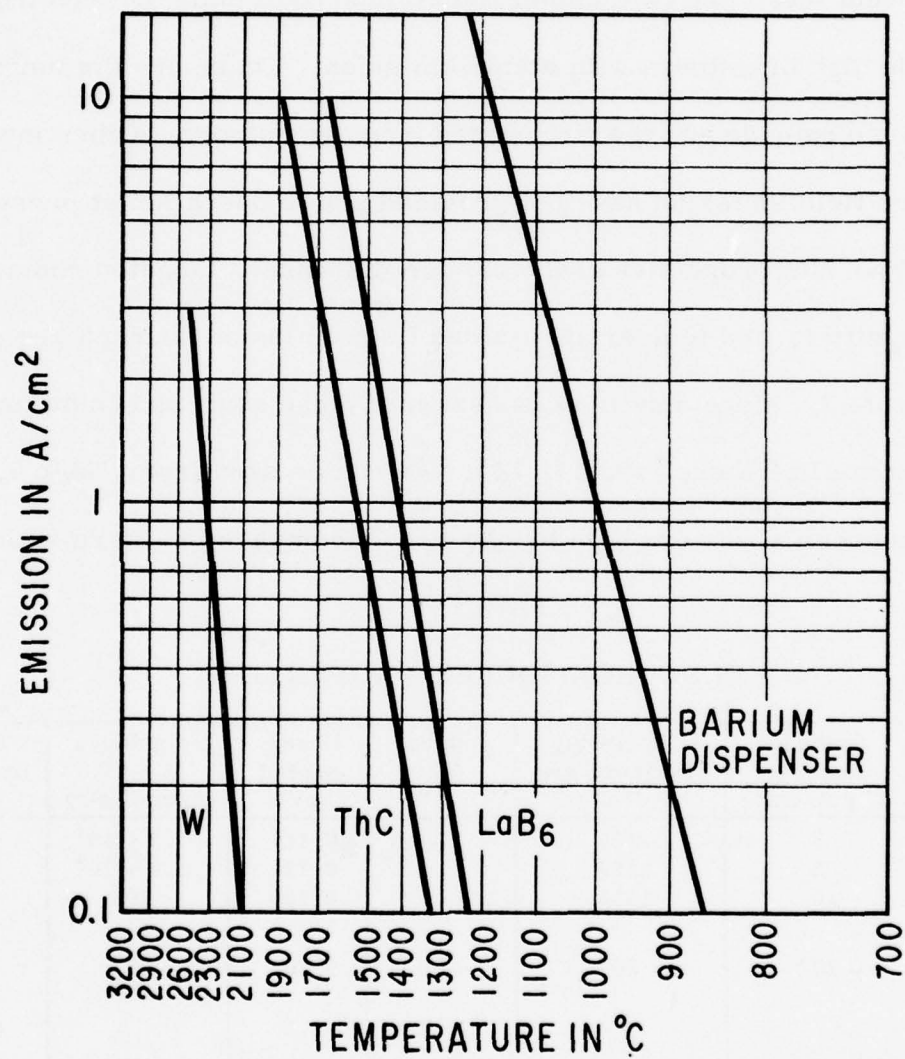
Figure 51.   Cathode Loading vs Temperature for Various Electron Cathodes

107

be seen that for a given level of performance (A/cm^2), the barium dispenser operates at a lower temperature than most other cathodes. This, coupled with the fact that it can operate at high cathode loadings (e. g., 10 A/cm^2) with long life, makes it an extremely attractive cathode for high brightness sources.

At present there are two temperature-aided field emission electron sources that provide high brightness with stable emission. These are the tungsten $\langle 100 \rangle$ built-up cathode and the zirconiated tungsten cathode. Other modes of temperature field emission have not provided stable operation at present.

The important properties of the barium dispenser, tungsten room temperature field emitter, and temperature-aided field emission sources are summarized in Table 7. More detailed discussion of these sources can be found in the appropriate literature [12, 13, 14]. As can be seen from Table 7, field emission sources have very high brightness as compared to thermionic sources.

TABLE 7

ELECTRON SOURCE PROPERTIES

Source	Cathode Loading (J_O-A/cm^2)	Operating Temperature (°K)	Source Size (Å)	Energy Spread (eV)	Brightness at 4 kV ($A/cm^2/str$)	Angular Brightness (A/str)
Ba Dispenser	3	1353	$\sim 2 \times 10^5$	0.117	3.3×10^4	0.102
	5	1393		0.121	5.3×10^4	0.167
	10	1453		0.126	105	0.314
Field Emission Room Temp.	$\sim 10^4$	300	~ 30 Å	0.20	10^8	3×10^{-5}
Temp.- Field Zr W W(100)	$> 10^4$ $> 10^4$	1400-1800 1850	~ 30 Å < 30 Å	0.7-1.0 0.8-1.5	$\sim 10^{10}$ $\sim 10^{10}$	10^{-3} 10^{-3}

It is, however, important to realize that this brightness is not achieved through a high directional-intensity of the beam, as can be seen from the angular brightness figures, but rather through the very small source size. Therefore, the advantage of this high brightness over conventional sources can be achieved only at small beam sizes on the order of 0.1 to 1 μ depending on the optics design.

Ion sources have not achieved the brightness attainable from electron sources. Conventional ion sources such as the duoplasmatron, rf discharge, penning discharge, and sputtering sources are capable of very high currents ($10^{-4}$to 10^{-1} A) but are also characterized by fairly high energy spreads and low current densities [15]. Of these ion sources, the one most promising for focused ion probes is the duoplasmatron. Field ion sources, either gas phase or liquid metal (sometimes called field desorption or hydrodynamic ion sources), present the high brightness/low source size counterparts of field emission sources in ion beam technology. These sources, for similar reasons, are expected to be extremely important for focused ion beams with submicron spot sizes. Source sizes as small as 5 Å have been calculated for the gas phase field ionization source[16]. Characteristics of the field ion sources and the duoplasmatron, based on the best available figures to date, are summarized in Table 8.

Currently, field ion sources have only been successfully developed using H_2, Ar, and other inert gasses such as Ne and Xe. Conventional semiconductor dopants such as a P, As, and B have been confined to duoplasmatrons. Ga, InGa, and Cs ions have been obtained from liquid metal sources. However,

109

TABLE 8

ION SOURCE CHARACTERISTICS

Source	Total Current (A)	Current Density (A/cm²)	Energy Spread (eV)	Brightness (A/str/cm²)	Angular Brightness (A/str)
Duoplasmatron	10^{-3} to 10^{-1}	10^{-2} to 1	10	$< 10^3$	-
Field Ion	10^{-9} to 10^{-8}	10^3	2-5	10^5	1.5×10^{-6}
Liquid Metal Field Ion	10^{-8} to 10^{-6}	$\sim 10^5$	?	10^7	10^{-4}

energy spreads of up to 30 eV have been reported [17] along with question-able stability. Greater development of these sources is required in order to achieve the same or better performance as the gas-phase field ion source. New developments in both of these sources are being closely monitored at the Oregon Graduate Center.

BEAM CURRENT CONSIDERATIONS FOR A SPHERICAL ABERRATION LIMITED SYSTEM

As shown in the preceding section, source sizes vary over a large range from a few angstroms to several microns depending on the source type. Conventional sources such as thermionic electron or plasma ion sources have larger source sizes that can usually be resolved by the lenses in the optical column. This leads to certain conditions under which the maxi-mum beam current can be achieved for a given source, lens system, and desired operating characteristics. The field sources with their extremely small source size cannot always be resolved by the lens system. The limit

110

for this case is the ideal point source which cannot be resolved with any lens with finite aberrations. For this case, the final spot size is set by the aberration and the allowed half-angle of the lens system. This results in an entirely different set of conditions for the probe current. These two operating points will be examined more closely in this section.

The maximum current criterion for a resolvable source will be considered first. Assume a generalized optical system, as shown in Figure 52, which images an on axis source of size d_O, to a final spot, d, at the image plane. The imaging optics may be a single lens system or a multiple lens system. However, for present purposes, they are assumed to be characterized by a linear magnification, m, and an equivalent spherical aberration coefficient, C_S. The equivalent spherical aberration for multi-lens systems will be considered in more detail later in this report. In terms of the parameters of Figure 52, the spot size at the image plane for a spherical aberration limited system is given by:

$$d^2 = dg^2 + (1/4)C_S^2 \, \phi_i^6 \qquad (12)$$

where

$\quad$ d = final spot size at the target (cm)

$\quad$ d_g = Gaussian spot size at the target (cm)

$\quad$ C_S = spherical aberration coefficient of the lens system (cm)

$\quad$ ϕ_i = beam half-angle at the target (rad)

The beam current, I, contained within this spot is:

$$I = \beta(\pi/4) \, dg^2 \, \Omega_i \qquad (13)$$

where

$\quad$ β = beam brightness at the image (A/cm^2/str)

$\quad$ Ω_i = is the solid angle subtended by the beam at the target (= $\pi\phi_i^2$ str)

111

Figure 52. General Optical System
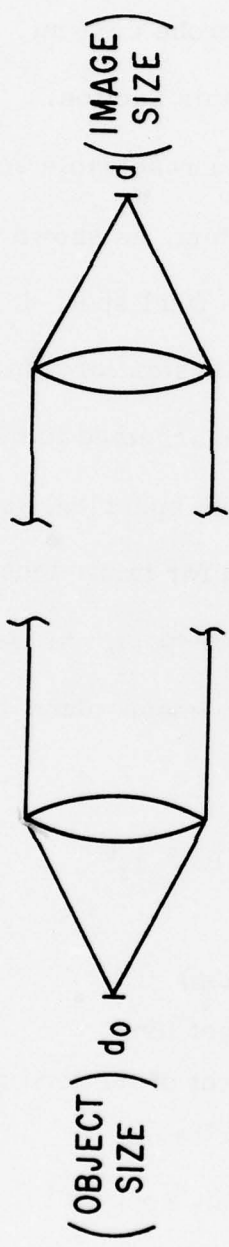
LENS SYSTEM

C_S = SPHERICAL ABERRATION CONSTANT

m = LINEAR MAGNIFICATION

$d\left(\begin{array}{c}\text{IMAGE}\\\text{SIZE}\end{array}\right)$

$\left(\begin{array}{c}\text{OBJECT}\\\text{SIZE}\end{array}\right) d_0$

Solving Eq. (12) for dg² and substituting in Eq. (13) gives:

$$I = \frac{\pi^2}{4} \beta \left[d^2 - \frac{1}{4} C_s^2 \phi_i^6 \right] \phi_i^2 \tag{14}$$

The current is maximized with respect to the beam half-angle as:

$$\frac{dI}{d\phi_i} = \frac{\pi^2}{4} \beta \left[2d^2 \phi_i - 2 C_s^2 \phi_i^7 \right] = 0 \tag{15}$$

Solving Eq. (15) for the optimum half-angle for maximum beam current gives:

$$\phi_{i\ opt} = (d/C_s)^{1/3} \tag{16}$$

Substituting Eq. (16) back into Eq. (15) gives the maximum beam current:

$$I_{max} = \frac{3\pi^2}{16} \beta \frac{d^{8/3}}{C_s^{2/3}} \tag{17}$$

Note that Eq. (16) in conjunction with Eq. (12) mandates a specific Gaussian or geometric spot size at the target given by:

$$dg = (\sqrt{3}/2)d \tag{18}$$

The geometric spot size at the image plane, dg, is related to the source size, d_o, by the linear magnification m:

$$dg = md_o \tag{19}$$

Therefore, in order to achieve the maximum current conditions, the magnification of the optical system must be:

$$m = \frac{\sqrt{3}}{2} \frac{d}{d_o} \tag{20}$$

The preceding analysis is based on the underlying assumption that the spherical aberration coefficient is not a strong function of the magnification. Thus, when adjusting the imaging system for the optimum condition (Eq. 20),

113

the spherical aberration is not strongly influenced by m, and the beam current (Eq. 17) is severely reduced. This condition is easily satisfied for demagnifying systems (m<1) since C_s, in general, has a polynomial dependence on the magnification. However, for a magnifying system (m>1), C_s changes so drastically with m that the beam current can be severely reduced. The end result is that more current can be achieved at an operating point other than that prescribed by the maximum current conditions predicted here. Thus the conditions for maximum current outlined in the preceding section can be expected to apply to demagnifying optical systems using a thermionic emission source or duoplasmatron ion source that has large source sizes. On the other hand, this analysis is not expected to apply to field electron and ion sources which have very small source sizes and will have to operate with magnifications greater than unity for the spot sizes of interest here.

As an extreme case of a nonresolvable source, consider the optical system of Figure 52 operating with an ideal point source (i.e., $d_o = 0$). For these conditions, Eq. (12) reduces to:

$$d^2 = (md_o)^2 + \frac{1}{4} C_s^2 \phi_i^6 \approx \frac{1}{4} C_s^2 \phi_i^6 \tag{21}$$

for a spherical aberration limited system. Because the source is just an ideal point, the source brightness in $A/cm^2/str$ is meaningless, since the source current density cannot be defined. In this case, the source parameter of interest is the angular brightness, Ω_{β_o}, in A/str. This source parameter is also applicable to field emission/ionization sources which have a finite source size that is so small that it cannot be precisely determined. For these sources, the angular brightness is a characterizing parameter of the

114

source that can be measured directly. In terms of the angular brightness, the beam current delivered into a solid angle defined by the source half-angle ϕ_O is

$$I = \Omega_{\beta_O} \pi \phi_O^2 \qquad (22)$$

Using Abbe's sine condition, the half-angle in object space ϕ_O is related to the half-angle in image space by the equation:

$$\phi_O = m \phi_i \sqrt{V_i / V_O} \qquad (23)$$

where V_i and V_O are the beam potentials in image and object space, respectively. Substituting Eq. (23) into Eq. (22) gives:

$$I = \Omega p_O \pi m^2 (V_i/V_O) \phi_i^2 \qquad (24)$$

The beam half-angle in image space is defined in terms of the final spot size, d, and the spherical aberration coefficient of the imaging system from Eq. (21) as :

$$\phi_i = (2d/C_s)^{1/3} \qquad (25)$$

Thus substituting Eq. (25) into Eq. (26) gives the beam current in the imaged spot as:

$$I = \Omega_{\beta_O} \pi m^2 \frac{V_i^{2/3}}{V_O} \cdot \frac{2d^{2/3}}{C_s^{2/3}} \qquad (26)$$

A comparison of Eq. (25) and (26) illustrates a fundamental important difference in beam current capabilities of an optical system imaging a resolvable and nonresolvable source. For the case of a resolvable source, Eq. (17) shows that the beam current is proportional to the 8/3 power of the final spot diameter, d. This is the condition that applies to conventional sources such as the Radley-Pierce electron source and the duoplasmatron

115

ion source for probe diameters on the order of 1000 Å. For a nonresolvable source, the beam current is proportional to the 2/3 power of the final spot diameter, d, as shown by Eq. (26). This condition applies to field electron and field ionization sources with their extremely small source sizes. In practice, this means that more current can be achieved at small spot sizes with field emission or ionization sources than with conventional thermionic sources, whereas the converse is true for larger spot sizes. The break-even point in current capability for the two source types falls somewhere in the 1000 Å to 1 μ range and is highly dependent on the optics configuration. It is for this reason that both source types will be considered in the optics analysis for the archival write stations.

MULTI-LENS SYSTEM ABERRATIONS

As indicated in the general optics considerations section of this report, the imaging properties of the writing probe are the most important since they affect the basic achievable spot size. Deflection aberrations are somewhat secondary in importance because they affect the final achievable field size but not the basic probe size and beam current. It was also indicated, in the general optics section, that a multi-lens system would be required in order to couple effectively the source capabilities to the desired target conditions. During this quarter, equations governing the focal properties of a two-lens imaging system were developed and are presented here.

A two-lens collimating system, as shown in Figure 53, is considered for the optical column. A collimating system such as this has several optical advantages such as no crossovers between object and image, lower individual
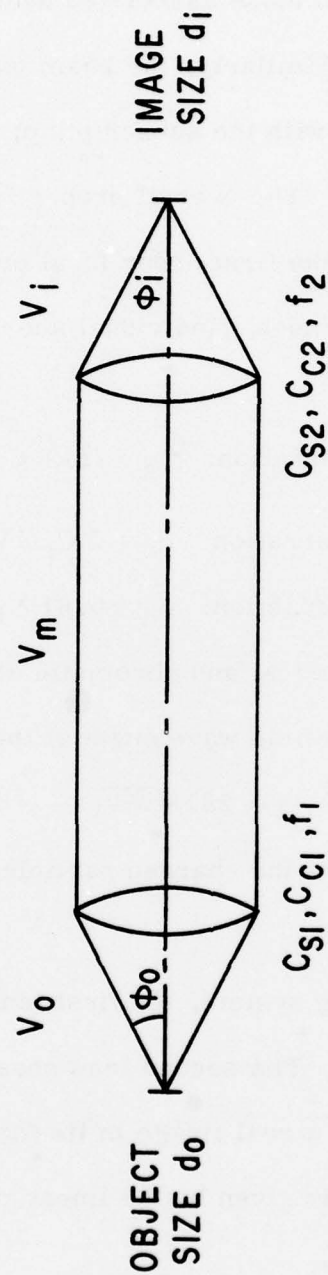
116

Figure 53. Two-Lens Collimating Optical System

117

lens aberrations, and less sensitivity to stray fields. As indicated on the figure, the parameters associated with the first lens nearest the sources are denoted by the subscript 1, and those associated with the second lens, nearest the image, by a subscript 2. Similarly, the beam potential, V, and beam half-angle, ϕ, are suitably defined with the subscripts o, m, i, to indicate object side, middle, and image side. The overall properties of the system are characterized by a combination of the first order focal properties and third order aberrations of the individual lenses. Individual aberration terms for the lenses are:

$$\text{Spherical aberration:} \quad d_s = (1/2) \, C_s \, \phi^3 \tag{27}$$

$$\text{Chromatic aberration:} \quad d_c = 2 \, C_c (\Delta V / V) \, \phi^3 \tag{28}$$

$$\text{Diffraction:} \quad d_d = 0.61 \, \lambda_i / \phi_i \tag{29}$$

where C_s, and C_c are the spherical and chromatic aberration coefficients, respectively. The charged particle wavelength at the image, λ_i, is given by:

$$\lambda_i = 0.287 / \sqrt{M V_i} \tag{30}$$

where M is the atomic weight of the charged particle. (Note that for electrons, M can be taken as $\approx 1/1837$.)

For a two-lens collimating system, the first lens produces a virtual image of the object at infinity. The second lens sees this image as a virtual object at infinity and produces a real image in its focal plane. To first order, the image to object size ratio is given by the linear magnification which for a two-lens collimating system is:

$$m = f_2 / f_1 \tag{31}$$

Of course, the image size is not determined by first order properties alone since aberrations of both lenses affect the final spot size. Since the first

118

lens produces a virtual image at infinity, the aberrations are most conveniently handled by referring the effects of the first lens aberrations to the object. This produces an effective object that is imaged to first order by both lenses and further affected only by the aberrations of the second lens.

Considering the two-lens collimating system of Figure 53, the true object size, d_o, is increased to an effective source size, d_{se}, by the aberrations of the first lens referred to the object as:

$$d_{se} = \sqrt{d_o^2 + \frac{1}{4} C_{si}^2 \phi_o^6 + 4 C_c \left(\frac{\Delta V}{V_o}\right)^2 \phi_o^2} \tag{32}$$

Using Eq. (32) as the source size, the final image d_i is given as a quadratic combination of the first order imaging and the aberrations of the second lens:

$$d_i = \sqrt{(md_{se})^2 + d_s^2 + d_c^2 + d_d^2} \tag{33}$$

Substituting the individual aberration terms from Eq. (27) to (29) and (32) into Eq. (33) and making use of the Abbe's sine condition:

$$\phi_o = m\sqrt{V_i/V_o} \; \phi_i \tag{34}$$

gives the final spot size at the target:

$$d_i = \left[m^2 d_o^2 + \frac{1}{4}\left\{ m^8 C_{s1}^2 \left(\frac{V_i}{V_o}\right)^3 + C_{s2}^2 \right\} \phi_i^6 \right. \tag{35}$$
$$\left. + 4 \left\{ m^4 \; C_{c1}^2 \; \frac{\Delta V^2 V_i}{V_o^3} + C_{c2}^2 \left(\frac{\Delta V^2}{V_i}\right) \right\} \phi_i^2 + \left(\frac{0.61\lambda_i}{\phi_i}\right)^2 \right]^{1/2}$$

The effects of a third lens, as indicated in Figure 54, can easily be included by considering d_i as the object for the final lens and using Abbe's sine condition for ϕ_i and ϕ_3 to represent all aberrations in terms of ϕ_3 as:

$$d_f = \sqrt{(m_3 d_i)^2 + \frac{1}{4} C_{S3}^2 \; \phi_3^6 + 4 C_{c3}^2 \; \phi_3^2 \left(\frac{\Delta V}{V_3}\right)^3} \tag{36}$$
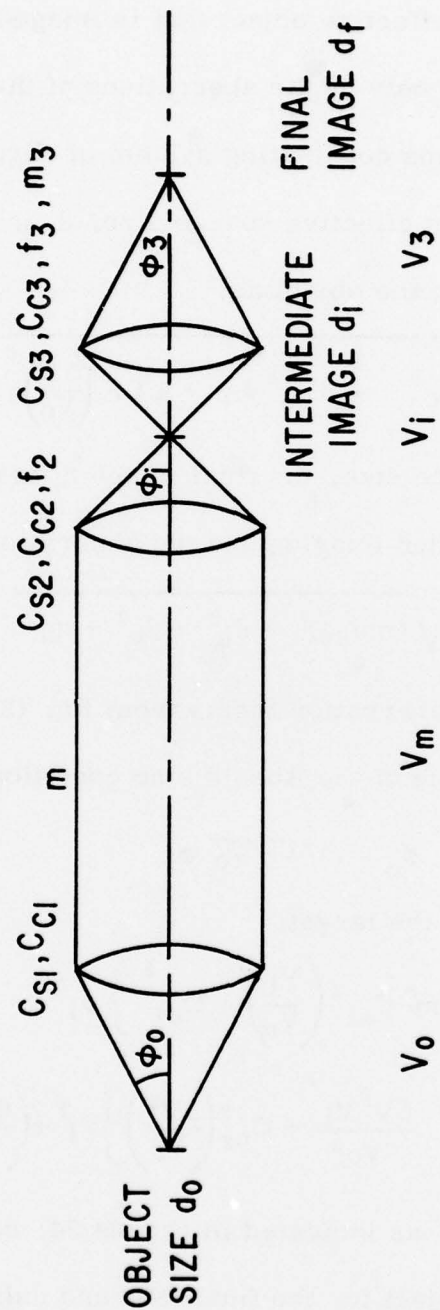
119

Figure 54. Three-Lens Optical System

120

These equations will be used to evaluate the final spot size for the archival write columns during the next quarter.

LENS PROPERTIES

As seen in the preceding section, the focal and aberration constants for the lenses are required in order to estimate the optical performance. These parameters are functions of the lens type, its geometry and operating point. Recently, a very extensive computer study of various electron lenses has been completed at the General Electric Research and Development Center. The study has resulted in the accurate numerical data for paraxial focal properties, spherical aberration constants, and chromatic aberration constants for many lens types which are summarized in Figure 55.

In the computer analysis of electron lenses, Bertram's technique[18] was used to determine the axial potential of the electrostatic equidiameter two- and three-cylinder lenses. The axial potential and its derivatives are obtained as integrals involving modified Bessel functions which can be conveniently evaluated numerically. The axial potentials of the two- and three-aperture electrostatic lenses were found by using a modified form of Liebmann's relaxation technique as described by Shortley and Weller [19]. The derivatives of the potential in these cases were found from a fast Fourier transform technique[20] by reconstructing the potentials obtained by the relaxation method. The lens potentials and their derivatives were then used with Liebmann's ray tracing technique[21] to evaluate the optical properties, i.e., paraxial and aberration constants for the electrostatic lenses. The optical constants for symmetrical magnetic lenses were available from a previous source[22].

121

LENS TYPE	# OF CASES	ELECTRON OPTICAL SYMBOL
3 APERTURE EINZEL	27 SYM $\begin{cases} R_1 = R_3 \\ S_1 = S_2 \end{cases}$ 72 ASYM $\begin{cases} R_1 \neq R_2 \neq R_3 \\ S_1 \neq S_2 \end{cases}$	
2 APERTURE IMMERSION	6 SYM $R_1 = R_2$ 18 ASYM $R_1 \neq R_2$	
2 CYLINDER IMMERSION	8 SYM $R_1 = R_3$ 16 ASYM $R_1 \neq R_3$	
3 CYLINDER EINZEL	6 SYM $S_1 = S_2$ 12 ASYM $S_1 \neq S_2$	
MAGNETIC	20 SYM $R_1 = R_2$ 14 ASYM $R_1 \neq R_2$	

Figure 55. Lens Study Summary

During this quarter, several of the lens programs were reestablished on the time-sharing computer network. Aberration properties for various electrostatic lenses that occupy the same space were investigated. The results for spherical aberration are shown in Figure 56. These lens data will be used in the fourth quarter to aid in selecting the best lens type and geometry for the archival write optics.

SUMMARY

During this quarter, the optics study was confined to acquiring and developing the tools necessary for a general analysis of the various write optics configurations. These tools will be used in the analytical evaluation of specific write optics configurations during the fourth quarter.
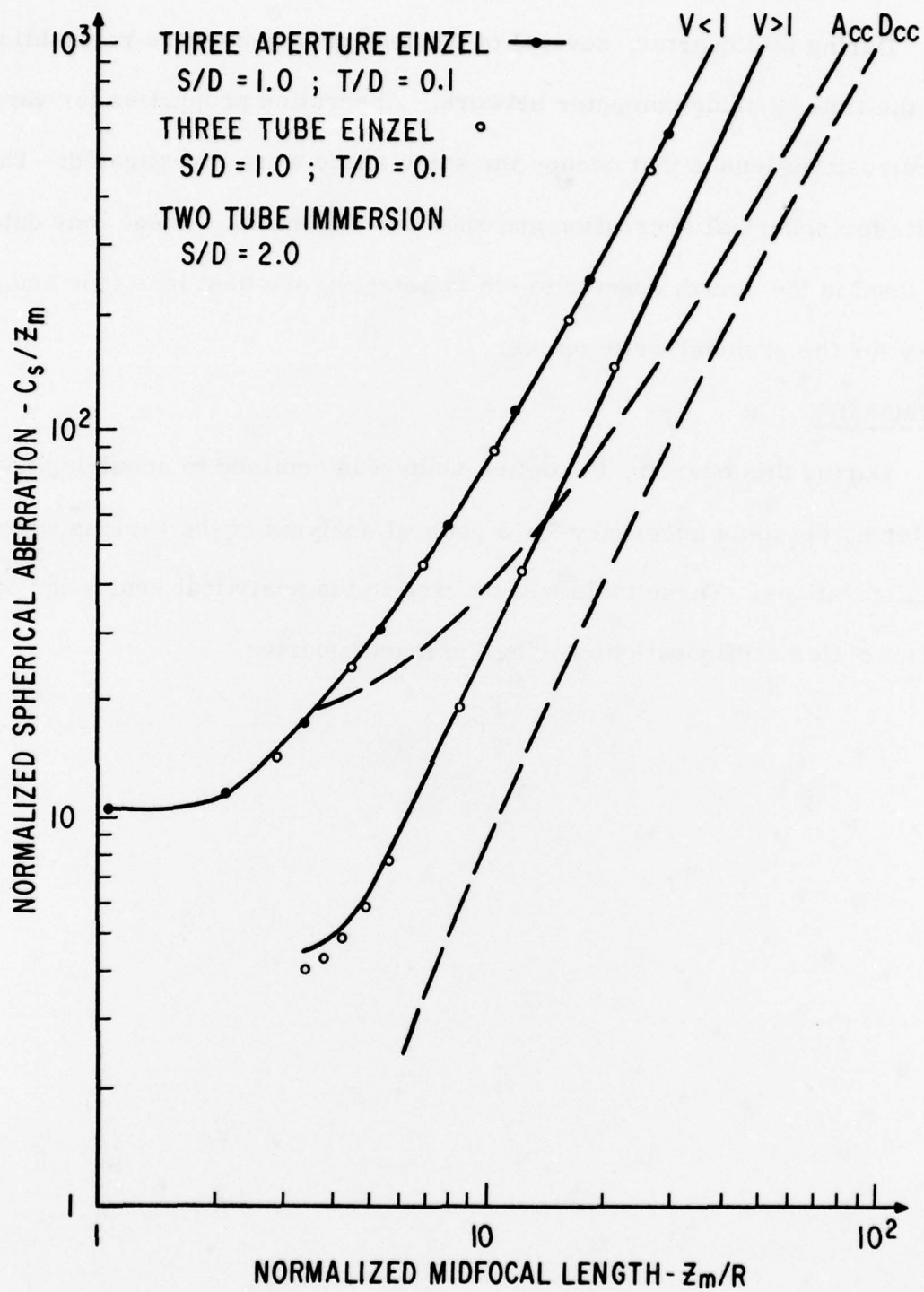
Figure 56. Spherical Aberration Constant (C_S) as a Function of Midfocal Length (Z_m)

REFERENCES

1. F. N. Schwettmann, "Enhanced Diffusion During the Implantation of Arsenic in Silicon," Applied Physics Letters, Vol. 22, 570-572 (1973).

2. B. L. Crowder, J. F. Ziegler, and G. W. Cole, "The Influence of the Amorphous Phase on Boron Atom Distributions in Ion Implanted Silicon," International Symposium on Ion Implantation in Semiconductors and Other Materials, B. L. Crowder, ed., Plenum Press, New York, 1972, pp. 257-265.

3. K. Wittmaack, J. Maul, and F. Schulz, "Energy Dependence and Annealing Behavior of Boron Range Distributions in Silicon," International Symposium on Ion Implantation in Semiconductors and Other Materials, B. L. Crowder, ed., Plenum Press, New York, 1972, pp. 119-131.

4. B. L. Crowder, J. F. Ziegler, and F. F. Morehead, "The Application of Ion Implantation to the Study of Diffusion of Boron in Silicon," International Symposium on Ion Implantation in Semiconductors and Other Materials, B. L. Crowder, ed., Plenum Press, New York, 1972, pp. 267-274.

5. S. M. Davidson, "Rapid Profile Measurements in Ion Implanted Silicon," Journal of Physics E, Vol. 5, 23-26 (1972).

6. P. V. Gray and K. L. Wang, "Surface Characterization of Ion Implanted Si-SiO$_2$ Structures," IEDM Technical Digest, 340-344 (1976).

7. D. M. Brown, R. C. Connery, and P. V. Gray, "Doping Profiles by MOSFET Deep Depletion C(V)," Journal of the Electrochemical Society, Vol. 122, 121 (1975).

8. J. F. Gibbons, W. S. Johnson, and S. W. Mylroie, Projected Range Statistics, Halsted Press, New York, 1975.

9. B. Abeles, "Lattice Thermal Conductivity of Disordered Semiconductor Alloys at High Temperatures," Physical Review, 131, 1906 (1963).

10. L. W. Swanson, Proceedings of the Symposium on Advanced Memory Concepts, Stanford Research Institute, Menlo Park, Cal., p. V-130.

11. D. B. Langmuir, "Theoretical Limitations of Cathode-Ray Tubes," Proceedings of the IRE, Vol. 25, 977 (1937).

12. W. C. Hughes, <u>Record of the 10th Symposium on Electron, Ion, and Laser Beam Technology,</u> Gaithersburg, Maryland, May 1969, San Francisco Press Inc., San Francisco, Cal., 1969.

13. L. W. Swanson, "Comparative Study of the Zirconiated and Built-Up W Thermal-Field Cathode, " <u>Journal of Vacuum Science and Technology,</u> Vol. 12, 1228 (1975).

14. L. W. Swanson and N. A. Martin, "Field Electron Cathode Stability Studies: Zirconium/Tungsten Thermal-Field Cathode," <u>Journal of Applied Physics</u>, Vol. 46, 2029 (1975).

15. R. G. Wilson and G. R. Brewer, <u>Ion Beams with Application to Ion Implantation,</u> John Wiley, New York, 1973.

16. J. H. Orloff and L. W. Swanson, "Study of a Field-Ionization Source for Microprobe Applications," <u>Journal of Vacuum Science and Technology,</u> Vol. 12, 1209 (1975).

17. V. E. Krohn and G. R. Ringo, "Ion Source of High Brightness Using Liquid Metal," <u>Applied Physics Letters,</u> Vol. 27, No. 9, 479 (1975).

18. S. Bertram, "Calculation of Axially Symmetric Fields," <u>Journal of Applied Physics</u>, Vol. 13, 496 (1942).

19. G. H. Shortley and R. Weller, "The Numerical Solution of Laplace's Equation," <u>Journal of Applied Physics</u>, Vol. 9, 334 (1938).

20. E. O. Bringham and R. E. Morrow, "The Fast Fourier Transform," <u>IEEE Spectrum</u>, 63 (1967).

21. G. Liebmann, "An Improved Method of Numerical Ray Tracing Through Electronic Lenses," <u>Proceedings of the Physical Society,</u> Vol. B62, No. 360, 753-772 (1949).

22. H. G. Parks, MSEE thesis, Syracuse University, Syracuse, N. Y., June 1969.